

**DEVELOPMENT AND VALIDATION OF AN ELECTRIC SUBMERSIBLE
PUMP BEARING EROSION FACILITY THAT REPLICATES
THE CONDITIONS EXPERIENCED DURING PUMP OPERATION**

A Thesis

by

ANDREW WILLIAM JOHNSON

Submitted to the Office of Graduate and Professional Studies of
Texas A&M University
in partial fulfillment of the requirements for the degree of

MASTER OF SCIENCE

Chair of Committee,	Gerald Morrison
Committee Members,	Andrea Strzelec
	Robert Randall
Head of Department,	Andreas Polycarpou

December 2015

Major Subject: Mechanical Engineering

Copyright 2015 Andrew William Johnson

ABSTRACT

The ever increasing global oil demand has forced the energy industry to provide artificial stimulation to many oil wells to increase their productivity. A common way to do this is to install an electric submersible pump (ESP) in the wellbore to overcome the pressure losses associated with bringing hydrocarbons to the surface for processing. This type of artificial lift has become increasingly more popular in offshore oil fields. When an ESP fails in a subsea well, the cost to replace it has been estimated to be as much as forty times the cost of the pump due to the high price of offshore rig time.

The increase in deep water oil production over the past two decades has demanded that ESPs operate properly for as long as possible. One of the most common failure modes for ESPs arises from erosion by sediments (fine sand) in the flow. The journal bearings in the ESP are susceptible to erosion from these particles because the pump bearings are lubricated by the fluid flowing through the pump. Previous ESP erosion tests that were conducted at the Turbomachinery Laboratory at Texas A&M University show that the erosion caused by sand particles in the flow lead to ESP journal bearing erosion that ultimately caused the pump to fail.

This work provides the design, construction, and validation of a testing apparatus that was built to replicate a single ESP stage so that journal bearings can be eroded and evaluated to be used to design new bearings with a longer lifetime. The testing apparatus is capable of replicating the conditions of an ESP to conduct erosion studies on a journal bearing independent of the actual pump. This provides a cost effective way to test different bearing materials over a variety of different operating conditions.

The testing apparatus is capable of operating speeds up to 7200 RPM, gas volume fractions (GVF) ranging from 0-100%, and different testing liquids (water or oil). The testing apparatus was designed to collect bearing annulus dynamic pressure, temperature, and the radial loads the bearing experiences as well as measure the orbital displacement of the bearing. In addition, the bearing geometry can be measured and the surface can be observed at discrete time intervals.

DEDICATION

I would like to dedicate this thesis to my parents who have encouraged me through all of my academic endeavors. I would also like to dedicate this work to my fiancé, Stephanie, for all of the support along the way.

ACKNOWLEDGEMENTS

I would like to thank the chair of my committee and research adviser, Dr. Morrison, for providing support throughout my master's research. His guidance and experience was invaluable throughout my project and provided a holistic education that exceeded what is found in a textbook. I would also like to thank my other committee members, Dr. Strzelec and Dr. Randall, for taking time out of their busy schedules to serve on my committee. In addition I would like to thank Dr. Stuart Scott and Hector Casillas at Shell for providing the funding for my project.

I want to acknowledge all my lab colleagues at the Turbo Lab, but in particular I would like to recognize Changrui Bai for working as my partner throughout the project. Each and every one of my lab mates contributed to my work in some way and I want to thank you all.

NOMENCLATURE

ESP	Electric Submersible Pump
FFT	Fast Fourier Transform
GVF	Gas Volume Fraction
ID	Inner Diameter
Mil	One thousandth of an Inch
OD	Outer Diameter
P&ID	Piping and Instrumentation Diagram
RPM	Rotations per Minute
VFD	Variable Frequency Drive

TABLE OF CONTENTS

	Page
ABSTRACT	ii
DEDICATION	iv
ACKNOWLEDGEMENTS	v
NOMENCLATURE.....	vi
TABLE OF CONTENTS	vii
LIST OF FIGURES.....	ix
LIST OF TABLES	xv
INTRODUCTION.....	1
Background.....	1
Problem Statement.....	4
LITERATURE REVIEW	5
DESCRIPTION OF FACILITY	13
Overall Configuration.....	13
Rotor Dynamics	15
XLTRC2 Simulation.....	18
Sommerfeld Theory	22
Testing Chamber.....	24
Testing Stand	30
Fluid Movement.....	36
Sand Settling and Fluid Storage Tanks.....	39
Sand Administration	41
Controls.....	43
FACILITY CONSTRUCTION.....	49
FACILITY VALIDATION.....	54
CONCLUSIONS AND RECOMMENDATIONS.....	81

Conclusions.....	81
Recommendations and Future Work	82
REFERENCES.....	84
APPENDIX A DRAWINGS.....	85
Assembly A: Testing Stand Drawings.....	85
Assembly B: Testing Chamber Drawings	95
Assembly C: Top Configuration.....	101
Assembly D: Sand Administrator	109
Assembly E: Shaft and Imbalance Disk	112
Assembly F: Imitation Brass Bearings	115
Assembly G: Tank Supports	118
APPENDIX B ALL 6 MIL RADIAL CLEARANCE DATA.....	122
APPENDIX C ALL MIL RADIAL CLEARANCE DATA.....	138

LIST OF FIGURES

FIGURE	Page
1. Material hardness of different materials on the Mohs scale [1].....	6
2. BHI WJE-1000 ESP that experienced an accelerated erosion study [2]....	9
3. Bearing OD measurements after 185 of erosion testing [2].....	10
4. Tangential abrasive marks after 185 hours of erosion testing [2].....	11
5. Uniformly distributed hair line fractures as seen under a microscope [2].	12
6. P & ID for the ESP journal bearing testing apparatus.	13
7. Complete bearing testing apparatus	14
8. Dimensions of the WJE 1000 pump [3].....	15
9. The designed shaft and disk assembly.	17
10. The designed imbalance disk made of stainless steel.	18
11. Model of shaft with imbalance disk [2].	19
12. Simulation results of orbits [2].....	20
13. Real experimental results of orbits [1].	20
14. Simulation results of load at 6 mil radius clearance [2].....	22
15. Cross section view of testing chamber attached to mounting plate.	25
16. Top view of instrumentation that surround the ESP journal bearing.....	28
17. Assembly of instrumentation locations.....	29
18. Testing stand that houses the motor, shaft, and testing chamber.	30
19. The motor mount and adjustment mechanisms.....	32
20. Roller bearing support assembly	33

21.	The splash guard that will contain the leakage through the bearing.	34
22.	The linear bearings that allow the testing chamber to be moved.	36
23.	Pump curve for replenishing loop with design point highlighted [5].	38
24.	Pump curve for the recirculation loop diaphragm pump [7].	39
25.	The liquid storage tank (left) and sand settling tank (right).	41
26.	The sand administration system to add sand to the flow.	42
27.	The stepper motor that drives the sand administration system.	43
28.	Instrumentation flow chart.	46
29.	Device selection details.	47
30.	Control diagram of the stepper motor and VFD	48
31.	Facility location at the turbomachinery lab at Texas A&M University,	49
32.	The insulated shed that serves as the facility office.	50
33.	The testing tray that was constructed to contain liquid leakage.	51
34.	Control hardware installed on a rack (backside view)	52
35.	Complete assembly	53
36.	Orbit measurements of the 6 mil bearing at different speeds.	56
37.	Pressure distribution as a function of angle for the 6 mil bearing.	57
38.	Radial load as a function of angle for each of the load cells.	58
39.	Position, force, and pressure for 6 mil bearing at 3600 RPM	60
40.	Relationship between position and pressure for the 6 mil bearing.	61
41.	Prediction and measured pressure for the 6 mil bearing at 1200 RPM.	63
42.	Prediction and measured pressure for the 6 mil bearing at 3600 RPM.	64

43.	Orbits of the 12.5 mil bearing at different speeds	66
44.	Pressure as a function of angle for the 12.5 mil bearing.....	67
45.	Radial load as a function of angle for each of the load cells.....	68
46.	Position, force, and pressure for 12.5 mil bearing at 3600 RPM.....	70
47.	Relationship between position and pressure for the 12.5 mil bearing.	71
48.	Prediction and measured pressure for the 12.5 mil bearing at 1800 RPM.	72
49.	Prediction and measured pressure for the 12.5 mil bearing at 3000 RPM.	73
50.	Orbit Comparison to WJE-1000 Pump at 6 mil bearing, 3600 RPM.....	74
51.	Waterfall plot of the frequency spectrum for the 6 mil bearing.....	76
52.	Waterfall plot of the frequency spectrum for the 12.5 mil bearing.....	76
53.	The testing chamber lowered to inspect the journal bearing.....	77
54.	The borescope setup to take photographs of the bushing surface	78
55.	The borescope taking a picture of the bushing surface ID.....	78
56.	A photograph of the bushing ID taken with the borescope.....	79
57.	A photograph of the 12.5 mil brass bearing OD surface.....	80
58.	6 mil radial clearance orbit at 600 RPM	122
59.	6 mil radial clearance orbit at 1200 RPM	122
60.	6 mil radial clearance orbit at 1800 RPM	123
61.	6 mil radial clearance orbit at 2400 RPM	123
62.	6 mil radial clearance orbit at 3000 RPM	124
63.	6 mil radial clearance orbit at 3600 RPM	124
64.	6 mil radial clearance radial loads at 600 RPM	125

65.	6 mil radial clearance radial loads at 1200 RPM	125
66.	6 mil radial clearance radial loads at 1800 RPM	126
67.	6 mil radial clearance radial loads at 2400 RPM	126
68.	6 mil radial clearance radial loads at 3000 RPM	127
69.	6 mil radial clearance radial loads at 3600 RPM	127
70.	6 mil radial clearance annulus pressure at 600 RPM	128
71.	6 mil radial clearance annulus pressure at 1200 RPM	128
72.	6 mil radial clearance annulus pressure at 1800 RPM	129
73.	6 mil radial clearance annulus pressure at 2400 RPM	129
74.	6 mil radial clearance annulus pressure at 3000 RPM	130
75.	6 mil radial clearance annulus pressure at 3600 RPM	130
76.	6 mil orbit comparison as a function of speed	131
77.	6 mil radial clearance pressure comparison as a function of angle	131
78.	6 mil predicted compared to measured pressure at 600 RPM.....	132
79.	6 mil predicted compared to measured pressure at 1200 RPM.....	132
80.	6 mil predicted compared to measured pressure at 1800 RPM.....	133
81.	6 mil predicted compared to measured pressure at 2400 RPM.....	133
82.	6 mil predicted compared to measured pressure at 3000 RPM.....	134
83.	6 mil predicted compared to measured pressure at 3600 RPM.....	134
84.	6 mil position, force, and pressure comparison at 600 RPM	135
85.	6 mil position, force, and pressure comparison at 1200 RPM	135
86.	6 mil position, force, and pressure comparison at 1800 RPM	136

87.	6 mil position, force, and pressure comparison at 2400 RPM	136
88.	6 mil position, force, and pressure comparison at 3000 RPM	137
89.	6 mil position, force, and pressure comparison at 3600 RPM	137
90.	12.5 mil radial clearance orbit at 600 RPM	138
91.	12.5 mil radial clearance orbit at 1200 RPM	138
92.	12.5 mil radial clearance orbit at 1800 RPM	139
93.	12.5 mil radial clearance orbit at 2400 RPM	139
94.	12.5 mil radial clearance orbit at 3000 RPM	140
95.	12.5 mil radial clearance orbit at 3600 RPM	140
96.	12.5 mil radial clearance radial loads at 600 RPM	141
97.	12.5 mil radial clearance radial loads at 1200 RPM	141
98.	12.5 mil radial clearance radial loads at 1800 RPM	142
99.	12.5 mil radial clearance radial loads at 2400 RPM	142
100.	12.5 mil radial clearance radial loads at 3000 RPM	143
101.	12.5 mil radial clearance radial loads at 3600 RPM	143
102.	12.5 mil radial clearance annulus pressure at 600 RPM	144
103.	12.5 mil radial clearance annulus pressure at 1200 RPM	144
104.	12.5 mil radial clearance annulus pressure at 1800 RPM	145
105.	12.5 mil radial clearance annulus pressure at 2400 RPM	145
106.	12.5 mil radial clearance annulus pressure at 3000 RPM	146
107.	12.5 mil radial clearance annulus pressure at 3600 RPM	146
108.	12.5 mil orbit comparison as a function of speed	147

109.	12.5 mil pressure comparison as a function of angle	147
110.	12.5 mil predicted and measured pressure at 600 RPM.....	148
111.	12.5 mil predicted and measured pressure at 1200 RPM.....	148
112.	12.5 mil predicted and measured pressure at 1800 RPM.....	149
113.	12.5 mil predicted and measured pressure at 2400 RPM.....	149
114.	12.5 mil predicted and measured pressure at 3000 RPM.....	150
115.	12.5 mil predicted and measured pressure at 3600 RPM.....	150
116.	12.5 mil position, force, and pressure comparison at 600 RPM	151
117.	12.5 mil position, force, and pressure comparison at 1200 RPM	151
118.	12.5 mil position, force, and pressure comparison at 1800 RPM	152
119.	12.5 mil position, force, and pressure comparison at 2400 RPM	152
120.	12.5 mil position, force, and pressure comparison at 3000 RPM	153
121.	12.5 mil position, force, and pressure comparison at 3600 RPM	153

LIST OF TABLES

TABLE	Page
1. Comparison between simulation results and experimental results	21
2. List of instruments around the journal bearing.	26
3. Instruments that need to be controlled.	44
4. The data that needs to be acquired.	45
5. Operating data from the 6 mil radial clearance brass bearing test.	55
6. 6 mil bearing lead angle between pressure and minimum clearance.	61
7. The proportionality constants for each speed for the 6 mil bearing.	63
8. Operating data from the 12.5 mil radial clearance brass bearing test.	65
9. Comparison between the bearing's estimated eccentricity ratios	69
10. 12.5 mil bearing lead angle between pressure and minimum clearance.	71
11. The proportionality constants for each speed for the 12.5 mil bearing.	72

INTRODUCTION

Background

When an oil well is drilled, often times, the wellbore pressure is sufficient enough to overcome the pressure losses of the well and force the hydrocarbons to the surface.

Over time, as oil and gas is extracted from the well, the wellbore pressure drops and is not sufficient for the well to be economically viable. This can be reversed if the well is stimulated by means of artificial lift. The two most common ways to increase production from an oil well are by gas lifting or pumping.

Gas lifting is the process of injecting a gas into the well stream at some point within the well. Each well is different and has different flow requirements and therefore the means of gas lifting can be continuous gas injection or intermittent gas injection.

Another common way to increase well production is by pumping. One way of pumping is by means of a “sucker rod” pump. This type of pump is a positive displacement pump that uses a plunger that is driven by a pivoting beam on the surface. Another method of pumping makes use of a rodless pump called an electric submersible pump (ESP).

An ESP is a multistage centrifugal pump driven by a submerged electric motor powered by electricity from the surface. The first ESP was invented by Russian born immigrant Armais Artunoff and patented in the United States in 1926. The first ESP was installed in the El Dorado field in Kansas in 1926 [1]. Today, ESPs are used in onshore and offshore wells because of their capability to move large liquid volumes.

The range of liquid rates for a typical ESP installation is between 200 and 50,000 barrels per day and they can be installed at a depth between 1000 and 10,000 feet. ESPs have many advantages, however they also have some disadvantages and limitations. Some of the advantages are low maintenance (if installed properly) and they are well suited for offshore applications because they do not require much space. The use of an ESP is limited to locations where electricity is readily available. A couple of disadvantages associated with this type of artificial lift is that sand in the flow wears on the equipment and repair is difficult and costly because it must be pulled out of the well.

An ESP is a centrifugal pump comprised of a motor and, in some cases, hundreds of impellers and diffusers. The entire pump is submerged in the wellbore working fluid. The entire pump body, including the motor, is cooled by the working fluid moving past the various components. This aids in avoiding cavitation and lubricates the pumps moving components. The pump creates a pressure rise that pushes the fluid from the bottom of the well to the surface. Pushing the fluid creates a greater potential for pressure rise than pulling the fluid.

Each stage of the multistage centrifugal pump is comprised of an impeller and a diffuser. The impeller is fixed to the shaft and the diffuser is stationary. The impeller rotates and adds kinetic energy to the wellbore fluid. Each diffuser is stacked directly above each impeller. The purpose of the diffuser is to slow the fluid down, thereby increasing the pressure. This process is repeated for each stage of the pump.

Engineers in the oil industry anticipate particles in wellbore fluid and devised a way to remove most of these particles before they reach the ESP by means of a sand control. Typical sand control consists of screens and gravel packs. These measures are efficient in removing most particles in the flow, however small particles and hydraulic fracturing sand are often too small to be caught by these pieces of equipment. This presents a problem because all of the fluid coming out of the well travels through the ESP. When these particles travel through the pump, they damage the bearings, shaft, and other components in the pump. This is one cause of ESP failure during operation.

There is a financial incentive for research that prolongs the useful life of ESPs. This is primarily due to the fact that they are becoming increasingly more utilized in offshore oil fields. The cost of maintaining an offshore oil well is incredibly expensive due to the price of offshore rig time. Currently, there is no baseline for how long an ESP will last and there are no indications as to when a pump is approaching the end of its useful life. Depending upon ocean depth and the depth of the well, it could cost up to forty times the price of the ESP to replace a pump that has failed in an offshore well.

One of the ways to prolong the useful life of an ESP is to prolong the life of the bearings inside the pump. It is known that sand particles within the working fluid have detrimental effects on the bearings. In order to design a bearing with a longer useful life, quantifiable values must be determined to provide design constraints.

Problem Statement

This thesis will describe the experimental apparatus that was designed and constructed to study the effects of fine sands on ESP bearings. The objective is to be able to replicate the operating conditions of an ESP independent of the pump. This will allow for individual bearings to be tested and evaluated to determine a more viable option than the status quo. This will create an opportunity to improve the current bearings found in ESPs and ultimately prolong its life from an unpredictable amount of time to a predictable amount of time. This work will provide the details of the testing apparatus design, procedures to be used in experiments, and validate the design for future use. Due to time constraints, and the magnitude of this study, the scope of this work only includes the design, construction, and validation.

LITERATURE REVIEW

According to the Electric Submersible Pump Manual [1], the possible wear points where sand has an effect in ESPs are erosion in the pump stage, abrasion in radial bearings (radial wear), and abrasion in thrust washers and thrust bearings (axial wear). As sand particles enter the bearing clearance, they are crushed and material is removed from the bearing surface. The wear rate of the bearings is heavily dependent upon the flow rate through the pump. This is because as flow rate increases, the amount of sand that travels through the bearing increases leading to more material being removed from the surface [1].

As the amount of material removed from the bearing surface increases, the bearing clearance increases causing the whirl orbit to increase. As the whirl radius increases, the radial loads experienced by the pump increase and the rate of erosion increases. This also increases radial vibrations which have catastrophic effects leading to pump failure.

Pump modifications have been made to combat this deficiency with the ultimate goal of making any parts susceptible to erosion out of a harder material than sand. In the design process, the materials that are considered are harder than sand or quartz. Figure 1 shows the material hardness of several different materials on the Mohs scale [1]. It can be seen that ordinary steel is not hard enough to resist erosion from sand. This is an indication as to why current ESP bearings are made of tungsten carbide.

Contradicting this thought, softer more flexible materials such as rubber could be used in journal bearings. The resilient properties of such a material allow for sand

particles to enter the clearance and just bounce off without removing any material. Additionally, sand particles don't become imbedded in the material and simply work their way out of the bearing leading to less wear on the journal.

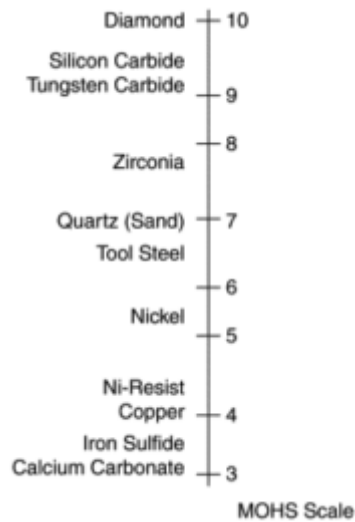


Figure 1: Material hardness of different materials on the Mohs scale [1]

Swierczek of Greene, Tweed & Co. published an article related to the vertical water pump bearings suggesting that polyetheretherketone (PEEK) based material showed considerable resistance to abrasive particle induced erosion. The original bronze bearings found in these water pumps were very susceptible to abrasive particles and the mean time between failures (MTBF) was approximately two years. Upon replacing the bearings with a PEEK based material, the MTBF increased to more than five years. Additionally, this thermoplastic composite provide non-galling, non-seizing properties

and a low coefficient of friction that allowed the pump to run in off-curve conditions (dry run or excessive vibration) [2].

In 2013, Zheng conducted an accelerated erosion study on the Baker Hughes WJE-1000 ESP with tungsten carbide bearings at the Texas A&M Turbomachinery Lab. During the study, a 100 mesh sand concentration of 2 grams/Liter was held constant to determine the erosion effects on different parts of the pump. This sand slurry concentration is approximately ten times the most severe condition encountered in the field. The reason for such a high concentration was so that the experiment could be conducted in a timely manner. The WJE-1000 pump was run for 117 hours with sand and water as the working fluid (two phase flow). Afterwards, the pump was run for 65 additional hours at 15% GVF (three phase flow).

Throughout the study, the pump was disassembled to quantify the effects of erosion. Figure 2 shows a cross sectional view of the different components found in the pump that Zheng used. Several notable things were found from this study. The bearing clearances increased with time. The three phase flow had a much larger impact on the rate of bearing radial clearance over time. Figure 3 shows that the impact of the erosion was not axially uniform along the bearing. The erosion caused a tapered effect on the bearings [3].

Zheng also found that as the tungsten carbide bearings eroded, wear in the tangential direction became visually detectable. When the bearings were examined under a microscope, the existence of hairline fractures became apparent. Abrasive wear

grooves having similar width to the sand particles were present in the tangential direction. This was clearly induced by the lodging of a sand particle in the bearing annulus. Hair line fractures of similar width showed up under a microscope, only these were in the axial direction and uniformly distributed. It was determined that the uniformity of the hair line fractures indicated that they were not due to individual sand particles. A possible explanation was the onset of fatigue failure due to the direct contact of tungsten carbide on itself (bushing and bearing collision). Figure 4 shows the tangential abrasive wear grooves and Figure 5 shows the uniform hair line fractures [3].

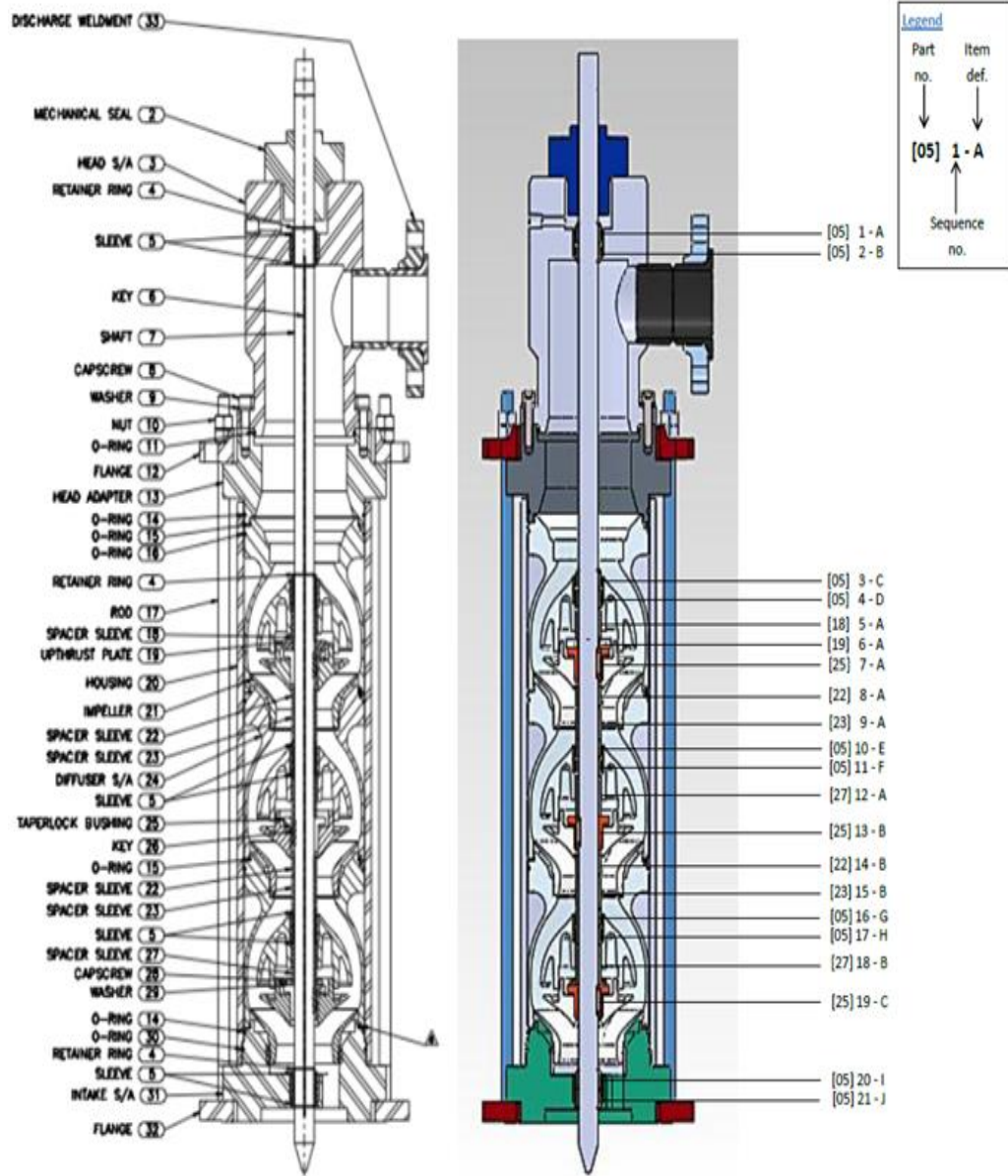


Figure 2: BHI WJE-1000 ESP that experienced an accelerated erosion study [2]

Tapered Edge on Bearing

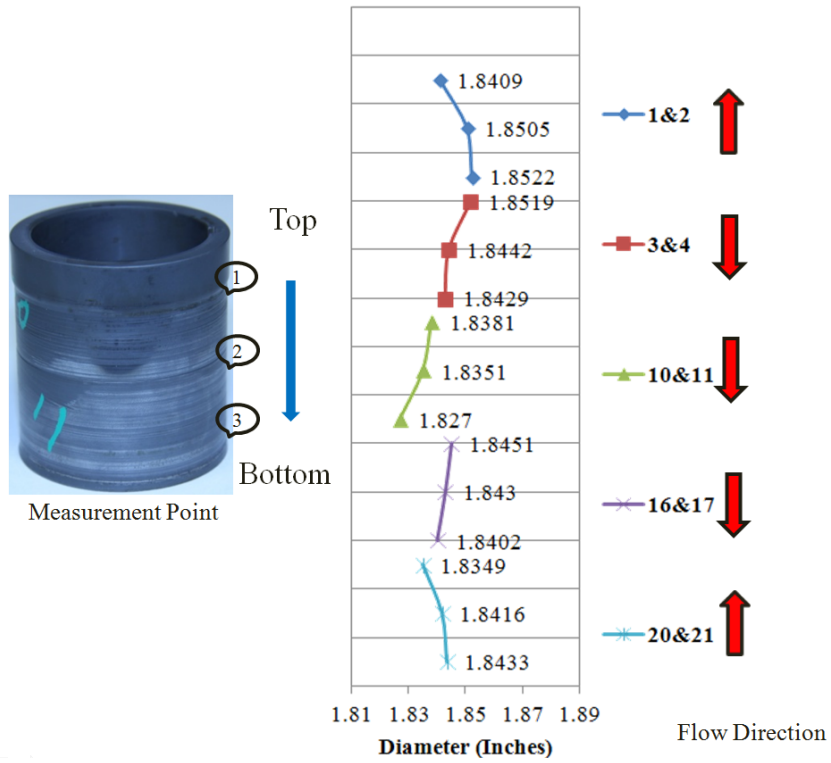


Figure 3: Bearing OD measurements after 185 of erosion testing [2].

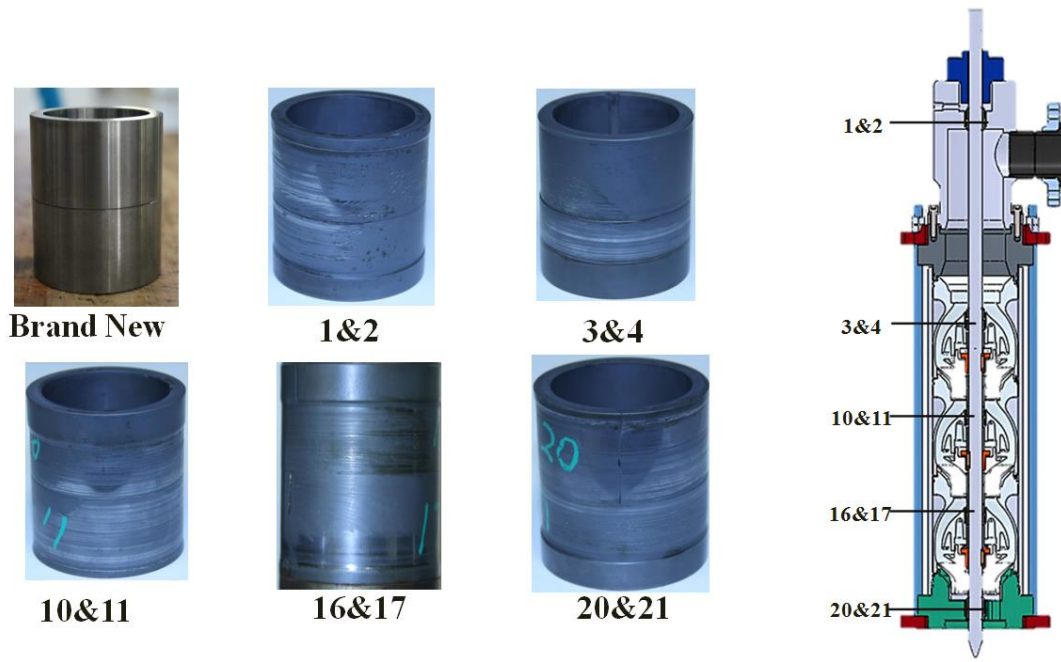


Figure 4: Tangential abrasive marks after 185 hours of erosion testing [2].

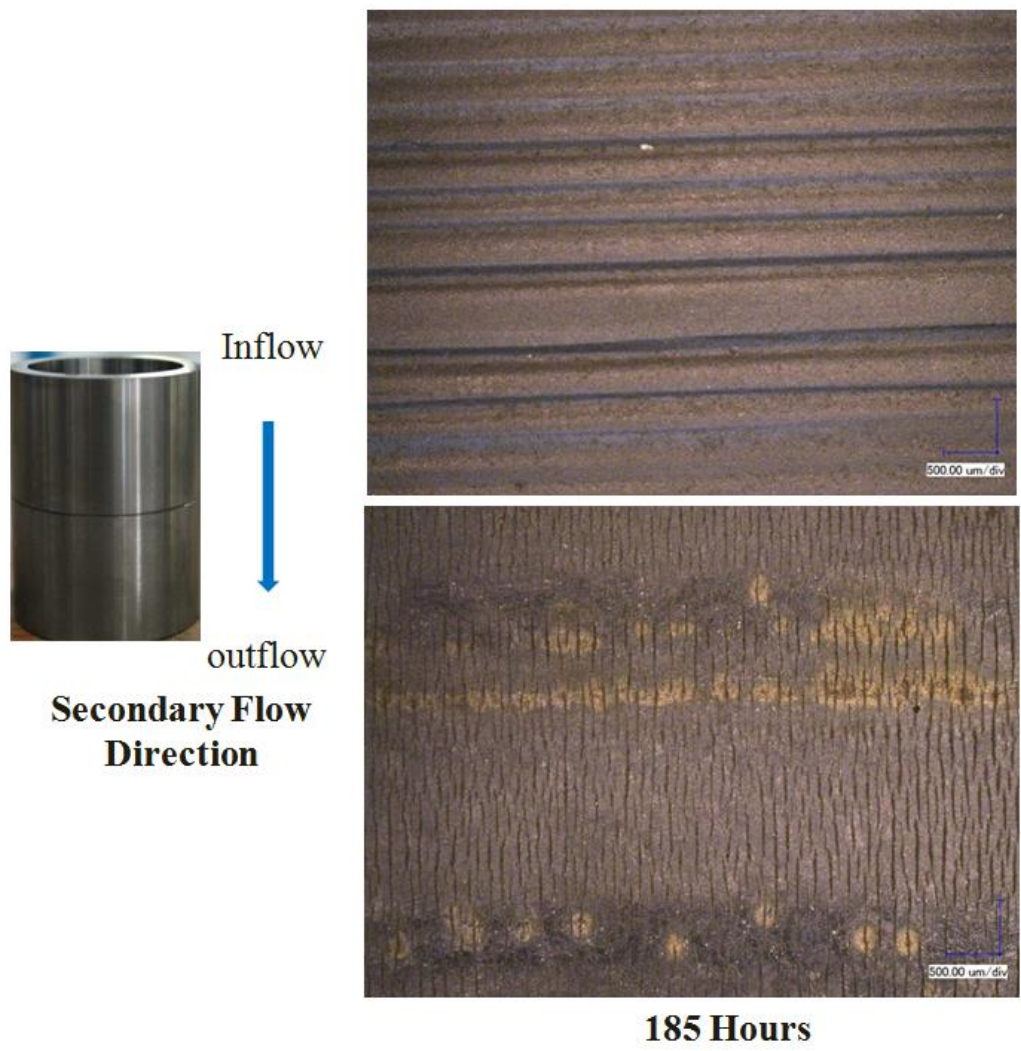


Figure 5: Uniformly distributed hair line fractures as seen under a microscope [2].

DESCRIPTION OF FACILITY

Overall Configuration

The piping and instrumentation diagram (P&ID) for the testing apparatus is shown in Figure 6. An overview of the fully designed bearing testing apparatus is shown below in Figure 7.

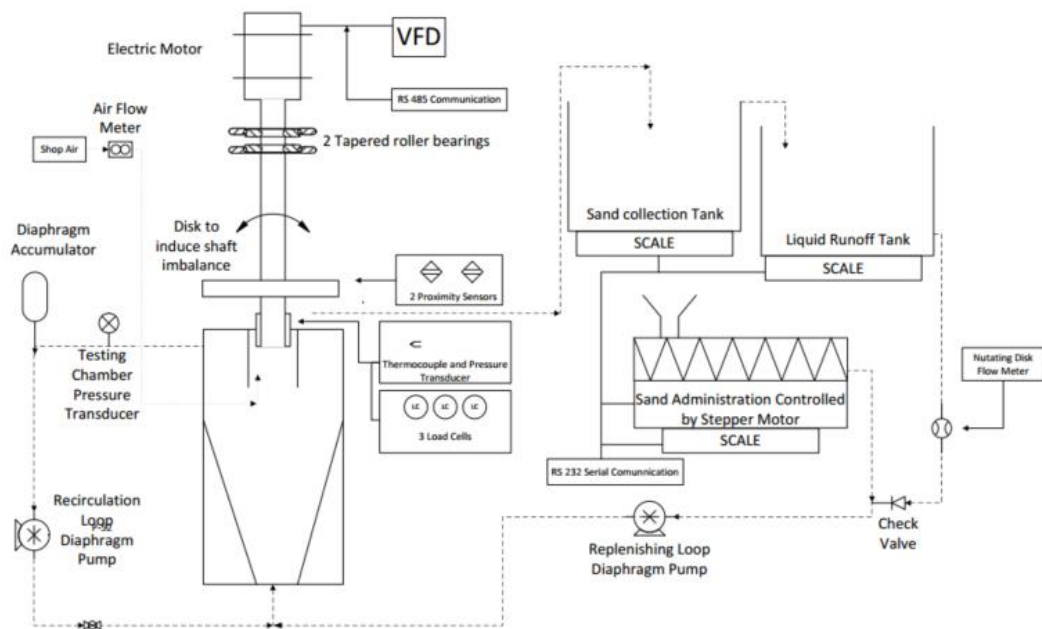


Figure 6: P & ID for the ESP journal bearing testing apparatus.

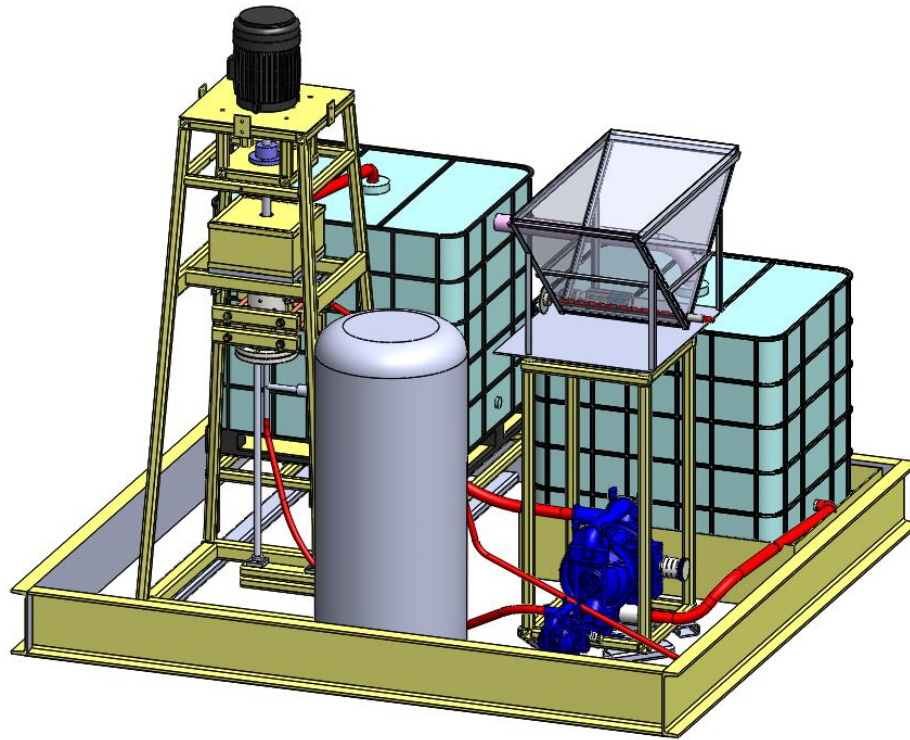


Figure 7: Complete bearing testing apparatus

The design process broke the entire system into several subsystems. These subsystems are listed below and a detailed description of each section is described in the following sections.

1. Rotor Dynamics
2. Testing Chamber
3. Apparatus Testing Stand
4. Fluid Movement
5. Sand Settling and Fluid Storage Tanks
6. Sand Administration
7. Controls

Rotor Dynamics

A shaft with an imbalance disk was designed to imitate the rotating motion of a shaft in a real pump. The disk was designed to produce similar motion of the shaft and impeller of the WJE-1000 pump [3]. An erosion study was conducted on this pump in previous experiments. The goal was to design an unbalanced disk to exhibit the same orbit characteristics as the impeller of the pump.

The dimensions of the second stage of the WJE-1000 pump are shown below in Figure 8. The mass of each impeller is 13.55 lb. The distance between the impeller and the bottom journal bearing is 3.00 inches and the distance between impeller and top journal bearing is 1.875 inches.

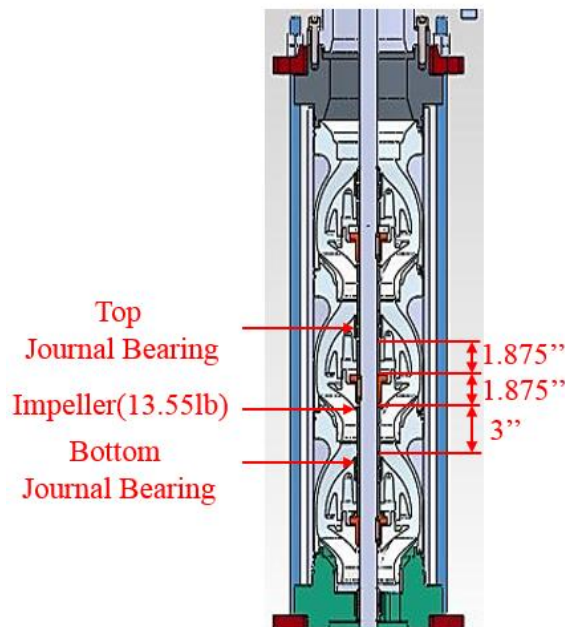


Figure 8: Dimensions of the WJE 1000 pump [3].

The designed shaft and disk assembly is shown in Figure 9. The designed shaft diameter has the same diameter of the WJE-1000 pump- 1.50 inches. The design includes two tapered roller bearing on the top. These bearings are used to support the weight of shaft and disk and to fix the shaft to avoid radial motion and vibration. The ESP journal bearing that will be tested will be fixed to the bottom of the shaft. The distance between the disk and the lower tapered roller bearing is 12 inches. The distance between the bottom of the disk and the journal bearing is 3 inches. This distance is the same as the distance between the impeller and the journal bearing in the WJE-1000 pump. Figure 9 shows four snap ring grooves. The uppermost snap ring groove is to constrain the coupling between the shaft and the motor. The second groove is to constrain the shaft to the bottom of the lower tapered roller bearing, and the bottom two snap rings are to constrain the ESP journal bearing in the axial direction. A keyway was also designed into the shaft to prevent the ESP journal bearing from moving in the circumferential direction.

The disk that was used to create a shaft imbalance is shown in Figure 10. The outside diameter of the disk is 7 inches and the height is 1.35 inches. The material of the disk was chosen as stainless steel to prevent corrosion from affecting the imbalance of the disk. There are sixteen threaded holes along the mid-plane of the disk that will allow for the disk imbalance to be finely adjusted via set screws. The diameter of these holes is 7/16 inch and the depth of each hole is 1.75 inches. The dimensions of these imbalance holes allow for an adjustable maximum mass eccentricity of the disk to be 0.099 inch.

The disk attaches to the shaft by a heavy duty flush-mount screw clamp bearing similar to those used to attach a pulley to a shaft. The screws in this bushing are tightened and pressure is applied on OD of the shaft and the ID of the imbalance disk hole until they cannot move independent of each other.

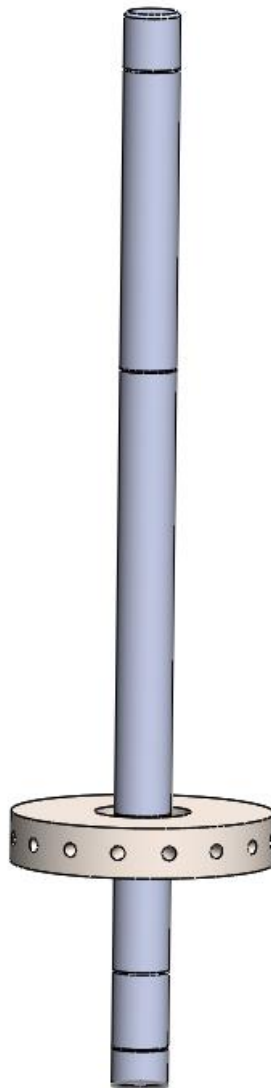


Figure 9: The designed shaft and disk assembly.

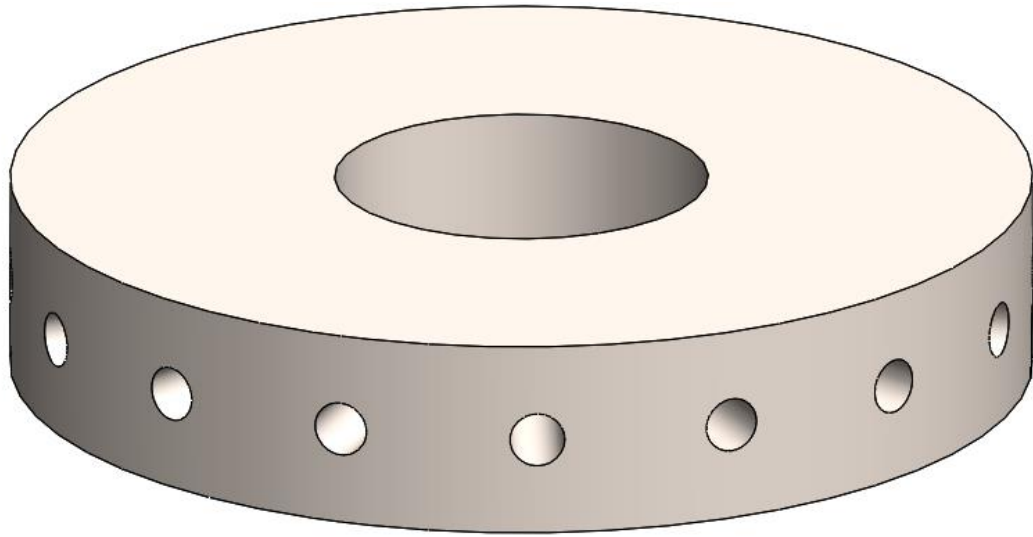


Figure 10: The designed imbalance disk made of stainless steel.

XLTRC2 Simulation

The design of the shaft and imbalance disk was conducted and validated by conducting rotor dynamic simulations with XLTRC2 software. XLTRC2 is a software developed by researchers at the Turbomachinery Lab at Texas A&M University to analyze rotor dynamics [4]. It has the capability to simulate the rotational motion of the shaft, disk, roller bearings, and journal bearing. The simulation results were compared to experimental data from the WJE-1000 pump for design validation [1].

The model that was used in the XLTRC2 simulation is shown in Figure 11. The roller bearings, imbalance disk, and journal bearing are included in the model.

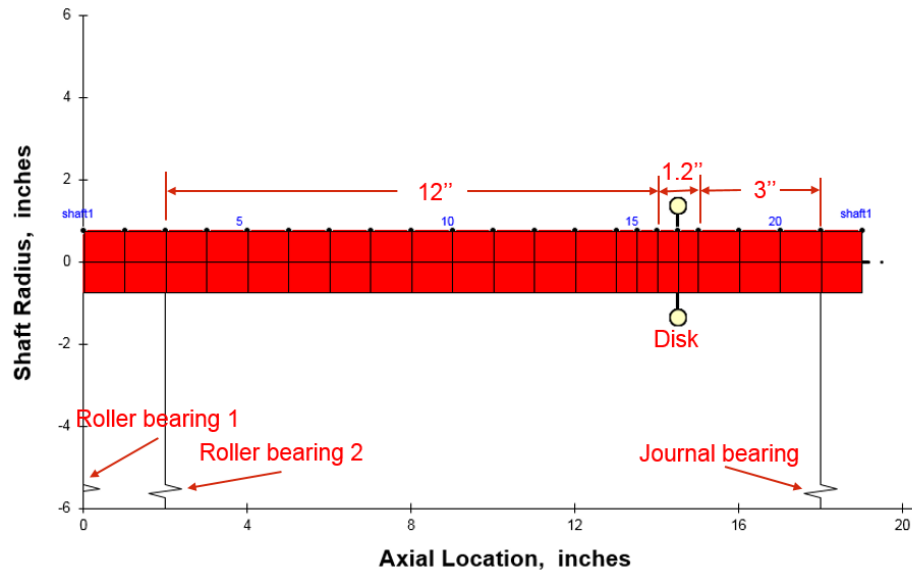


Figure 11: Model of shaft with imbalance disk [2].

The conditions that were used in the XLTRC2 simulation are as follows:

- 1) Shaft speed: 3600 RPM
- 2) Journal bearing radial annular clearance between sleeve and bushing: 6 mils
- 3) Disk mass: 11.71 lb
- 4) Disk eccentricity: 0.085 inch

The simulation delivered results in the form of rotational orbits. These results are shown in Figure 12. The left plot figure in Figure 12 is the orbit of the disk and the right plot is the orbit of the journal bearing. The experimental results from the WJE-1000 erosion study are shown in Figure 13 [1]. The experiment was conducted at 3600RPM with a nominal journal bearing clearance of 6 mils at the beginning of the experiment (at time = 0 hour). The left plot in Figure 13 is the orbit of impeller 2 and the right plot is the orbit of the journal bearing under impeller 2. The orbit of impeller 2 has two

extensions which were caused by a notch that was made in the impeller to make sure the proximity probes were functional and can be neglected. The circle in the figure is the actual orbit of impeller 2.

The comparison between the simulation results and experimental results is shown in Table 1.

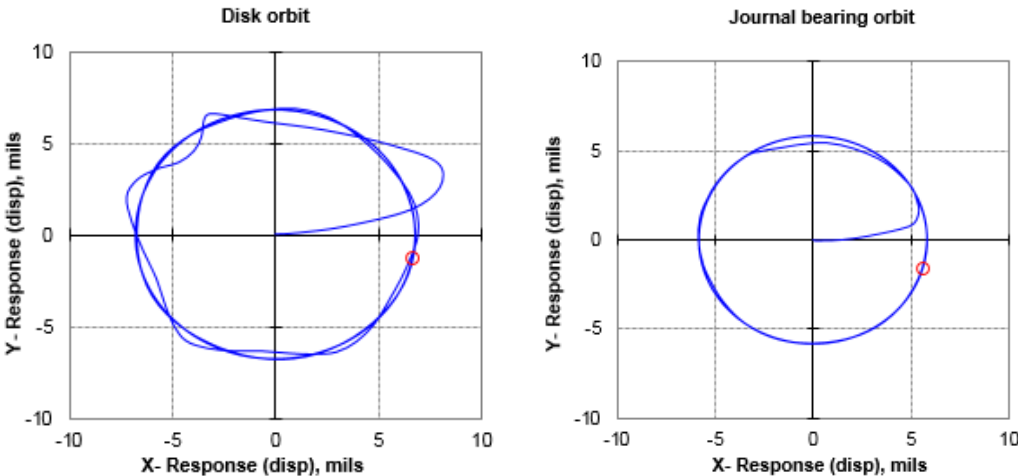


Figure 12: Simulation results of orbits [2].

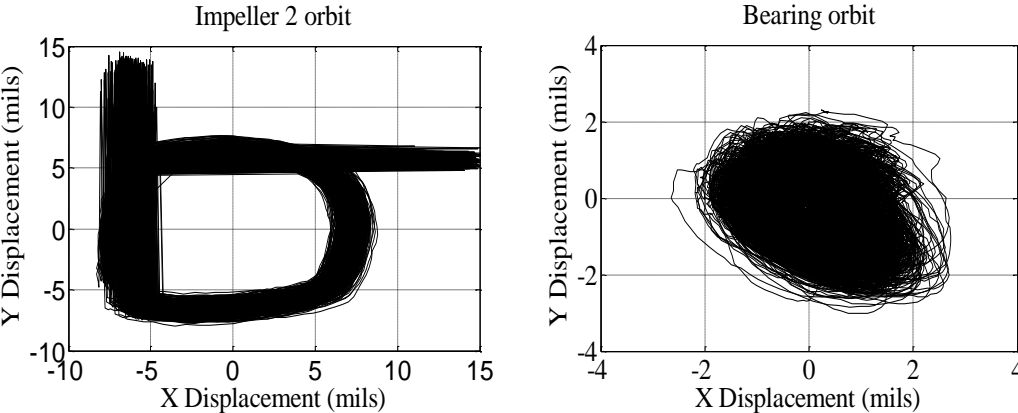


Figure 13: Real experimental results of orbits [1].

Table 1: Comparison between simulation results and experimental results

	Disk orbit radius (mil)	Bearing orbit radius (mil)
Real experiment	8	2.5
Simulation 1 (6 mil radial clearance)	7.5	6

Table 1 shows that the designed imbalance disk can simulate the motion of an ESP impeller at 3600 RPM and 6 mil radius clearance. In addition to orbit simulation, the XLTRC2 software can also determine the loads exerted on the roller bearings and journal bearing. This information provided a basis for selecting the proper roller bearings as well instrumentation for measurement (discussed further down). The simulation results of bearing loading on each bearing when the journal bearing radial annulus clearance is 6 mils is shown in Figure 14. The load determinations from the simulation provided a basis for selecting the range of the instrumentation that would be required for experimental tests.

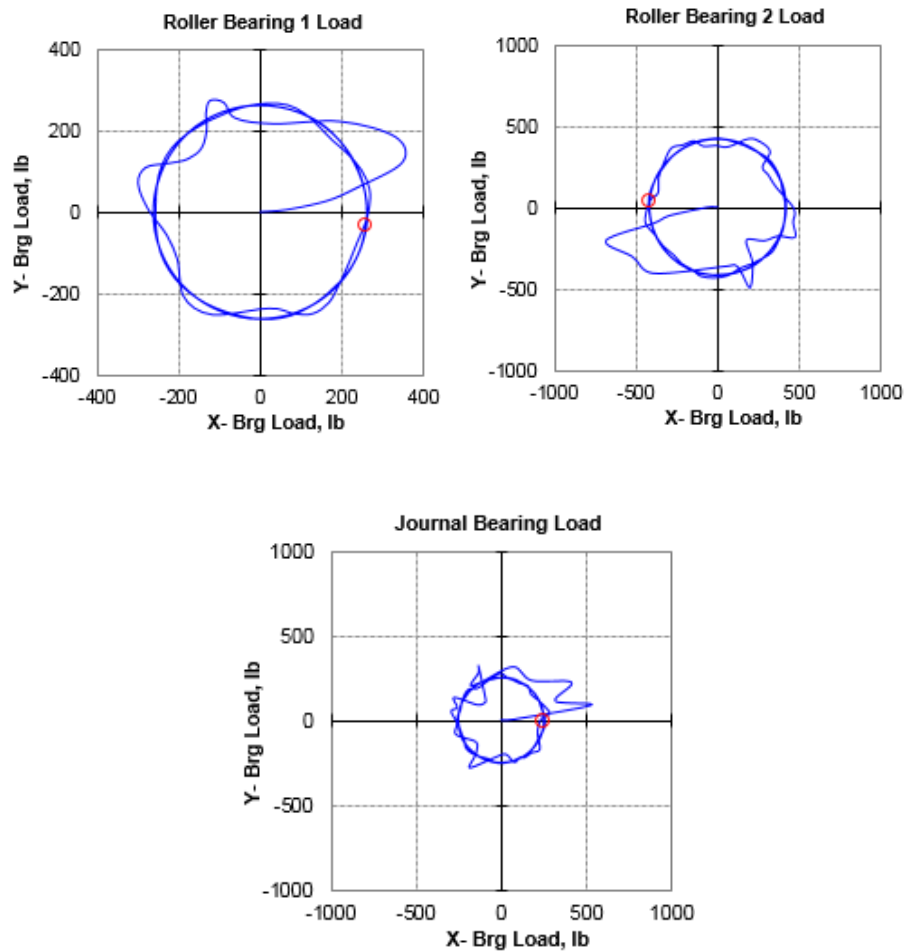


Figure 14: Simulation results of load at 6 mil radius clearance [2].

Sommerfeld Theory

XLTRC2 simulated the anticipated bearing loading conditions at various operating conditions. These loading conditions were important when selecting instrumentation for measurement during bearing testing. In addition to measuring the load exerted on the journal bearings, the pressure distribution in the journal bearing annulus is also of interest. This information provide a pressure distribution as a function of rotation angle that can serve as indication of normal stress exerted on the bearing/bushing surface.

This information is critical to future bearing designs, and could allow for a different bearing material selection to extend the life of the bearing.

A known pressure distribution around the bearing could be correlated with measured loads exerted on the bearing to better understand how bearing erosion not only affects the radial clearance of the bearing, but also the pressure distribution and the loads exerted on the bearing. The Sommerfeld lubrication theory was used to determine the anticipated pressure distribution as a function of rotation angle [3]. Equation 1 and Equation 2 show how the pressure distribution is derived from the Sommerfeld theory. The variables listed in these two equations are listed below:

- R_c = Radius of the journal bearing
- c = Clearance of the journal bearing.
- ϵ = Eccentricity ratio (shaft eccentricity/ clearance)
- μ = Viscosity of the lubricant fluid
- Ω = Spin speed of the shaft
- P = Pressure in the bearing annulus
- θ = Rotation angle

$$c_p = \frac{\epsilon \sin(\theta) (2 + \epsilon \cos(\theta))}{(2 + \epsilon^2)(1 + \epsilon \cos(\theta))^2} \quad (1)$$

$$P = \frac{6 c_p \mu \Omega * R_c^2}{c^2} \quad (2)$$

Testing Chamber

The testing chamber serves as the heart of the entire testing apparatus. The testing chamber is where the journal bearing is fixed and generates the flow of liquid through the journal bearing annulus. Figure 15 shows a cross section view of the testing chamber attached to the plate from which it hangs. The testing chamber consists of several steel flanges connected by a 6 inch diameter steel pipe. The hole on the top flange of the testing chamber leads to the bushing and journal bearing. A liquid and sand mixture enters the bottom of the testing chamber and is forced upwards to one of two exits. Some of the liquid and sand mixture will be forced through the journal bearing annulus while some of the flow will be directed towards the hole on the left side of the testing chamber. This will ensure that the flow does not slow down and prohibit the sand from sinking to the bottom of the testing chamber. The fluid that exits through the side of the testing chamber will be recirculated and forced back through the entrance at the bottom of the testing chamber. There is a funnel shaped piece of steel welded inside of the testing chamber to force any sand that has fallen out of the flow due to gravity back into the main stream of the flow.

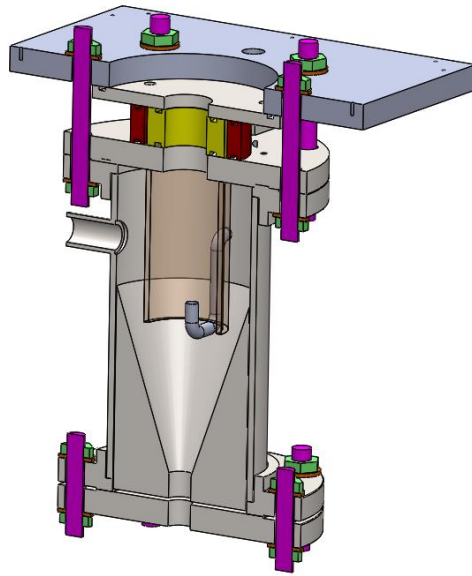


Figure 15: Cross section view of testing chamber attached to mounting plate.

The hole located on the back of the midsection of the testing chamber shown in Figure 15 will allow for a rigid tube carrying air to be inserted into the chamber. This tube will give the testing apparatus the capability to test bearings at different GVF. Once air is injected into the flow it will be directed inside the cylinder fixed to the top flange of the testing chamber. This cylinder will block any of the introduced air from escaping through the recirculation exit and ensure that an accurate GVF is being forced through the bearing.

The gap between the top flange of the testing chamber and the steel plate from which it will hang was designed into the system so that measurement instrumentation can be placed around the journal bearing that is being tested.

The instrumentation that was used to record measurements around the journal bearing is listed in Table 2. The data measured data is listed in the second column of the table.

Table 2: List of instruments around the journal bearing.

Instrument	Measured Data
Load Cells (3)	Radial Load exerted on the journal bearing
Flush Mount Thermocouple	Temperature in the bearing annulus
Flush Mount Pressure Transducer	Pressure as a function of rotation angle

The testing that was conducted in this study was done on several imitation bearings that were made of brass. A stainless steel bushing was designed and outfitted so that the instrumentation listed above recorded the appropriate data. Three brass bearings of decreasing OD's were machined to represent the progress of erosion on the ESP journal bearings.

The instrumentation listed above in Table 2 gave insight to the physical loading conditions that the journal bearing experiences while rotating. This was accomplished by maintaining a fixed bushing ID and changing the bearing OD so that the radial clearance can be changed to be 6, 12.5, and 25 mils. Imitation "bearings" were machined from brass having different OD's and fixed to the shaft where the actual bearing would be to imitate different radial clearances between the bearing and bushing.

A top view of the instrumentation locations described in Table 2 is shown and labeled in Figure 16. The three load cells are situated 120 degrees from each other on the same plane (mid plane of the bearing). They are 'button' type load cells that take

measurements from compressive loads by using a wheatstone bridge. The compressive nature of the load cells only allows for compressive load measurements to be taken, and therefore the load cells are backed by a block with a threaded hole. This block allows for a bolt to place a compressive load onto the load cells up to half of their rated load. Deviations from this compressive load in either direction will indicate that a tensile or compressive load is being exerted.

The thermocouple and pressure transducer are each situated on the same plane as the load cells. Each instrument is located 60 degrees from the closest two load cells. The thermocouple is flush mounted to the bushing ID and gives a temperature measurement in the annulus between the bearing and the bushing. The flush mount pressure transducer is mounted in a configuration that is slightly recessed from the bushing ID. This pressure transducer is of the dynamic type and gives the pressure distribution as a function of rotation angle. A hot-film probe can be used in future work to determine the wall shear stress in the annulus between the bearing and the bushing. This could provide important design information that would lead to a more promising bearing material.

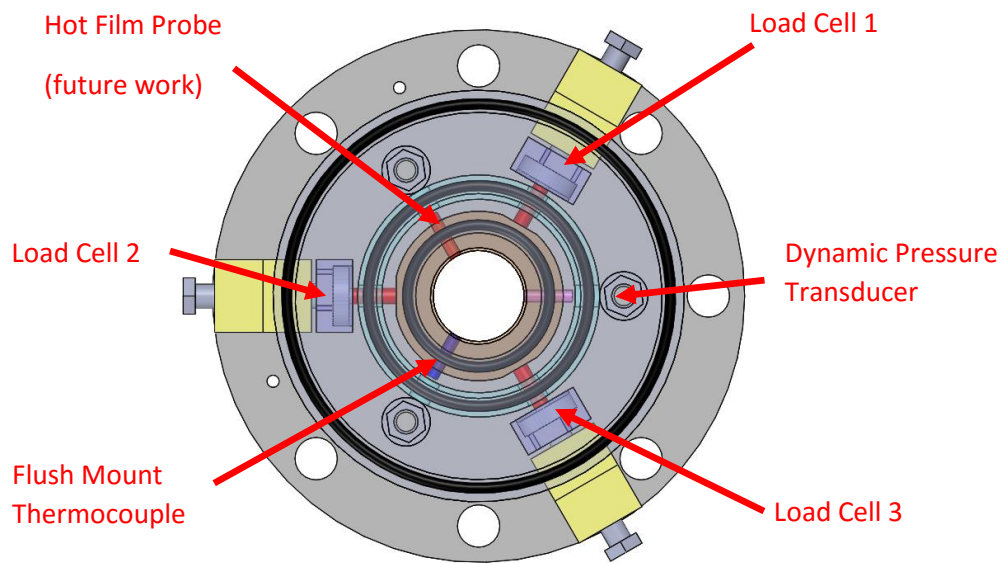


Figure 16: Top view of instrumentation that surround the ESP journal bearing

These measurements were taken to gain insight of the physical conditions that the bearing and bushing experience while operating. The data gathered from this test provides information as to how well the bearing exhibits the Sommerfeld behavior mentioned above, provides design constraints for ESP bearing materials, and establishes a portfolio of temperature, load, and pressure at different phases in an ESP journal bearing erosion lifespan. This information could be useful in quantifying a point of failure for an ESP journal bearing.

Figure 17 shows a cross section view of the assembly of the instrumentation mentioned above surrounding the journal bearing. All of the instrumentation is sandwiched between two plates. The bottom plate is the top flange of the testing chamber and the top plate secures the instrumentation in place. There are two concentric rings between these two plates that are floating on sets of O-rings. The inner ring

supports the pressure transducer and thermocouple and serves as the bushing for the imitation journal bearing. Three push rods are coincident with this inner ring that extend to the load cells outside of the outer ring. The reason for the outer ring is to ensure that the working fluid is contained within the testing chamber and only exits where it is supposed to. This protects the load cells from coming in contact with liquid. The top plate is bolted to the bottom plate with just enough force to cause the O-rings to seal, but not enough to cause resistance to the load cell measurements.

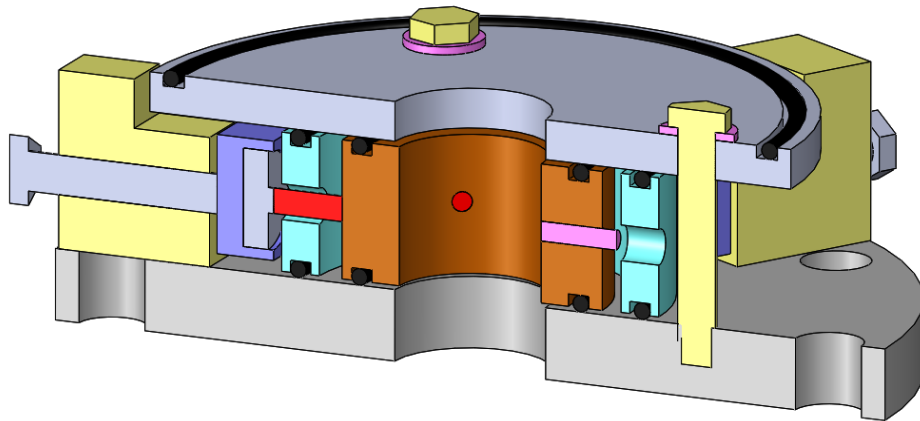


Figure 17: Assembly of instrumentation locations.

When testing an actual journal bearing, the flow will contain a concentration of sand (2 g/l) to intentionally erode the bearing and bushing. When this testing takes place, the inner ring will be replaced so that the bushing part of the actual bearing can be included in the test. This bushing must be slightly modified so that the dynamic pressure transducer and thermocouple can be used to collect data from the test.

Testing Stand

The backbone of the bearing testing apparatus is the testing stand which holds the motor, shaft, tapered roller bearings, and the bearing testing chamber. This testing stand is shown below in Figure 18.

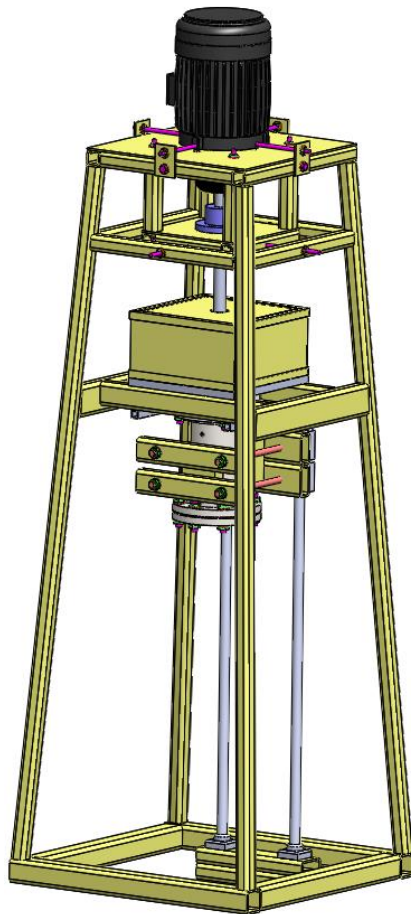


Figure 18: Testing stand that houses the motor, shaft, and testing chamber.

The testing stand was designed to be as rigid as possible so that any external movement does not affect the testing container. There are several key features that should be highlighted about the bearing testing stand.

The motor that turns the shaft and journal bearing is a custom order 40 HP motor that is capable of rotation at speeds up to 8000 RPM. The reason for such a high motor speed is because the project sponsor is interested in how the journal bearings behave at speeds up to 7200 RPM. The motor size was selected by calculating the losses associated with the different components in the system and applying a safety factor. The motor is driven by a variable frequency drive (VFD) so that the rotation speed can be adjusted to the desired operating conditions. The motor is mounted on top of the testing stand in such a way that it will be able to be aligned with the testing shaft and roller bearings. This adjustment mechanism is four bolts located orthogonally from each other allowing for adjustment in both the x and y direction. Adjustments in the z direction will be made by places shims underneath the motor. The motor and its mount is shown in Figure 19.

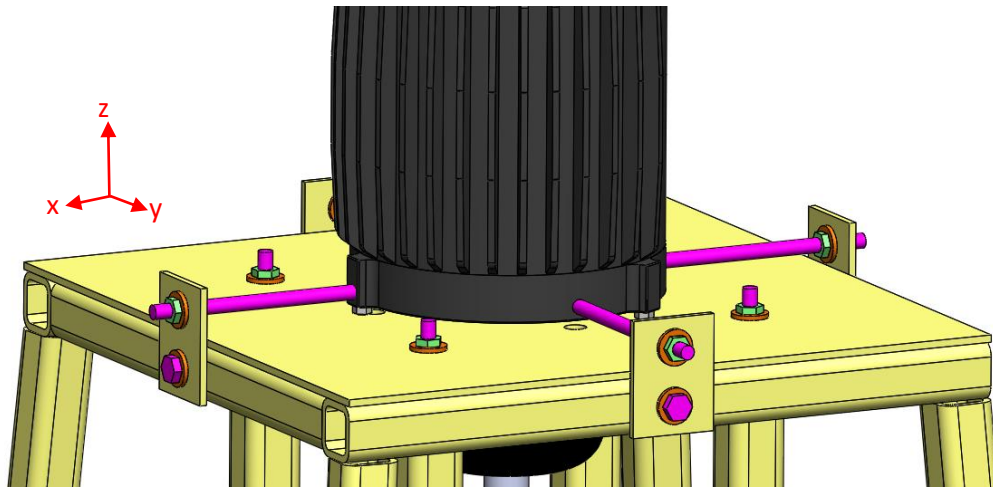


Figure 19: The motor mount and adjustment mechanisms.

The tapered roller bearing support is shown in Figure 20. The roller bearing support assembly contains the mount for both of the tapered roller bearings. Each bearing will be mounted on opposite sides of a steel plate. The reason there are two roller bearings is because it will create two points of contact on the shaft to ensure that it is completely vertical. The roller bearings are fixed to the shaft below the coupling between the shaft and the motor. Once the shaft is in place, a dial micrometer was used to adjust the position of the roller bearing support. The position of the support was adjusted in three directions to ensure that the roller bearings are concentric with the motor shaft and that the support plate is perpendicular to the shaft. These adjustments were made in the x and y direction by adjusting alignment bolts seen in Figure 20. Adjustment in the z direction was made by placing shims underneath the vertical rectangular structural steel members located on all four corners of the roller bearing support plate. There is a threaded rod running through the center of the vertical rectangular steel members that is used to fix the tapered roller bearing support plate in place once it is aligned properly.

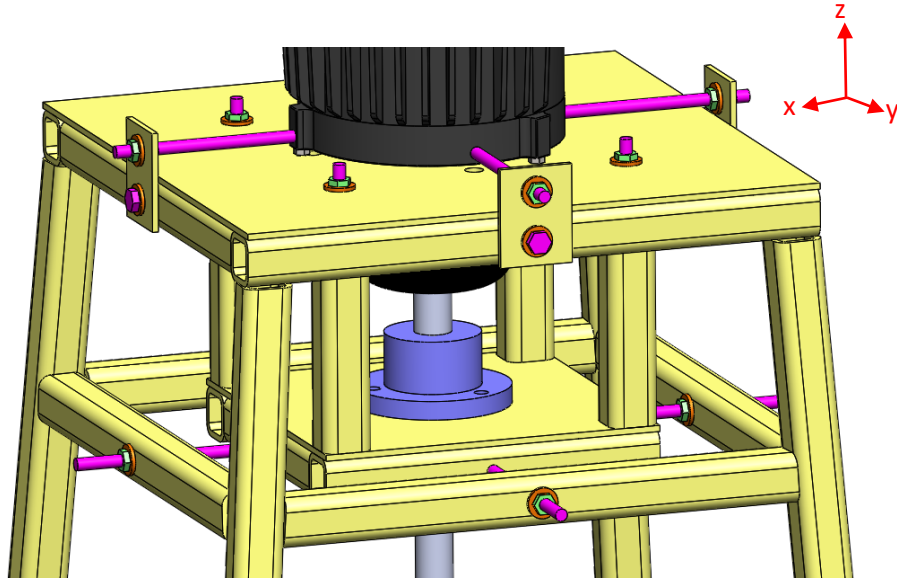


Figure 20: Roller bearing support assembly

When the bearing test apparatus is functioning, liquid (water or oil) combined with sand leaks through the annulus that exists between the journal bearing and bushing. This leakage must be contained so that it can be directed into the sand settling tank. In order to contain this leakage, a splash guard was designed that prevents the leakage flow from escaping to the environment. This splash guard is a metal box that is fixed to the testing stand above the testing chamber. This is shown in Figure 21. In the image shown, the sides of the splash guard assembly was made transparent for clarity. Once the liquid leaks through the journal bearing, it will be drained from the splash guard assembly into the sand settling tank.

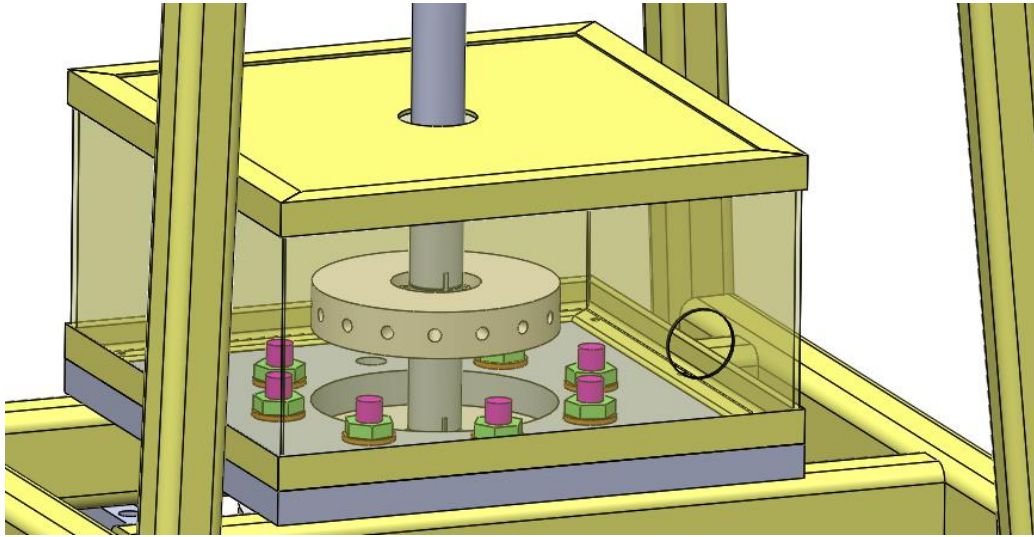


Figure 21: The splash guard that will contain the leakage through the bearing.

The testing that was conducted for this thesis proved the validity of this design and provided some room for improvement. When the shaft does not spin, the splash guard does its job very well. When the shaft starts spinning, the disk acts as an impeller and forces the liquid towards the outside edge of the box. When the liquid hits the outside of the box it is forced upward and some leaks through the lid of the box.

Recommendations for improvement are included in the conclusions section of this thesis.

The anticipated testing time for each journal bearing is 200 hours. During the testing time, visual and geometrical measurements will be taken. In order to take these measurements, the testing chamber must be lowered so that the OD of the journal bearing and the ID of the bushing are exposed. The bearing will remain fixed to the shaft and the bushing will remain fixed to the testing chamber. Once these faces are exposed, the bearing and bushing can be measured and photographed. The

measurements will be taken so that the bearing wear can be quantified. These measurements are taken with a micrometer and a set of telescoping gages. Photographs can be taken to examine the surfaces of both the bearing and the bushing. The ID of the bushing will be photographed with a borescope. The OD of the bearing will be photographed by using a microscope after it is removed from the shaft.

Previous experiments have shown that thermally induced hairline fractures exist on these surfaces due to friction [3]. These fractures became apparent after the bearings from the WJE-1000 pump underwent an erosion study. The hairline fractures were observed after examination under a microscope at 27X magnification. A borescope has been procured that can deliver such a magnification and will allow for photographs to be taken at discrete time intervals during the 200 hour test for each bearing. The linear bearings shown in Figure 22 establishes a way for the bearing and bushing to be measured without disassembling the entire testing apparatus.

When the testing chamber is lowered for bearing evaluation, it is moved from its original aligned position. In order to move the testing chamber back into its original position, a series of alignment pins with a tolerance of 1/10 of a mil are placed in the top of the testing chamber. These alignment pins correspond to a fixed position on the testing stand that allows for realignment to the original position for continued testing.

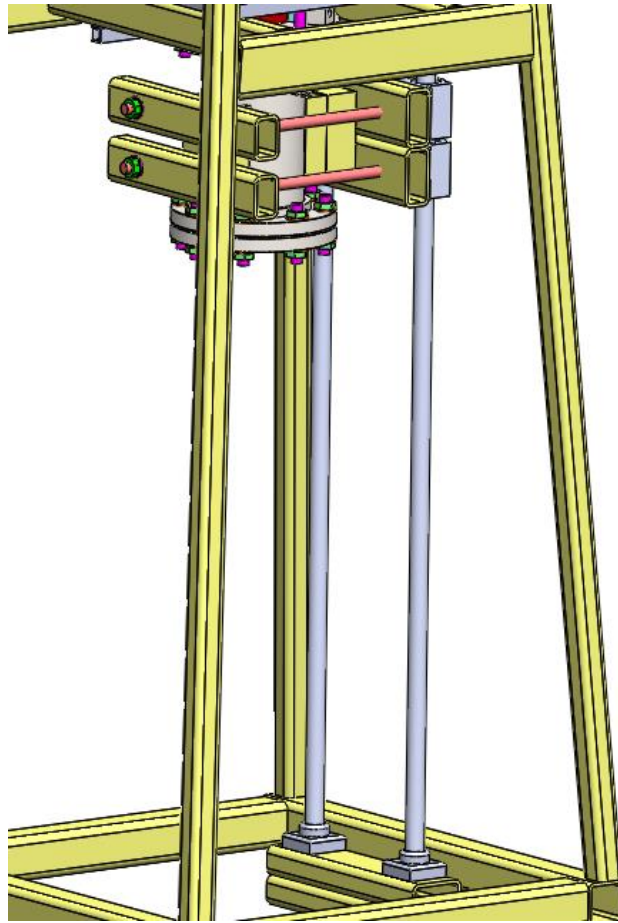


Figure 22: The linear bearings that allow the testing chamber to be moved.

Fluid Movement

As seen in the piping and instrument diagram in Figure 6 on page 12, the movement of liquid through the testing chamber consists of two loops. Liquid that exits the testing chamber through the clearance between the bearing and the bushing travels through the replenishing loop. Liquid that leaves the testing chamber through the pipe tap in the side travels through the recirculation loop and is moved back to the entrance of the testing chamber. Both loops are powered by pneumatic diaphragm pumps. This type of pump

was selected because preservation of the sand particles in the flow is important. A different type of pump other than a diaphragm pump would grind and crush the sand reducing its nominal particle size.

The role of the replenishing loop is to remove sand from the liquid that has traveled through the journal bearing annulus and replace it with fresh sand. CFD simulation of the journal bearing showed a minimum flow rate (3600 RPM, 6 mil radial clearance) of 12 gallons per minute (GPM) through the bearing annulus and a maximum flow rate (7200 RPM, 50 mil radial clearance) of 67 GPM through the bearing annulus. These values served as design parameters for the replenishing loop. Once the liquid-sand mixture flows through the bearing annulus, it is contained in the splash guard located above the testing chamber. The flow is drained into the sand settling tank where the sand falls at a faster rate than the liquid rises. This effectively removes the sand from the flow. The working fluid is then allowed to spill over into the liquid storage tank.

When the flow exits the liquid storage tank it is metered with a nutating disk (positive displacement) flow meter. After the flow meter, fresh sand is added through a stand pipe and pumped back to the inlet of the testing chamber. The selection of the replenishing loop diaphragm pump was made based on the anticipated minimum and maximum flow rate through the replenishing loop. The pump curve for this pump is shown below in Figure 23. The maximum flow rate design point is highlighted on the pump curve.

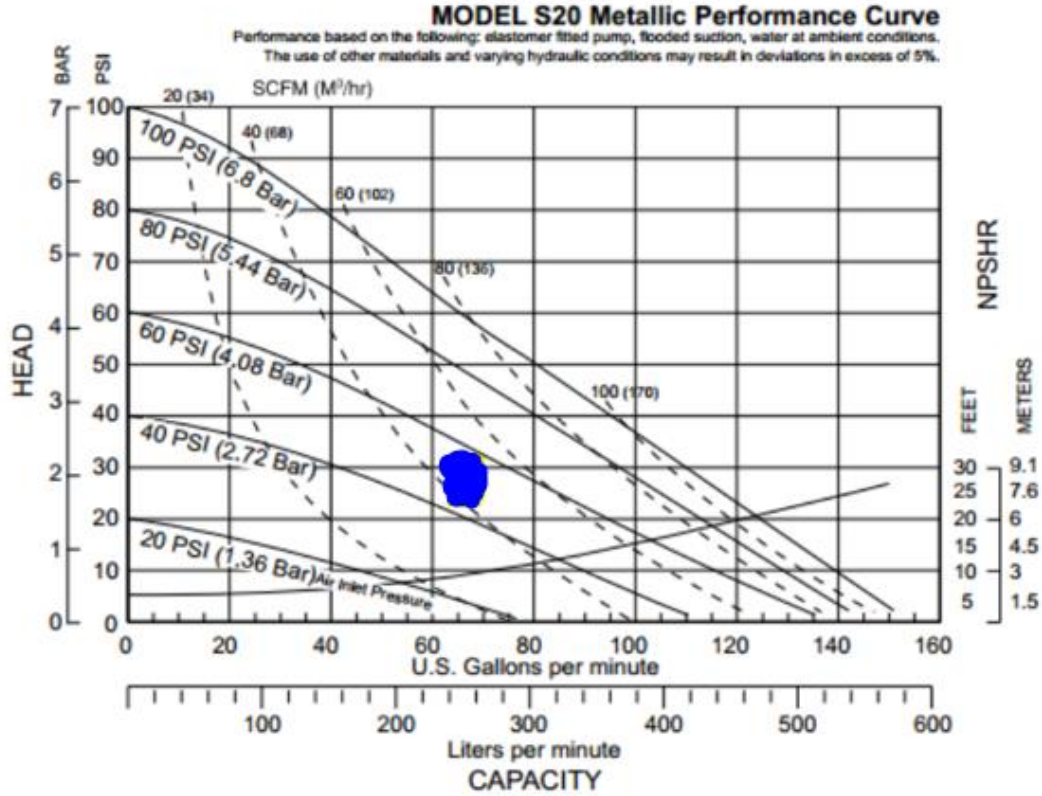


Figure 23: Pump curve for replenishing loop with design point highlighted [5].

To keep the liquid-sand mixture moving through the test chamber so that the sand does not settle out of the liquid, a recirculation loop was designed into the system. The flow rate for the recirculation loop was determined to be 12 GPM based on the sand settling speed and the dimensions of the testing chamber [6]. The recirculation loop consists of a pressure transducer, diaphragm accumulator, and a diaphragm pump.

The pressure transducer will measure the pressure within the testing chamber and provide information to control the recirculation diaphragm pump to maintain a constant pressure of 50 psi inside the testing chamber. The diaphragm accumulator is part of the system to smooth out any fluctuations in pressure caused by the diaphragm pump. The

diaphragm pump in the recirculation loop is smaller than the pump in the replenishing loop because it does not need to provide as much liquid flow. The pump curve for the recirculation loop diaphragm pump is shown in Figure 24. The design point is highlighted on the pump curve.

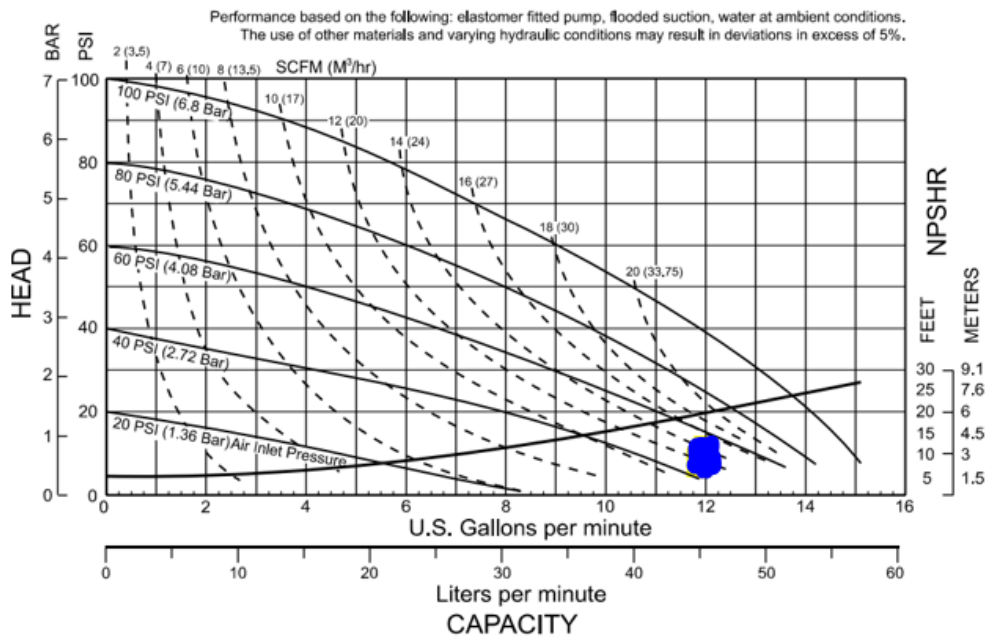


Figure 24: Pump curve for the recirculation loop diaphragm pump [7].

Both of the diaphragm pumps are pneumatic. Compressed air is directed towards the pumps and controlled by two control valves. The large pump has a larger control valve than the smaller pump.

Sand Settling and Fluid Storage Tanks

Once the fluid leaves the testing chamber it is directed towards the sand settling tank. This tank was sized so that the sand would sink at a faster rate than the water level rises.

The sand will sink to the bottom of the tank while the liquid rises and spills into a horizontal pipe connected to the liquid storage tank [6]. This fixed horizontal pipe will ensure that the liquid level remains constant and any change to the mass of the tank will be a function of an increased volume of sand and a decreased volume of liquid. This change in mass is monitored by a scale underneath the sand settling tank. The feedback from this scale will indicate how much sand has been removed from the flow and dictate the amount that should be added to replace it.

The liquid will leave the sand settling tank via a fixed horizontal pipe and enter the fluid storage tank. This tank is part of the design to ensure that there is enough flexibility in liquid volume for the replenishing pump to operate over the required range of flow conditions. Neither of the tanks are open to the atmosphere because the liquid would evaporate. In addition to evaporation concerns, changes in the weather could cause water to condense inside of either tank when oil is used as the working fluid.

The liquid storage tank also rests on a scale so that its volume can be monitored. Changes in mass of the liquid storage tank will be a redundant method to measure the flow rate of the replenishing loop. The location of the two tanks discussed above is shown in Figure 25.

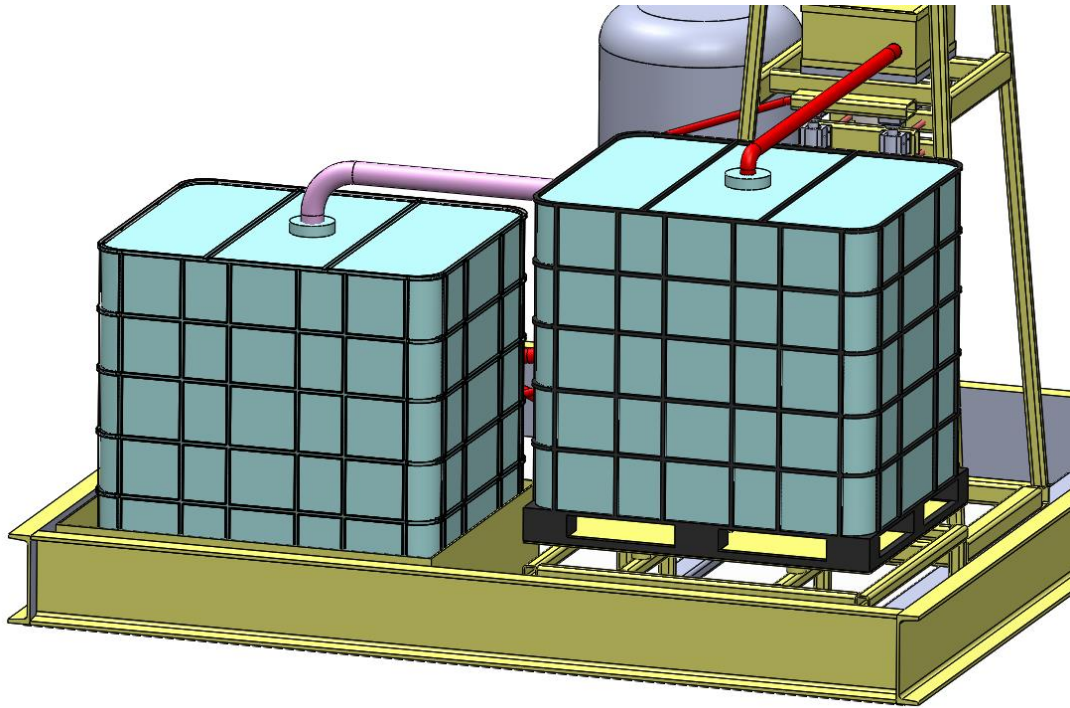


Figure 25: The liquid storage tank (left) and sand settling tank (right).

Sand Administration

Once the used sand is removed from the liquid, fresh sand must be added back to the flow and introduced into the testing chamber. The anticipated flow rate through the bearing annulus provided by CFD simulation indicated how much fresh sand flow will be required. This provided a design constraint for the maximum required sand for the testing apparatus to operate for 12 hours autonomously. Figure 26 shows the design for the sand administration system.

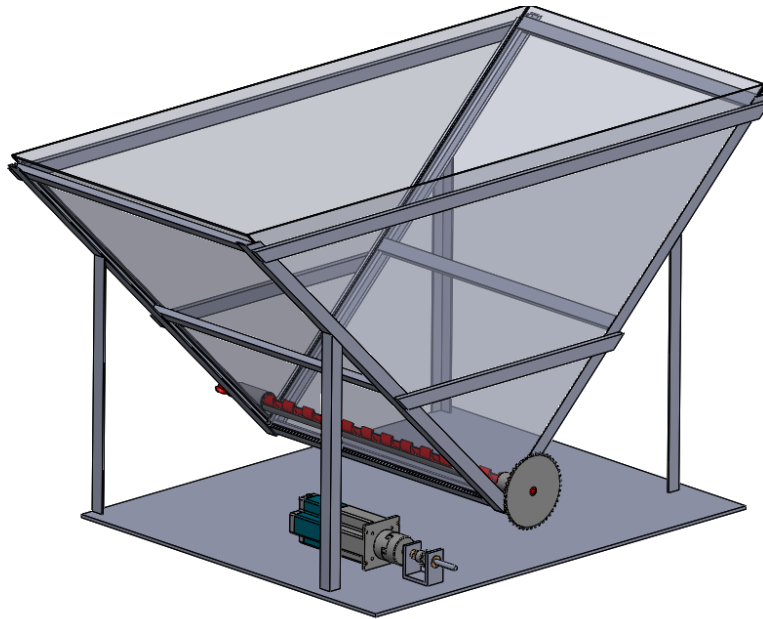


Figure 26: The sand administration system to add sand to the flow.

The sand administration system consists of several main parts that must work together so that sand can be added to the flow. Sand will be added through the top of the sand administrator and rest on an auger screw located at the bottom of a “V” shaped trough. The design includes this trough instead of a converging point so that if any sand gets wet, the entire system will not become clogged. The auger screw turns and advances sand towards the back side of the sand administrator where the sand is dumped into a standing pipe in the replenishing loop. The sand administration system sits on top of a third scale so that the amount of sand that is added to the system can be measured.

The auger screw that advances the sand towards the standing pipe is driven by a geared stepper motor. The stepper motor must be geared so that the required torque to turn the screw can be delivered. A stepper motor was selected for this application so that

the system controls can regulate how many rotations are delivered to the auger screw. The auger screw can be calibrated so that each revolution delivers a known volume of sand to the standing pipe. This calibration will be built into the control system for redundancy in measuring the amount of sand added to the flow.

The stepper motor is connected to the auger screw by making use of a chain and two gears. A small gear attached to a shaft will be coupled to the stepper motor. The shaft must be fixed independently of the stepper motor shaft because the tension loads exerted from the chain exceed the stepper motor shaft capacity. This small gear is chained to a larger gear that turns the auger screw. This configuration is shown in Figure 27.

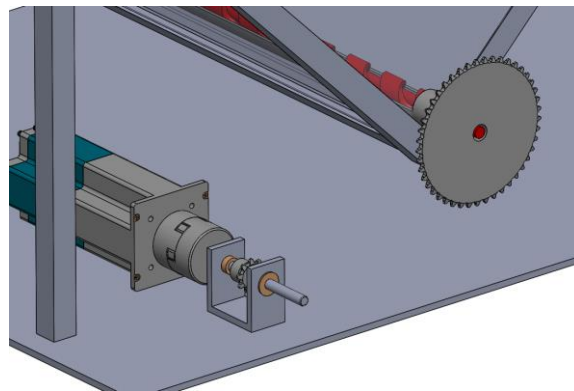


Figure 27: The stepper motor that drives the sand administration system.

Controls

The goal of the control system is to allow the testing apparatus to run autonomously. The reason for this is because each bearing must be tested for 200 hours. It would not be

conducive to time management to operate the apparatus during business hours alone.

The data acquisition and control system were designed to accommodate this task. The instruments that are controlled are shown in Table 3 and the data that will be collected is listed in Table 4.

Table 3: Instruments that need to be controlled.

No	Instrument	Function	Control Value	Control device	Communication
1	Recirculating loop diaphragm pump	Recirculate the flow in the testing chamber	Air pressure to pneumatic pump	Air pressure control valve	4-20 mA current
2	Replenishing loop diaphragm pump	Replenish flow with new sand to the testing chamber	Air pressure to pneumatic pump	Air pressure control valve	4-20 mA current
3	Stepper motor	Supplement sand loss to maintain the sand density in the chamber at 2g/L	Rotation speed and number of turns	Computer	RS 232
4.	VFD	Control the speed of motor	Frequency of motor's power supply	Computer	RS 485

Table 4: The data that needs to be acquired.

No	Instrument	Function	Data Type
1	Proximity probe (2)	Measure the orbit of disk	Voltage
2	Flush Mount Pressure Transducer	Measure the pressure in the bearing annulus	Voltage
3	Pressure Transducer	Measure the pressure in the testing chamber	Voltage
4	Flush Mount Thermocouple	Measure the temperature in the clearance between sleeve and bushing	Voltage
5	RPM Sensor	Measure the rotation speed of the shaft	Voltage
6	Load cell (3)	Measure the load on the journal bearing	Voltage
7	Scale (3)	Measure the mass of liquid storage tank, sand settling tank, and sand administrator.	RS 232
8	Flow meter	Measure the flow rate in the replenishing loop	4-20 mA current

The data acquisition system consists of a National Instrument cRIO-9074 real time controller and five C series modules were selected based on the requirements of the system [8]. The C series modules include:

- NI 9215: Simultaneous voltage input module
- NI 9237: Load cell module
- NI 9205: Voltage input module
- NI 9213: Thermocouple module
- NI 9265: Current output module

The NI 9215 and NI 9237 modules collect data simultaneously. The reason for this is because these modules will be collecting data as a function of the rotation angle of the

shaft. This will allow data to be correlated to the bearing rotation relative to the bushing.

A flow chart of the data acquisition is shown below in Figure 28.

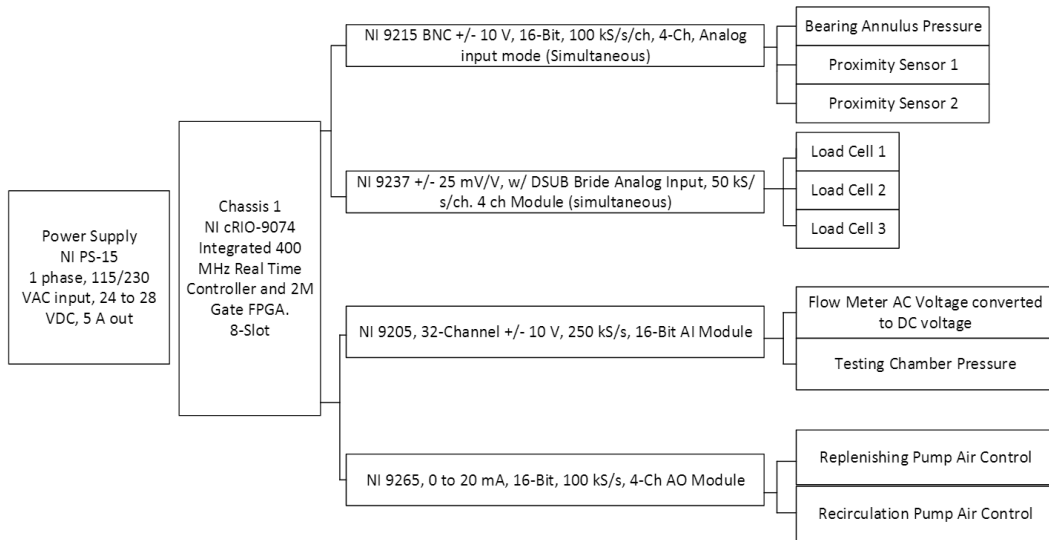


Figure 28: Instrumentation flow chart.

The devices connected to each module were also mapped out in a more detailed flow chart shown below in Figure 29.

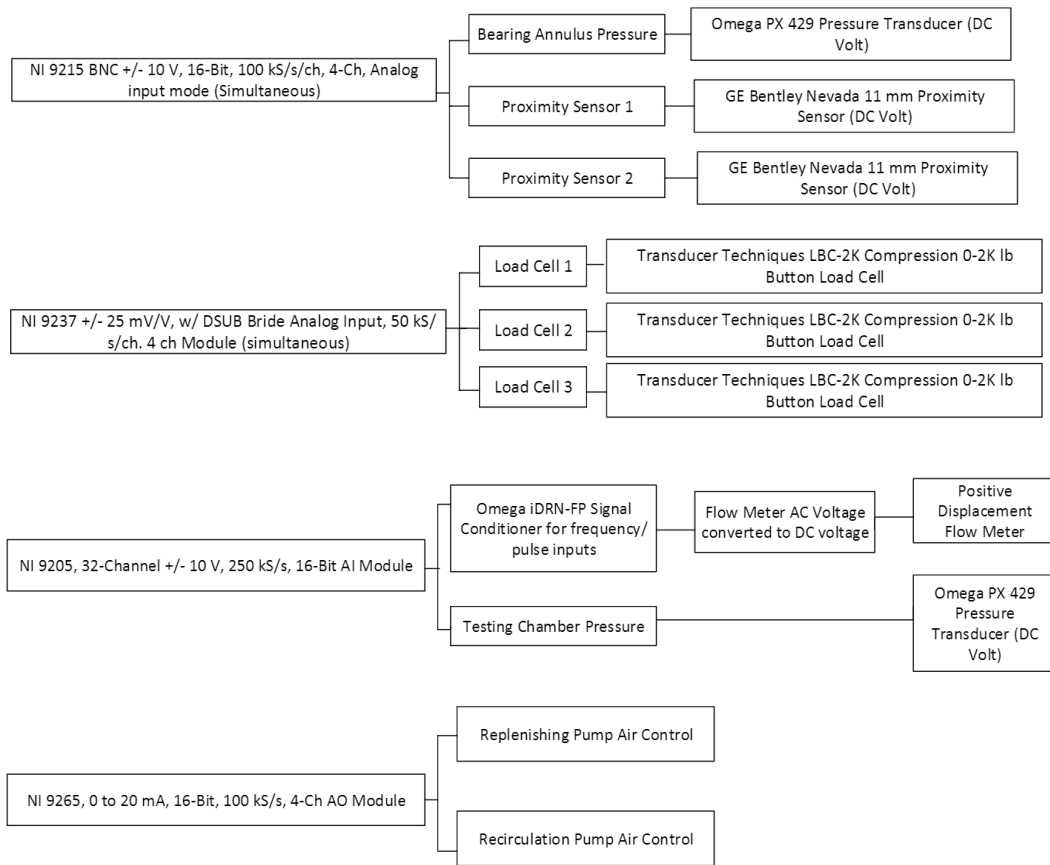


Figure 29: Device selection details.

While operating the bearing testing apparatus, there are four instruments that must be controlled. These instruments are the recirculating loop diaphragm pump, replenishing loop diaphragm pump, stepper motor, and VFD. The control algorithms for these instruments are listed below.

The pulsation of the pressure associated with the diaphragm pumps makes it impossible to design a PID controller to maintain the pressure in each loop. Instead, the

small diaphragm pump was set to always run continuously at the maximum rate it can pump. The large diaphragm pump was set to run so that 50 psi could be maintained across the journal bearing. This was determined by manually operating the large diaphragm pump control valve until a steady pressure of 50 psi was reached.

The stepper motor and VFD come from the manufacturer with an independent control system. Both of their control orders are sent by the serial communication ports in the computer. The difference between the two is that the stepper motor uses RS 232 communication protocol while the VFD uses RS 485 communication protocol. The control signal for the VFD is the speed of motor. And the control signal of stepper motor is calculated based on the sand mass loss during testing. The control diagram of stepper motor and VFD is shown below in Figure 30.

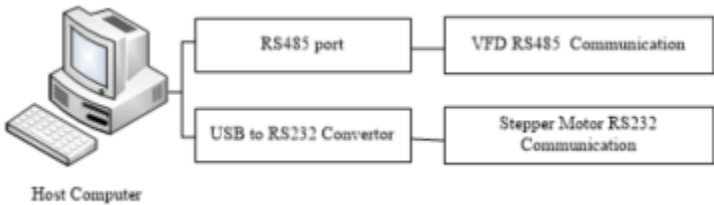


Figure 30: Control diagram of the stepper motor and VFD

FACILITY CONSTRUCTION

The ESP journal bearing testing facility was constructed outside on the southwest side of the Turbomachinery lab at Texas A&M University. The design of the testing facility took approximately 3-4 months and the physical construction took approximately 7 months to complete. Figure 31 shows the facility location before construction was started. The location provided 460 volt electricity that was used to drive the VFD and high speed motor.



Figure 31: Facility location at the turbomachinery lab at Texas A&M University,

An outside location was selected due to space constraints inside the lab. An insulated shed was brought to the site to serve as a graduate student office during construction and testing. The shed was outfitted with electricity, internet, and a heat

pump to heat and provide air conditioning to the equipment and occupants inside.

Figure 32 shows a picture of the shed before any equipment was moved inside.



Figure 32: The insulated shed that serves as the facility office.

Part of the design of the ESP journal bearing testing facility is the ability to run water and oil through the system. When using water, it is acceptable to spill some on the ground and have it run off into the woods. When using oil, this is not the case and a large tray had to be built to contain leakage in the event of a catastrophic leak. This tray was made of 12 inch Channel steel for the walls and ¼ inch steel for the floor. The tray was welded together then caulked with a metal sealant at the seams to prevent leakage. Figure 33 shows the testing tray after it was welded together. It was later caulked and painted to prevent leakage and corrosion.



Figure 33: The testing tray that was constructed to contain liquid leakage.

Most of the steel pieces that were used in construction were welded together and painted by graduate students. The testing chamber, imitation bearings, and shaft required precise machining and were outsourced to a machine shop. Most of the labor of putting together the testing facility was done by graduate students. This included moving all of the different components into the testing tray and securing them as well as constructing a roof over the top of the testing tray to keep rain out.

The control system that was designed and used for the facility were purchased primarily from National Instruments. The hardware was put together on a rack as shown in Figure 34. The software that is used to control the hardware was written in LabView. This software not only controlled every part of the testing facility, it also served as the data acquisition system.

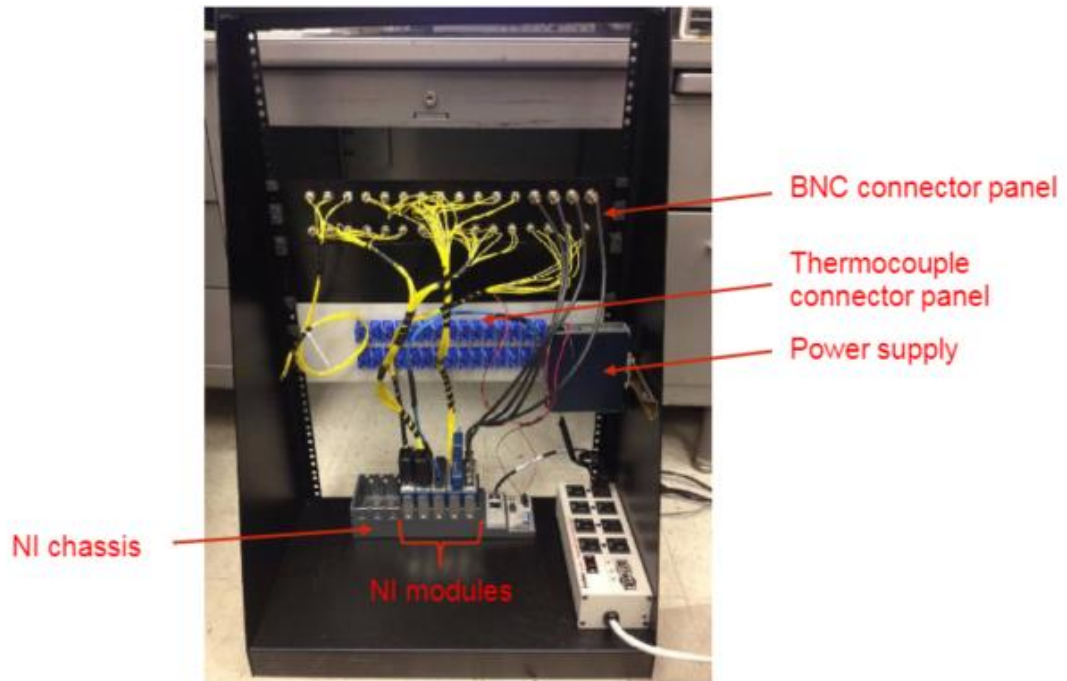


Figure 34: Control hardware installed on a rack (backside view)

The actual testing facility is shown below in Figure 35.



Figure 35: Complete assembly

The drawings for all of the different pieces associated with the testing facility construction are shown in Appendix A. Throughout testing, several issues arose and recommendations for resolving these issues are listed further down in conclusions section of this thesis.

FACILITY VALIDATION

The testing facility was validated by testing three different brass bearings that represent three different radial clearances within the spectrum of clearances found during the erosion study. The ID of the bushing was held constant while the OD of the bearings was changed. The three different radial clearances that were tested were 6, 12.5 and 25 mil radial clearance.

The first test was conducted with the 6 mil radial clearance, the second with the 12.5 mil radial clearance, and the third with the 25 mil radial clearance. The testing facility was sufficiently built to maintain a 50 psi differential pressure across the bearing for the first two tests. This was because the large diaphragm pump (replenishing loop) was not operating continuously. The annular clearance of the bearing was small enough that the leakage through the bearing only required the large diaphragm pump to push more liquid into the system every ten seconds or so. The small diaphragm pump (recirculation loop) operated continuously and there were small fluctuations (plus or minus 4 psi) in the testing chamber pressure from the pulsation of the small diaphragm pump.

When the 25 mil radial clearance brass bearing was tested, the leakage rate through the annulus increased drastically and required the large diaphragm pump to operate continuously. The large pump operating continuously caused large swings (plus or minus 20 psi) in the testing chamber pressure. This led to poor data collection that had a constantly changing testing chamber pressure. For this reason, only the data for the 6 and 12.5 mil radial clearance is presented below. Suggestions for improvement of this problem are included in the summary and conclusions section of this thesis.

Table 5 shows the operating data from the 6 mil radial clearance brass bearing test for 6 different operating speeds between 600 RPM and 3600 RPM. The tabulated data shows the orbit radius, maximum pressure, minimum pressure, and maximum radial load experienced within the bearing at six different operating speeds. The pressure values that are shown are given in absolute pressure. The reason for this is so that the annulus pressure can be compared to the vapor pressure of water to see if cavitation occurs. Figure 36 shows a comparison between the orbit sizes of the shaft just above the imbalance disk as a function of rotating speed. It can be seen from Table 5 and Figure 36 that the orbit of the shaft above the imbalance disk exceeds the size of the bearing clearance. This indicates that the shaft is bowing as a result of the disk imbalance and the bottom of the shaft is being constrained by the bearing making contact with the bushing.

Table 5: Operating data from the 6 mil radial clearance brass bearing test.

Operating Speed (RPM)	Orbit Radius (mils)	Maximum Pressure (psia)	Minimum Pressure (psia)	Maximum Force (lb_f)
600	3.32	18.32	14.36	2.60
1200	5.14	29.16	12.77	3.55
1800	7.29	36.05	11.75	3.52
2400	8.42	27.92	10.66	5.91
3000	9.74	40.22	6.99	10.77
3600	10.56	55.21	4.46	18.68

Table 5 also includes the maximum and minimum pressure seen in the bearing annulus during operation at each of the six operating speeds. As the operating speed increased, and the orbit radius also increased, the maximum pressure showed an

increasing trend. The minimum pressure showed a decreasing trend. These trends are shown as a function of rotation angle in Figure 37. It is also shown in Figure 37 that the pressure annulus pressure is cyclical as a function of rotation angle. The maximum and minimum pressures repeat once every rotation. This agrees with the Sommerfeld lubrication theory in that as the bearing rotates inside the bushing, the eccentricity of the bearing produces an area of high pressure and an area of low pressure resulting from the converging/diverging wedge formed from shaft not remaining completely concentric within the bushing. It is important to note that the pressure comparison shown in Figure 37 is only for comparison of the magnitude of the pressure at different operating speeds. The pressure distributions were superimposed on top of each other for a clear comparison by aligning the peaks. The peaks do not necessarily occur at the same angle for each operating speed.

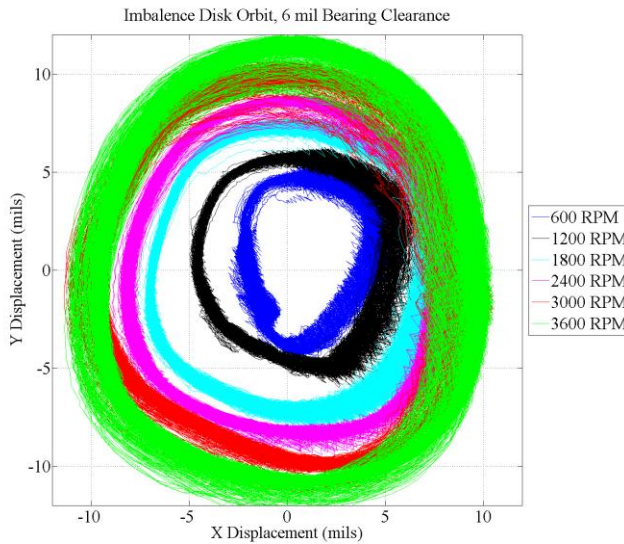


Figure 36: Orbit measurements of the 6 mil bearing at different speeds

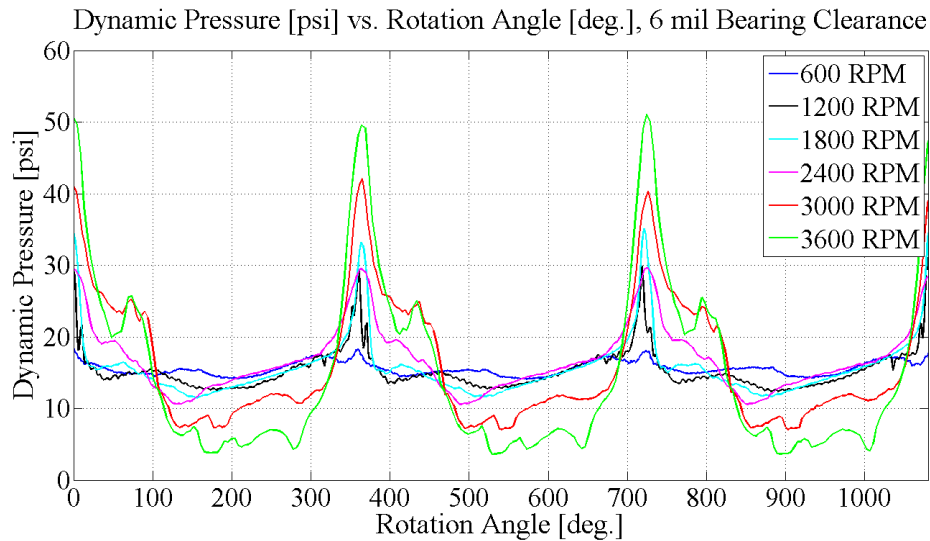


Figure 37: Pressure distribution as a function of angle for the 6 mil bearing.

The three load cells surrounding the journal bearing are situated on the same plane as the dynamic pressure transducer and located 120 degrees from each other. The load measurements data were processed so that the load measurements oscillated about a no load condition. It can be seen in Figure 38 that the load cell measurements are each 120 degrees out of phase from each other. Each of the curves shown in the figure have a maximum and a minimum every 360 degrees. This makes sense because the high spot of the rotor (also the heavy spot) passes each load cell once every revolution. This heavy spot passes each of the load cells every third of a revolution as indicated by Figure 38.

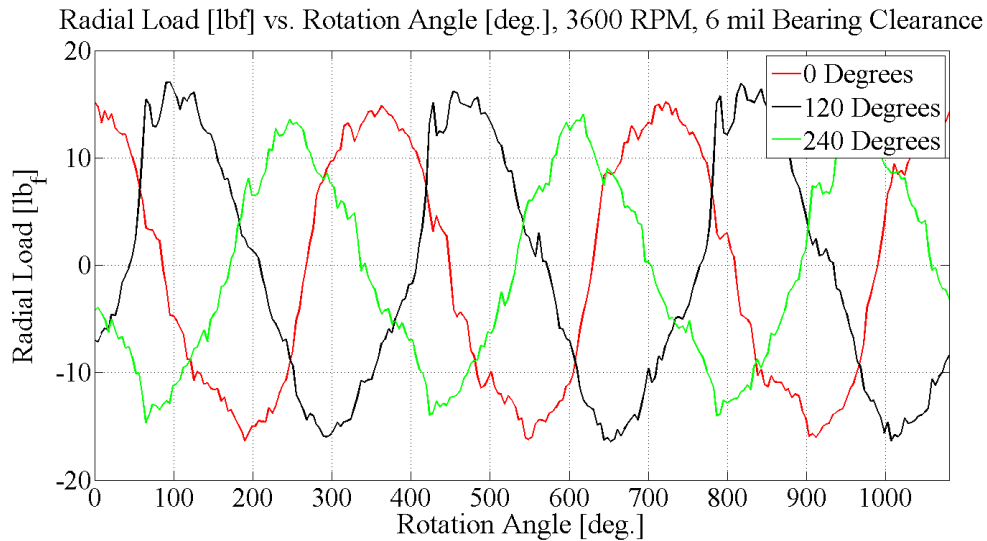


Figure 38: Radial load as a function of angle for each of the load cells.

The measured pressure distribution in the bearing annulus was superimposed with the orbit of the shaft (location) and the force from the point of view of the pressure distribution as a function of rotation angle. These data were all plotted on the same graph to see the relationship between maximum pressure, maximum force, and location. This is shown in Figure 39 for the 6 mil radial clearance bearing operating at 3600 RPM. From the figure, it can be seen that the maximum pressure in the bearing annulus and the maximum radial force experienced from the point of view of the dynamic pressure transducer occur at approximately the same angle. This makes sense because the maximum pressure acting over the bearing area is what causes the maximum force.

Figure 39 shows that the maximum pressure and the maximum force lead the minimum position by a measureable angle. These measurements were found by changing the reference coordinate frame to that of the dynamic pressure transducer. This means that the rotation is a function of time as the bearing passes the dynamic

pressure transducer. The maximum pressure and the maximum force occur before the minimum clearance passes the point of the pressure transducer. What this means is that the area of high pressure is occurring before the minimum clearance in the journal bearing. This contradicts the Sommerfeld journal bearing theory where a converging flow wedge causes a region of high pressure behind the minimum clearance. This can be explained by the onset of shaft whirl. An imbalance (as in the imbalance disk) typically causes the shaft to whirl in the direction of the spin. When the shaft whirls, it squeezes the liquid film in front of point of minimum clearance. Table 6 shows that as the rotation speed increases, the angle at which the area of high pressure leads the minimum clearance decreases for the 6 mil bearing.

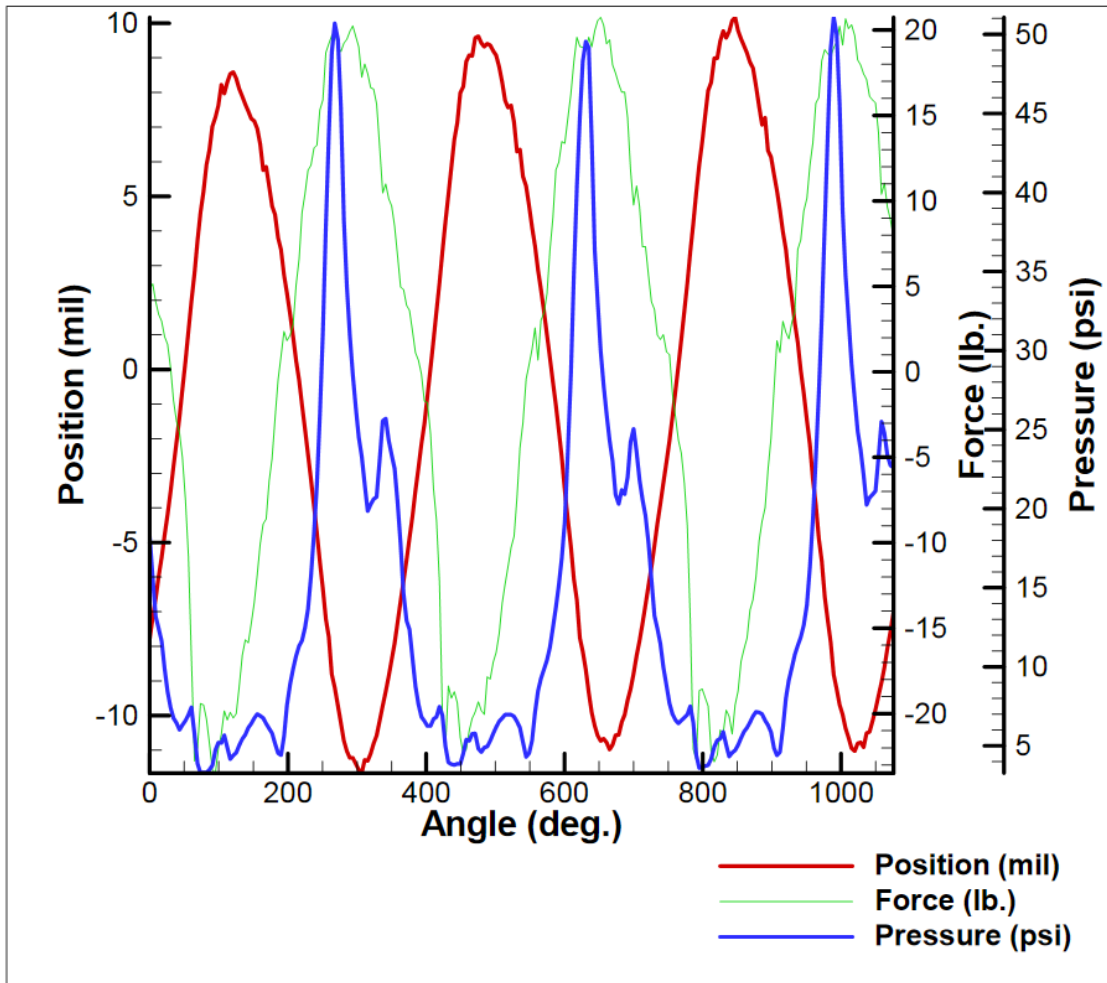


Figure 39: Position, force, and pressure for 6 mil bearing at 3600 RPM

The pressure distribution for each of the operating speeds was superimposed with the position data of the shaft. This was done to determine if the peak of the pressure distribution occurred at the same angle for each operating speeds. Figure 40 shows that the angle location of the peak pressure depends on the operating speed. As the operating speed increases, the lead angle of the maximum pressure in front of the minimum clearance decreases. This is quantified in Table 6 for the operating speeds between 1200

and 3600 RPM. The 600 RPM data was omitted because of the large amount of noise in the data.

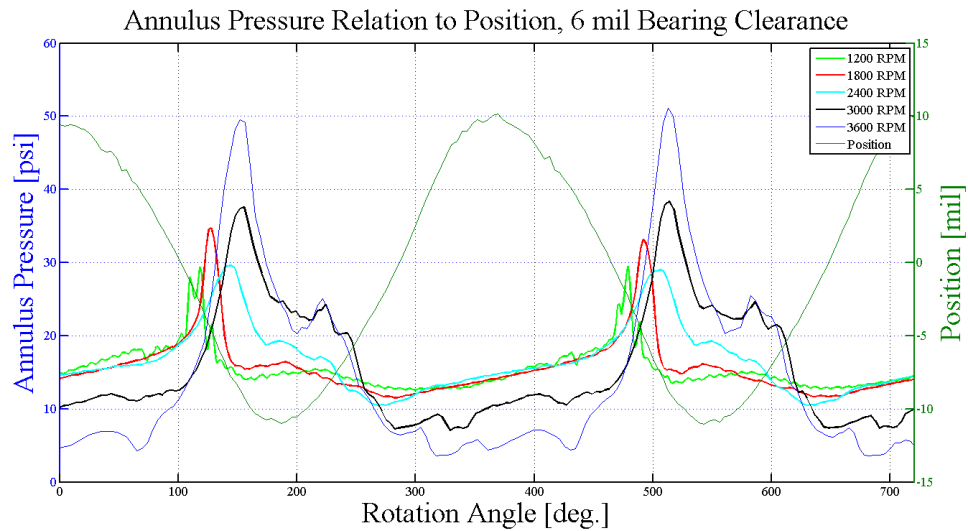


Figure 40: Relationship between position and pressure for the 6 mil bearing.

Table 6: 6 mil bearing lead angle between pressure and minimum clearance.

Speed (RPM)	Pressure Lead Angle (deg.)
1200	68.6
1800	57.45
2400	43.4
3000	32.55
3600	34.8

The proximity data that was collected from the orbit of the shaft just above the imbalance disk was used in conjunction with the Sommerfeld theory to predict the pressure distribution within the bearing annulus. This was also done to determine if the Sommerfeld theory prediction matched the measured data. An eccentricity ratio for each

operating speed was found by dividing the orbit radius by the bearing radial clearance. The Sommerfeld theory was invoked to determine a predicted pressure distribution for each eccentricity ratio. For each operating speed, the determined eccentricity ratio was multiplied by a proportionality constant so that the predicted pressure distribution matched the measured pressure distribution. The proportionality constant was determined by matching the measured and predicted maximum pressure. This was necessary because the actual orbit of the bearing is impossible to know because there is no way to put proximity probes inside the bearing. The trend that was found was that at lower rotational speeds, the proportionality constant was above unity and as the speed increased, the proportionality constant decreased. This makes sense because at low operating speeds, the imbalance disk orbit is smaller than the bearing clearance and indicates that the imbalance disk is not causing the shaft to deflect at all. It also means that the orbit of the bearing is larger than that of the imbalance disk. As the orbit of the imbalance disk increased past the size of the bearing clearance, the end of the shaft was constrained by the bushing ID and it indicates that the shaft deflected in a bow shape. The proportionality constants for the 6 mil radial clearance bearing with the corresponding operating speed is shown in Table 7. In addition, the measured and predicted pressure distribution for each operating speed is shown in Figure 41 and Figure 42 for two selected operating speeds.

Table 7: The proportionality constants for each speed for the 6 mil bearing.

Operating Speed (RPM)	Proportionality Constant Range
600	1.52-1.55
1200	1.06-1.08
1800	0.74-0.76
2400	0.61-0.62
3000	0.54-0.55
3600	0.51-0.52

1200 RPM, 6 mil Bearing Clearance Annulus Pressure Compared to Sommerfeld Prediction

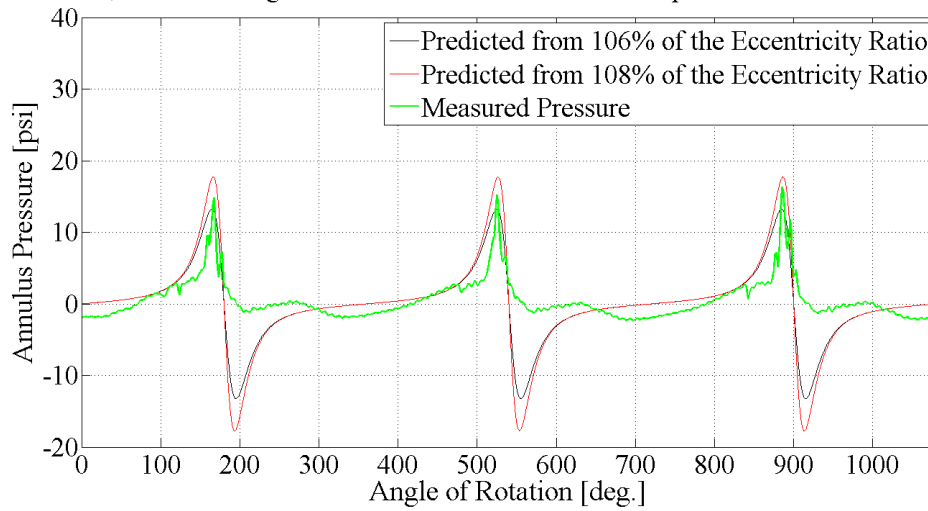


Figure 41: Prediction and measured pressure for the 6 mil bearing at 1200 RPM

3600 RPM, 6 mil Bearing Clearance Annulus Pressure Compared to Sommerfeld Prediction

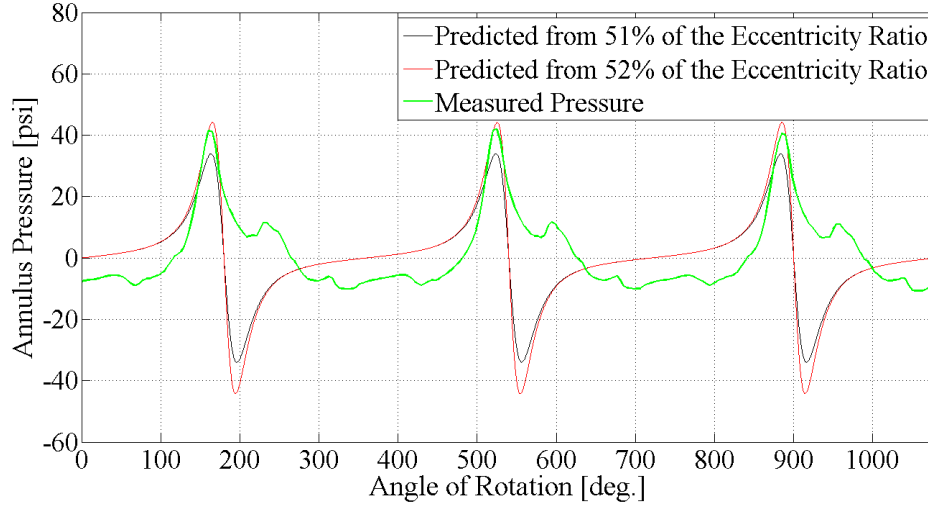


Figure 42: Prediction and measured pressure for the 6 mil bearing at 3600 RPM

The Sommerfeld theory was invoked to match the measured pressure distribution to a predicted pressure distribution. Once the Sommerfeld theory was superimposed with the measured pressure distribution, it is seen that the maximum pressures match. In addition the decrease from the highest pressure to the lowest pressure for the Sommerfeld theory occurs over a smaller range of rotation angle than the measured pressure. It is also seen that the measured pressure only follows the Sommerfeld pressure distribution for the first half of the bearing rotation (high pressure side). This indicates that the measured data follows more of a half-Sommerfeld distribution where the rotation of the journal does not create an area of low pressure that sucks lubricant into the bearing annulus. This could be attributed to the fact that there was a negative pressure gradient across the bearing (50 psi) that forced the fluid to be pushed instead of pulled into the bearing clearance. As the rotation speed increases, the area of low pressure begins to become apparent, however its magnitude is minimal compared to that

of the high pressure area. This can be attributed to the fact that the eccentricity ratio inside the journal bearing increases with increasing rotation speed.

The same analysis was repeated for the bearing with a 12.5 mil radial clearance. For brevity, only several plots are shown in this section of the report. All data for the 6 mil and 12.5 mil radial clearance are shown in Appendix B and Appendix C, respectively. The operating data shown in Table 8 is from the tests conducted on the 12.5 mil radial clearance bearing. The tests show the same trends that were observed with the 6 mil clearance. The maximum pressure and maximum force for the 12.5 mil bearing are higher and the minimum pressure is lower. The lowest pressure that was measured in the bearing clearance occurred at 3600 RPM. This pressure is above the vapor pressure of water at 90 degrees (0.698 psia) indicating that cavitation does not occur in the bearing annulus.

Table 8 Operating data from the 12.5 mil radial clearance brass bearing test.

Operating Speed (RPM)	Orbit Radius (mils)	Maximum Pressure (psia)	Minimum Pressure (psia)	Maximum Force (lb_f)
600	2.21	15.92	12.30	13.93
1200	3.51	17.71	11.52	25.27
1800	5.15	19.67	11.31	32.04
2400	7.94	24.65	7.26	42.62
3000	8.87	32.95	6.66	50.23
3600	8.06	29.22	1.10	108.59

The orbit comparison for the 6 different operating speeds is shown in Figure 43. It can be seen that as the operating speed increases, as does the orbit until a certain point.

It appears the orbit of the shaft just above the imbalance disk does not exceed the nominal bearing radial clearance.

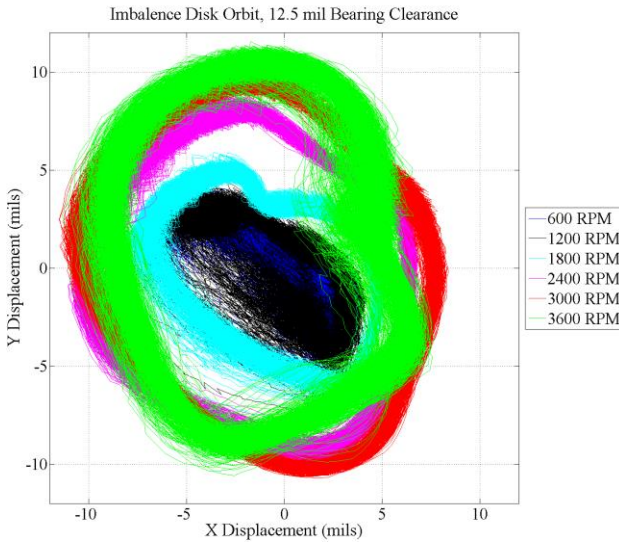


Figure 43: Orbits of the 12.5 mil bearing at different speeds

Figure 44 shows a comparison of the different dynamic pressure measurement inside the bearing annulus at each speed as a function of rotation angle. It shows that at the first two speeds, the pressure remains relatively constant. As the operating speed increases, the general trend is that the minimum pressure decreases and the maximum pressure increases. This information, combined with the orbit data shows that there is always a liquid film between the bearing and the bushing.

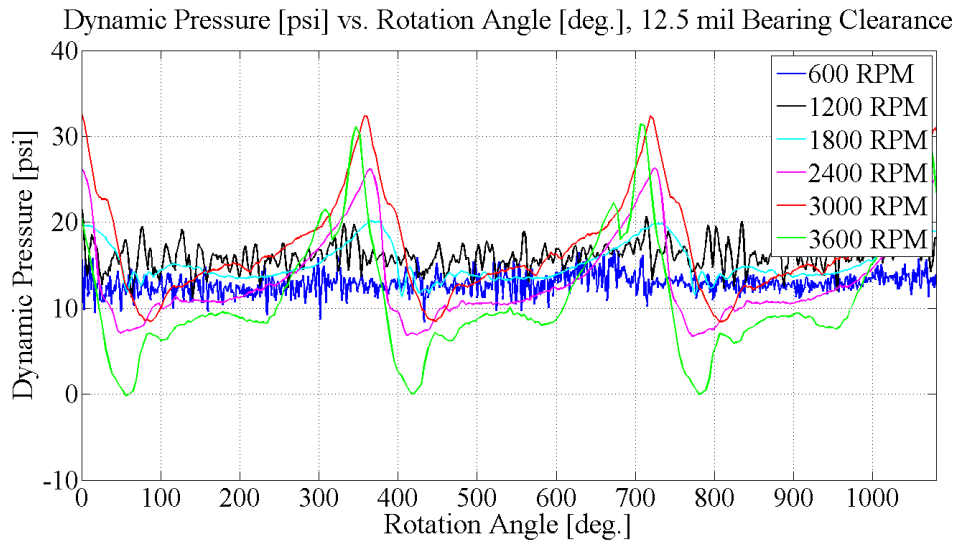


Figure 44: Pressure as a function of angle for the 12.5 mil bearing.

It is shown in Figure 45 that the load cell measurements are each 120 degrees out of phase from each other. The shape of this plot looks similar to that of the 6 mil radial clearance force data. The difference is the magnitude of the force. As the bearing clearance increased, the maximum force also increased for the same operating speed.

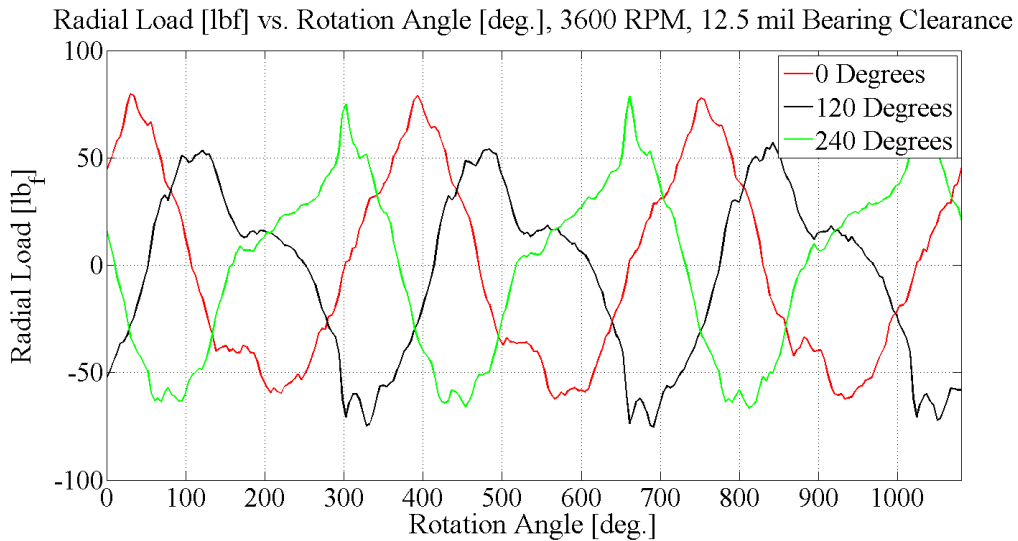


Figure 45: Radial load as a function of angle for each of the load cells.

As in the 6 mil bearing case, the location, force, and pressure measurements were compared as a function of rotation angle from the point of view of the pressure transducer. Figure 46 shows this data for the 12.5 mil bearing operating at 3000 RPM. The pressure and force are in phase and they are both out of phase with the position of the shaft.

Just as in the case with the 6 mil bearing, the pressure distribution for each speed was superimposed with the position of the journal bearing. This is shown in Figure 47 and the lead angles are tabulated in Table 10. This is only shown for operating speeds between 1800 and 3600 RPM due to an abundance of signal noise at lower speeds. As with the 6 mil bearing, the angle location of the peak pressure depends on the operating speed, however for the 12.5 mil bearing, as the operating speed increases, the lead angle increases. This can be explained by a comparison between the approximate eccentricity ratios that were found from the proportionality constants. Generally speaking, the 12.5

mil bearing eccentricity ratios are larger than the 6 mil eccentricity ratios at a given speed. This comparison is shown below in Table 9

Table 9: Comparison between the bearing's estimated eccentricity ratios

Operating Speed (RPM)	Eccentricity Ratio	
	6 mil	12.5 mil
1800	0.90-0.92	0.91-0.92
2400	0.86-0.87	0.93-0.94
3000	0.88-0.89	0.95-0.96
3600	0.90-0.92	0.91-0.94

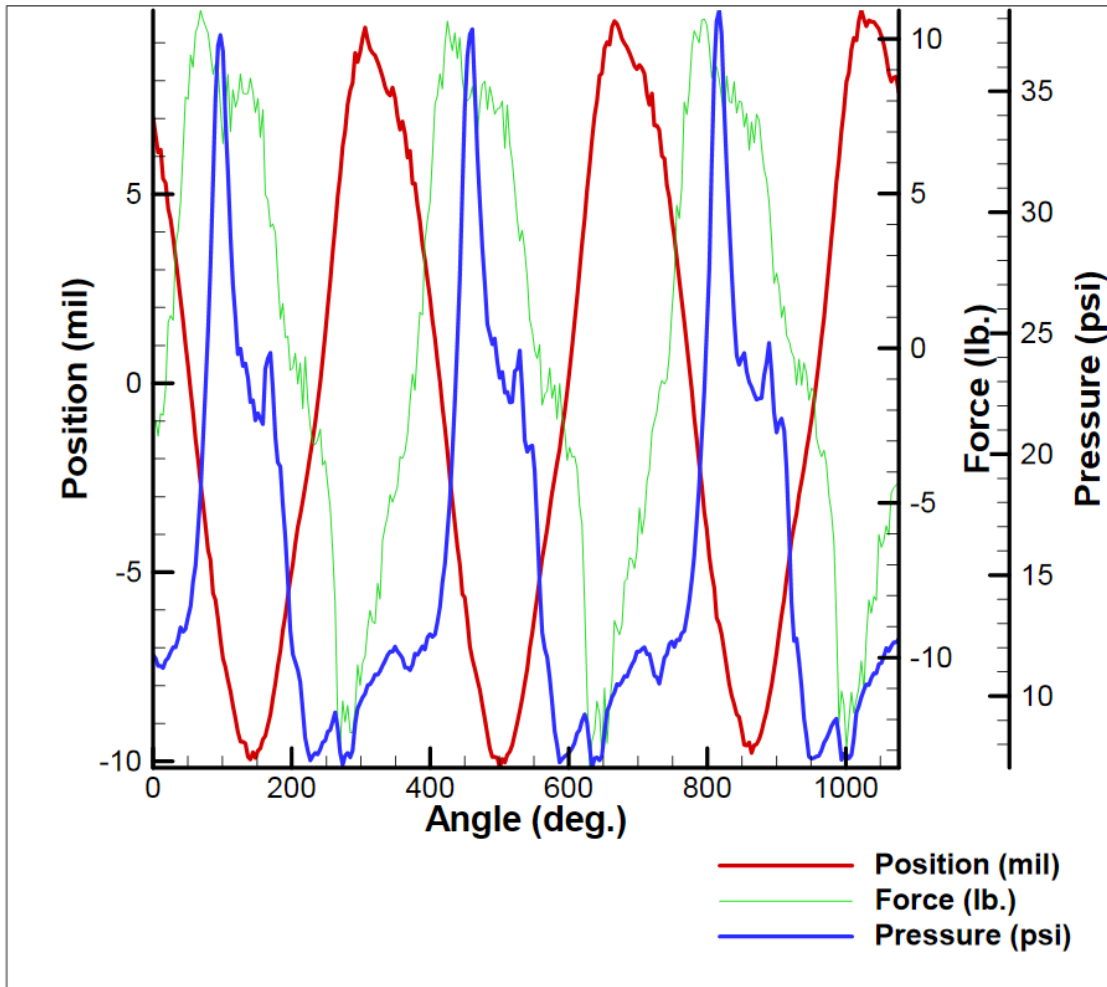


Figure 46: Position, force, and pressure for 12.5 mil bearing at 3600 RPM

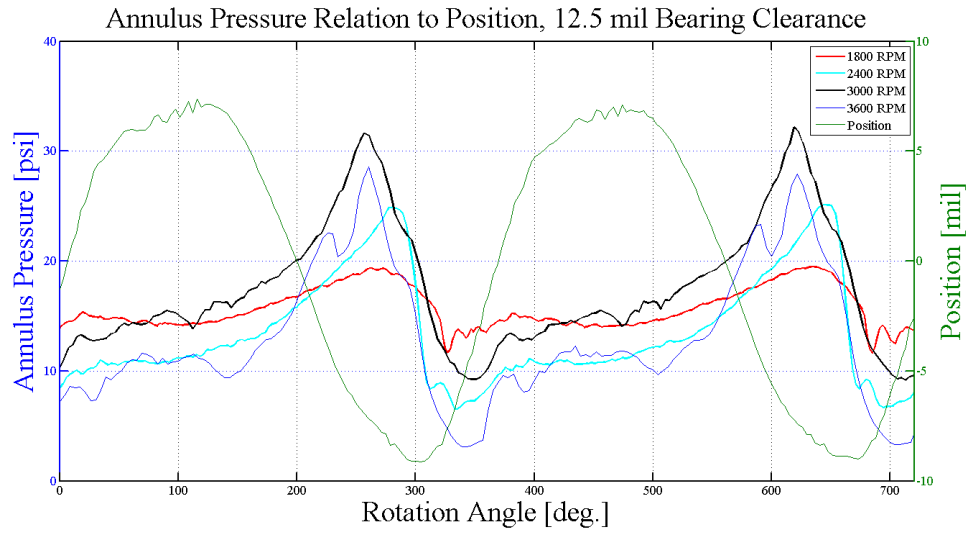


Figure 47: Relationship between position and pressure for the 12.5 mil bearing.

Table 10: 12.5 mil bearing lead angle between pressure and minimum clearance.

Speed (RPM)	Pressure Lead Angle (deg.)
1800	30.6
2400	16.25
3000	40.05
3600	43.4

The same Sommerfeld pressure distribution comparison was made to the 12.5 mil radial clearance bearing data. Table 11 shows the proportionality constant range required to match the measured data to the theoretical prediction. The comparison between the prediction and measured data for 1800 RPM and 3000 RPM is shown in Figure 48 and Figure 49, respectively.

Table 11: The proportionality constants for each speed for the 12.5 mil bearing.

Operating Speed (RPM)	Proportionality Constant Range
600	2.40-2.45
1200	1.25-1.59
1800	1.06-1.07
2400	0.70-0.71
3000	0.64-0.65
3600	0.68-0.70

1800 RPM, 12.5 mil Bearing Clearance Annulus Pressure Compared to Sommerfeld Prediction

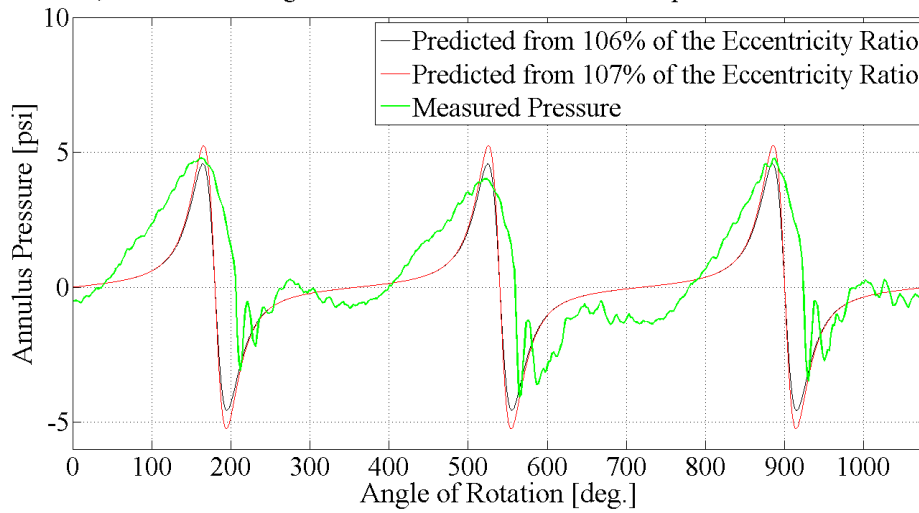


Figure 48: Prediction and measured pressure for the 12.5 mil bearing at 1800 RPM

3000 RPM, 12.5 mil Bearing Clearance Annulus Pressure Compared to Sommerfeld Prediction

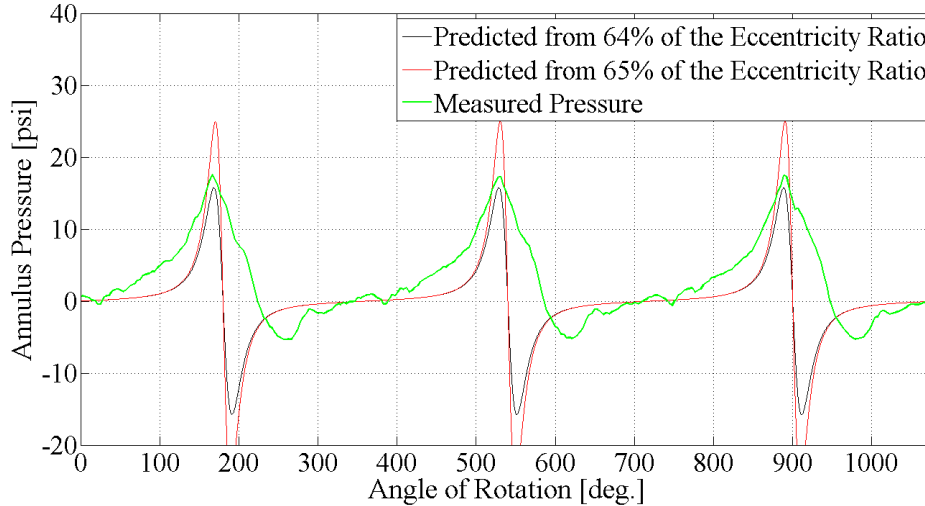


Figure 49: Prediction and measured pressure for the 12.5 mil bearing at 3000 RPM

The Sommerfeld comparison to the 6 mil bearing was similar to that of the comparison to the 12.5 mil bearing. The measured pressures only follow the Sommerfeld pressure distribution for the first half of the bearing rotation (high pressure side). A half Sommerfeld pressure distribution is apparent from the measured data. As the rotation speed increases, the area of low pressure, or the sucking of lubricant begins to become apparent. The magnitude of this low pressure is much smaller than that of the high pressure area. This can be attributed to the fact that the eccentricity ratio inside the journal bearing increases with increasing rotation speed.

The motivation for the construction of this facility was to be able to imitate the motion of the impeller found in the WJE-1000 pump. From previous experiments, the impeller that the imbalance disk was selected to imitate was the second impeller. The set screws on the imbalance disk were adjusted so that the orbit of the imbalance disk

matched the orbit of the second impeller found of the WJE-1000 pump. A comparison between the disk orbit and the second impeller is shown below in Figure 50.

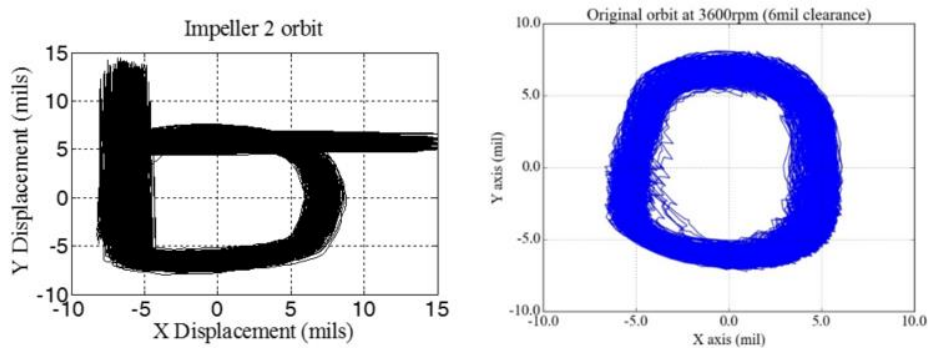


Figure 50:Orbit Comparison to WJE-1000 Pump at 6 mil bearing, 3600 RPM

The XLTRC2 simulation suggested that there was no rotor critical speeds at 3600 RPM (60 Hz). This information was used to determine if any other critical speeds were present in the range of operating speeds. The shaft was set to spin at 3600 RPM before any testing took place for each bearing clearance. Once the shaft was spinning at 3600 RPM, a rundown test was conducted. This test was conducted by turning the motor off and recording the motion of the shaft with two proximity probes as it slowed down to a complete stop. A Fast Fourier Transform (FFT) was conducted on the proximity data to determine if there was a frequency at which the shaft became excited-indicating a critical speed. During the rundown tests, no critical speed became apparent after conducting the rundown tests. This determined that it was safe to operate the shaft and imbalance disk in the anticipated operating speed ranges.

The proximity data from each operating speeds was processed in a similar way to determine if there were any sub-synchronous frequencies present during testing. The reason for this is because there was a 2/3 sub-synchronous frequency found during the WJE-1000 erosion experiment. A FFT was conducted on the proximity data for each operating speed for both the 6 mil and 12.5 mil bearing clearance. From this, a waterfall plot was created for each bearing clearance showing the frequency spectrum for each operating speeds. This is shown in Figure 51 and Figure 52, respectively. No subharmonics were observed in the testing that was conducted. The only frequencies that were observed after the FFT was conducted were multiples of the frequency of the shaft rotation. This can be expressed as $n * f_{rotation}$ where $n = 1, 2, 3 \dots etc.$ In all cases, the amplitude of the harmonics decreased with increasing values of n.

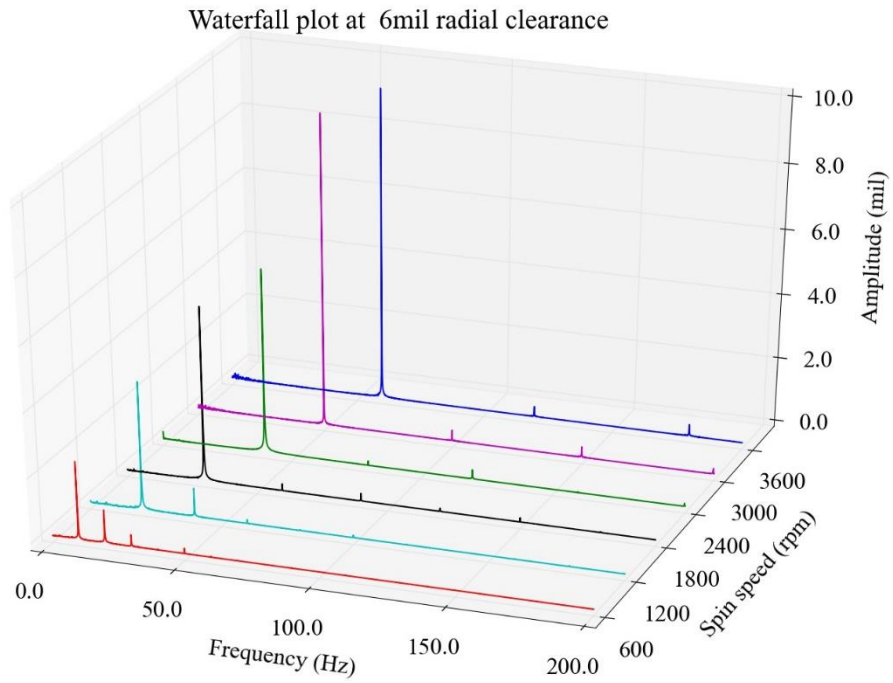


Figure 51: Waterfall plot of the frequency spectrum for the 6 mil bearing.

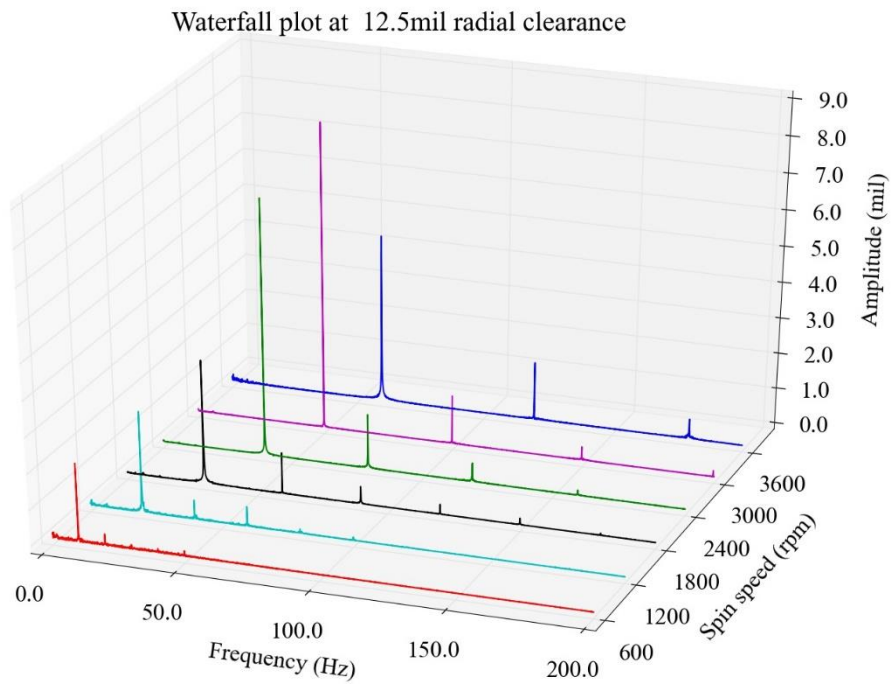


Figure 52: Waterfall plot of the frequency spectrum for the 12.5 mil bearing.

One of the most important features of the testing facility is the ability to inspect the journal bearing at discrete time intervals. When an erosion study is conducted on an entire pump, the pump must be completely disassembled to measure and inspect the bearings. This process takes several weeks and causes the entire erosion study to take up to six months. The testing chamber surrounding the bearing takes about an hour to be lowered to inspect the bearing. Once the bearing and bushing are photographed and measured, it takes about an hour and a half to bring the testing chamber back into position to continue the test. Figure 53 shows the testing chamber once it is lowered on the linear bearings. Once it is in this position, telescoping gages are used to measure the ID of the bushing and a micrometer is used to measure the OD of the journal bearing. In addition, the ID of the bushing can be photographed at a zoom magnitude of about 30 X using a borescope. This is the required magnitude to see the surface hairline fractures found on the bearings from past experiments. The borescope setup is shown in Figure 54. The borescope inside the bushing is shown in Figure 55.



Figure 53: The testing chamber lowered to inspect the journal bearing



Figure 54: The borescope setup to take photographs of the bushing surface



Figure 55: The borescope taking a picture of the bushing surface ID

Figure 56 shows a sample picture that was taken of the ID of the bushing (stainless steel). This picture shows some wear marks, however there are no hairline fractures. This is expected because the test was only run for several minutes and no sand was in the

flow. The main purpose of showing this picture is to prove that it is possible to take high fidelity pictures with the borescope by lowering the testing chamber. A picture of the OD surface of the 12.5 mil brass bearing is shown in Figure 57. This photograph was taken under a microscope. The bearing was simply removed from the shaft and photographed and then put back on the shaft. Both of these figures shown clear tangential wear marks, but as expected, no axial hairline fractures.

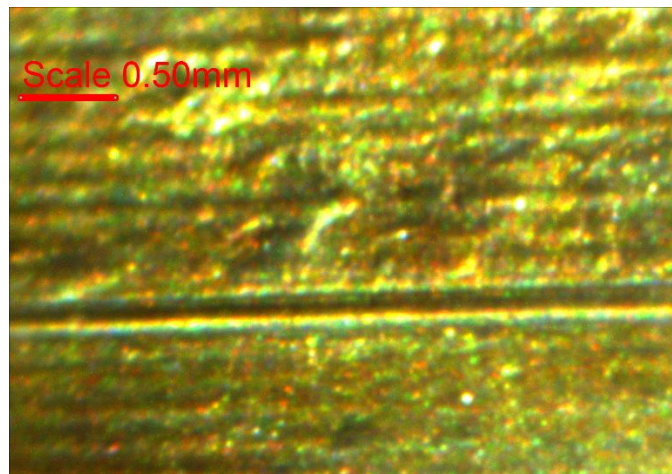


Figure 56: A photograph of the bushing ID taken with the borescope.

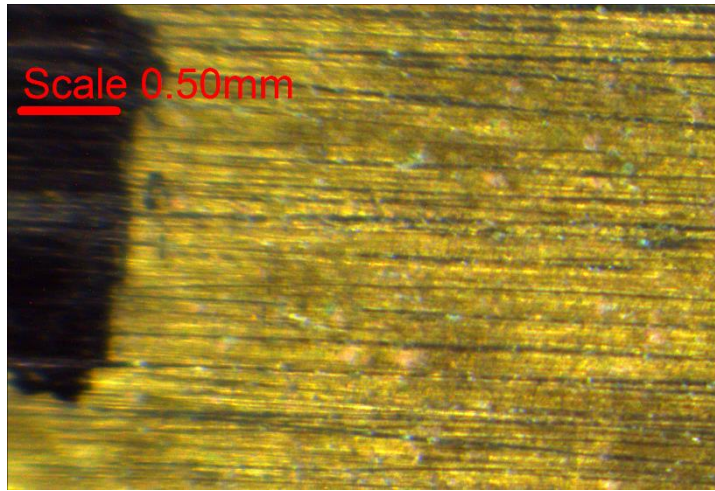


Figure 57: A photograph of the 12.5 mil brass bearing OD surface

Another advantage of exposing the bearing and bushing surface is the ability to measure the roughness of these surfaces. After each bearing was tested, the surface roughness was measured with a portable surface roughness tester. The surface roughness was measured at the top, middle, and bottom of the bearing every 90 degrees around its circumference. For the purpose of this work, the actual values of surface roughness are not important, however the ability to measure the surface roughness is.

CONCLUSIONS AND RECOMMENDATIONS

Conclusions

A testing facility was designed and constructed for erosion testing of an ESP journal bearing independent of the entire pump. This facility has the capability of testing journal bearings at operating speeds ranging from 0 to 7200 RPM. The working fluid for the bearings can either be water or oil with an induced gas volume fraction up to 100% along with a pre-determined amount of sand per unit of volume of liquid. Measurements from a previous erosion study provided orbital motion of an impeller within the ESP. A disk was designed to be fixed to the shaft that replicated these motions. The design allows for measurement of radial load on the bearing as well as pressure and temperature in the bearing annulus. In addition, the orbit of the shaft can be measured.

Two different sizes of bearings were tested-one with a radial clearance of 6 mil and the other with a radial clearance of 12.5 mil. Each of these bearings were tested at 6 different operating speeds ranging from 600 RPM to 3600 RPM. As the operating speed and the bearing clearance increased, maximum pressure measured in the bearing annulus increased and the minimum pressure measured in the bearing annulus decreased. The radial forces also increased as the rotation speed increased and the bearing clearance increased. For the 6 mil bearing, the maximum orbit increased as the rotation speed increased. This trend was also found for the 12.5 mil bearing, however the maximum orbit for the 6 mil bearing was found to be higher than the 12.5 mil bearing. The orbits were measured from a point that was just above the imbalance disk. An explanation for

this is that the 6 mil clearance limited the orbit at the point of the bearing and the shaft deflected more in the 6 mil case than the 12.5 mil case.

The Sommerfeld theory was used to predict pressure in the bearing annulus. The maximum pressure as predicted by the Sommerfeld theory was matched to the maximum measured pressure by multiplying a proportionality constant with the eccentricity ratio measured from the disk orbit. This matched the maximum pressure, but not the entire Sommerfeld distribution. It was found that the area of high pressure lead the location of the minimum bearing clearance. This lead angle decreased as rotation speed increased for the 6 mil bearing and the angle increased as rotation speed increased for the 12.5 mil bearing. This contradicts the converging flow high pressure wedge following the location of minimum clearance as specified by the Sommerfeld theory. The pressure distribution showed an area of high pressure that matched the Sommerfeld theory, however the area of low pressure was not as apparent. This suggest a half Sommerfeld pressure distribution. As the operating speed increased, the area of low pressure became more apparent.

Recommendations and Future Work

The ESP bearing testing facility was validated for two different sized bearings but was insufficient to test for a 25 mil radial clearance bearing. The reason for this was because of the large pulsations associated with the replenishing (large) loop diaphragm pump. A recommendation to smooth out these pulsations is to insert an additional accumulator in the replenishing loop of the system. Another recommendation for this is

to replace the diaphragm pump with a centrifugal pump. This is a solution only if the stand pipe were the sand is added to the flow is after the outlet of a centrifugal pump. This would prevent the sand from being damaged within the pump.

Another recommendation is to redesign the splash guard to prevent liquid from leaking out of it. A dome shaped piece of metal could probably do a better job containing the flow.

Future work has already been started at the time of writing this thesis. Impact, or ring, testing on the rotor to determine the natural frequencies and associated mode shapes are important this information is important in having a holistic understanding of the rotordynamics of the system. This test will be conducted when the bearing annulus has no liquid in it as well as when it is full of liquid. The difference in these conditions can be validated when different gas volume fractions are run through the bearing annulus.

More in depth CFD simulations can also be looked at to validate the data that was measured in these tests.

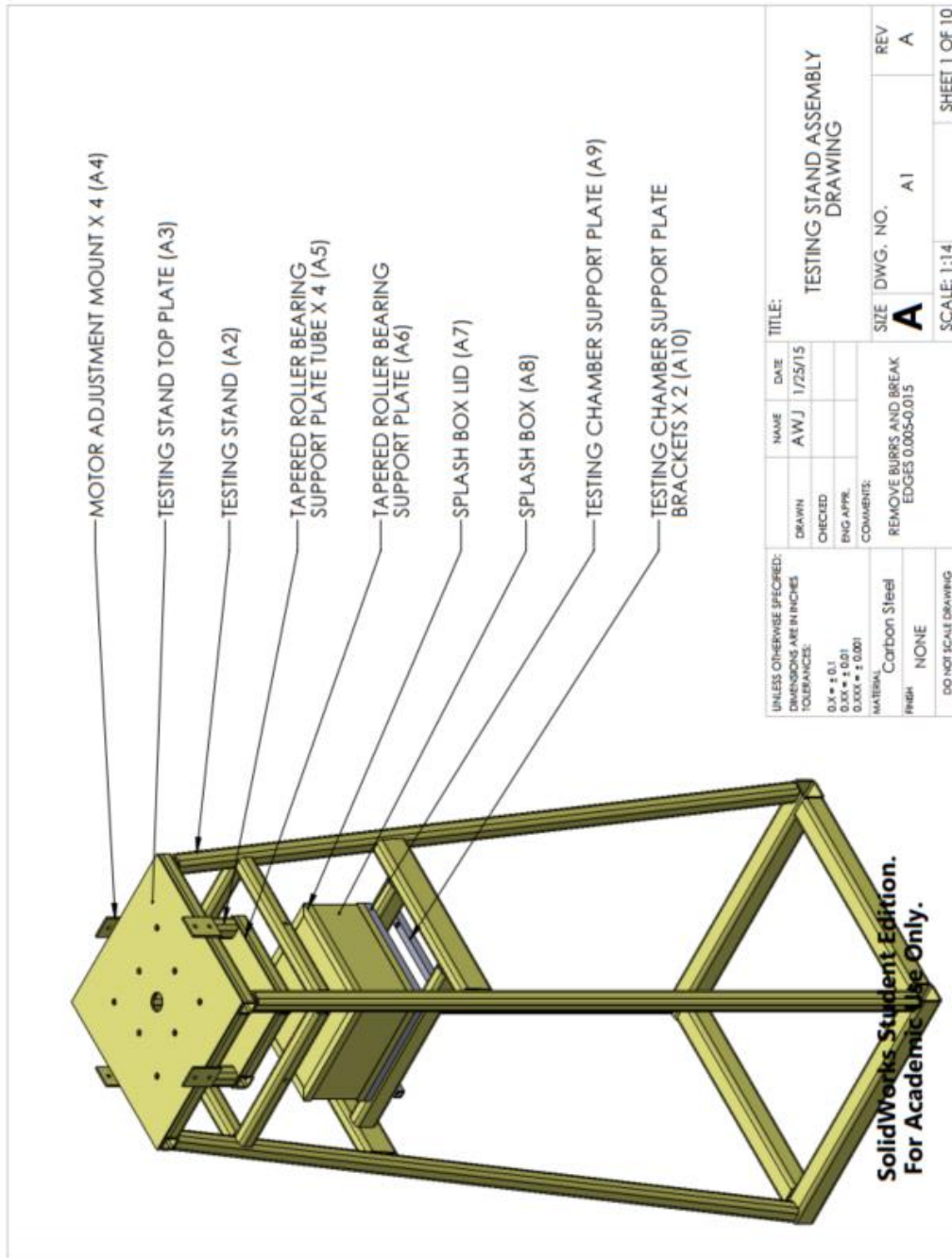
REFERENCES

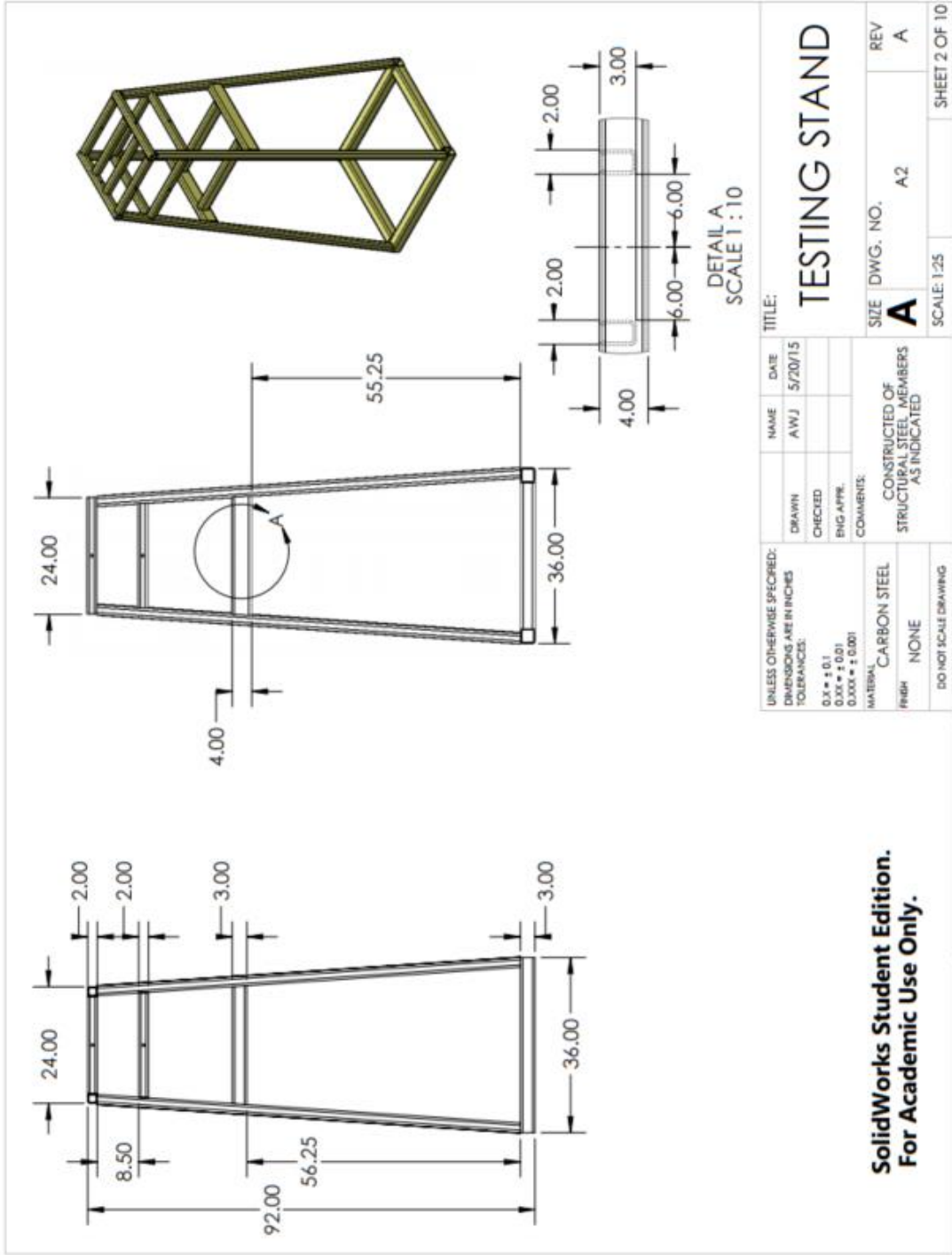
- [1] Takacs, Gabor. (2009) *Electrical Submersible Pumps Manual*, 1-355. Gulf Publishing Company
- [2] Swierczek, Martin. (2014) “Using Thermoplastic Composite Bearings in Vertical Water Pumps.” *Pumps & Systems*.
- [3] Zheng, Dezhi. (2013) “Three Phase Erosion Testing and Vibration Analysis of an Electrical Submersible Pump.” Thesis, Texas A&M University.
- [4] TURBOMACHINERY RESEARCH CONSORTIUM, 2014, “XLTRC2- Rotor Dynamic Software,” Department of Mechanical Engineering, Texas A&M University.
- [5] McMaster-Carr, 2014, “MODEL S05 Metallic Performance Curve,” McMaster-Carr, Atlanta, Georgia.
- [6] Philip J. Pritchard, 2011, Fox and McDonald’s Introduction to Fluid Mechanics, John Wiley and Sons, Danvers, Massachusetts, “Chapter 9.”
- [7] McMaster-Carr, 2014, “MODEL S30 Metallic Performance Curve,” McMaster-Carr, Atlanta, Georgia.
- [8] National Instruments, 2014, “NI C Series Module Compatibility Chart.”, from <http://www.ni.com/white-paper/8136/en/>, September 2014.

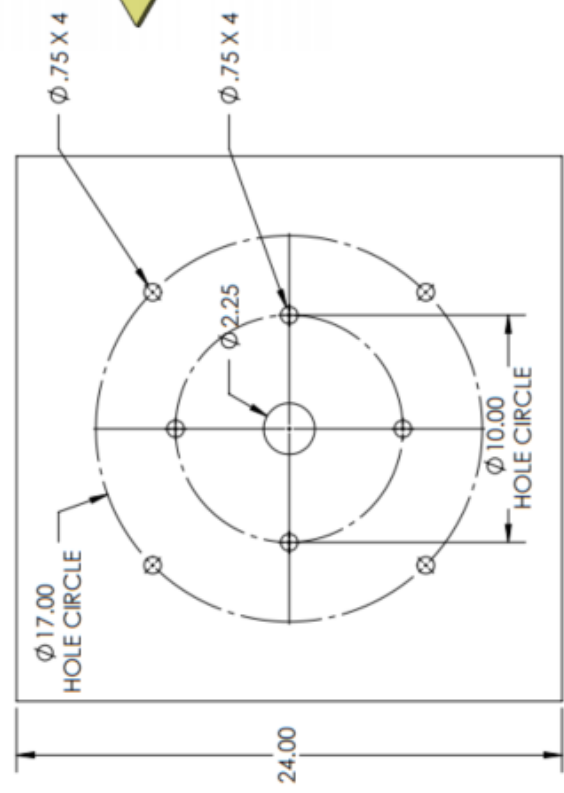
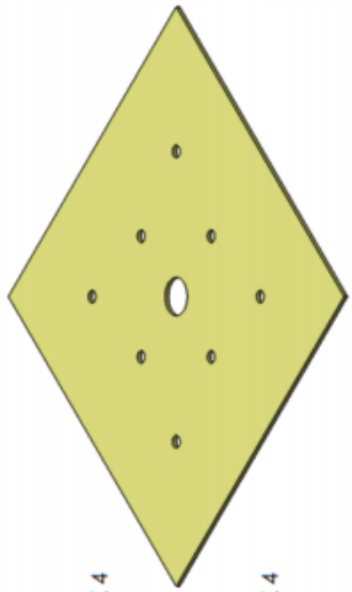
APPENDIX A

DRAWINGS

Assembly A: Testing Stand Drawings

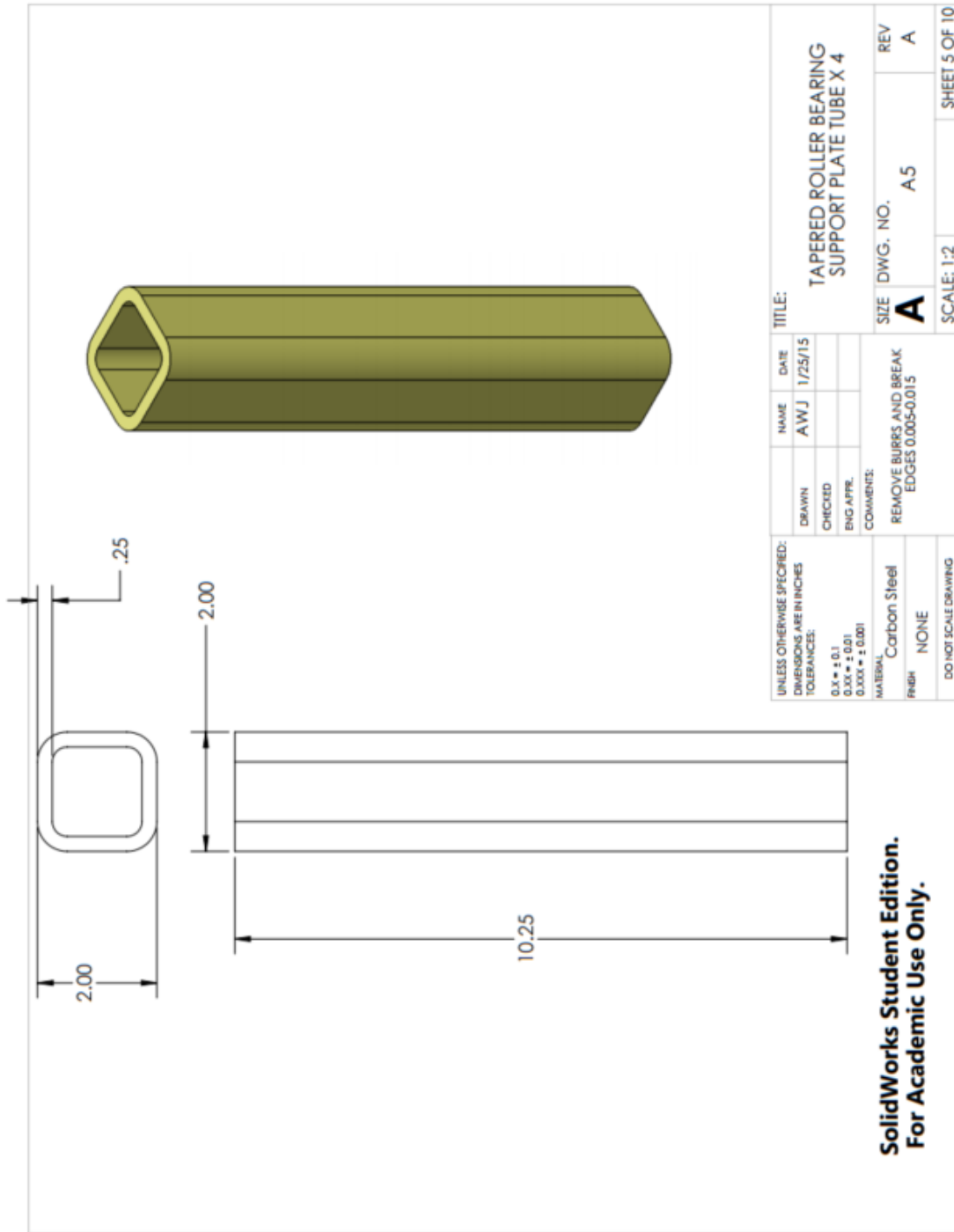


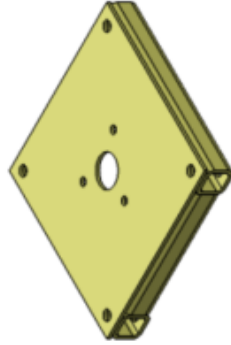
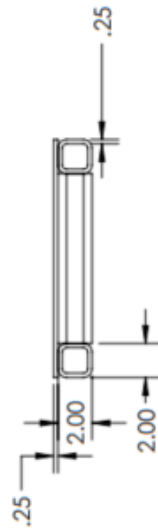
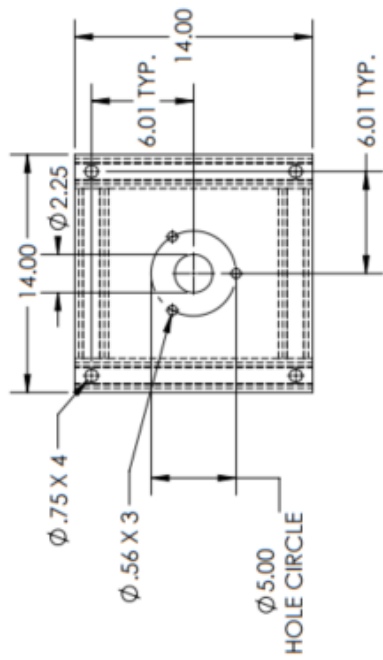




UNLESS OTHERWISE SPECIFIED: DIMENSIONS ARE IN INCHES TOLERANCES:		NAME	DATE	TITLE: TESTING STAND TOP PLATE
0.X ± 0.1	DRAWN	AWJ	1/25/15	
0.XX ± 0.01	CHECKED			
0.XXX ± 0.001	ENG APPR.			
MATERIAL: Carbon Steel	COMMENTS: REMOVE BURRS AND BREAK EDGES 0.005-0.015			SIZE DWG. NO. A
FINISH: NONE	DO NOT SCALE DRAWING			REV A
SCALE: 1:6				SHEET 3 OF 10

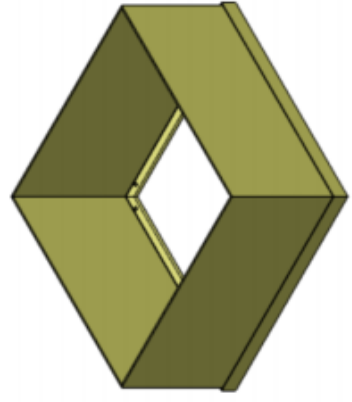
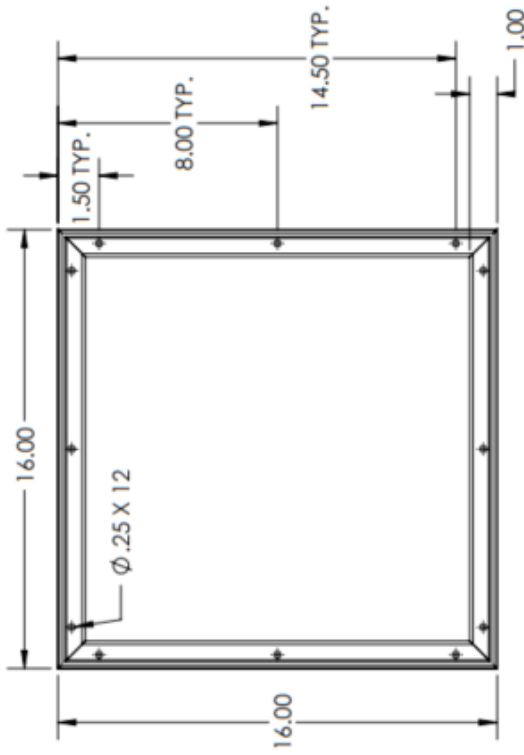
**SolidWorks Student Edition.
For Academic Use Only.**





UNLESS OTHERWISE SPECIFIED: DIMENSIONS ARE IN INCHES TOLERANCES:		DRAWN	NAME	DATE	TITLE:	
0.125 ± 0.1		CHECKED	AWJ	1/25/15	TAPERED ROLLER BEARING SUPPORT PLATE	
0.005 ± 0.001		ENG APPR.			SIZE	DWG. NO.
0.005 ± 0.001		COMMENTS:			A	A6
MATERIAL: Carbon Steel		REMOVE BURRS AND BREAK EDGES 0.005-0.015			REV	A
FINISH: NONE					SCALE: 1:8	SHEET 6 OF 10
DO NOT SCALE DRAWING						

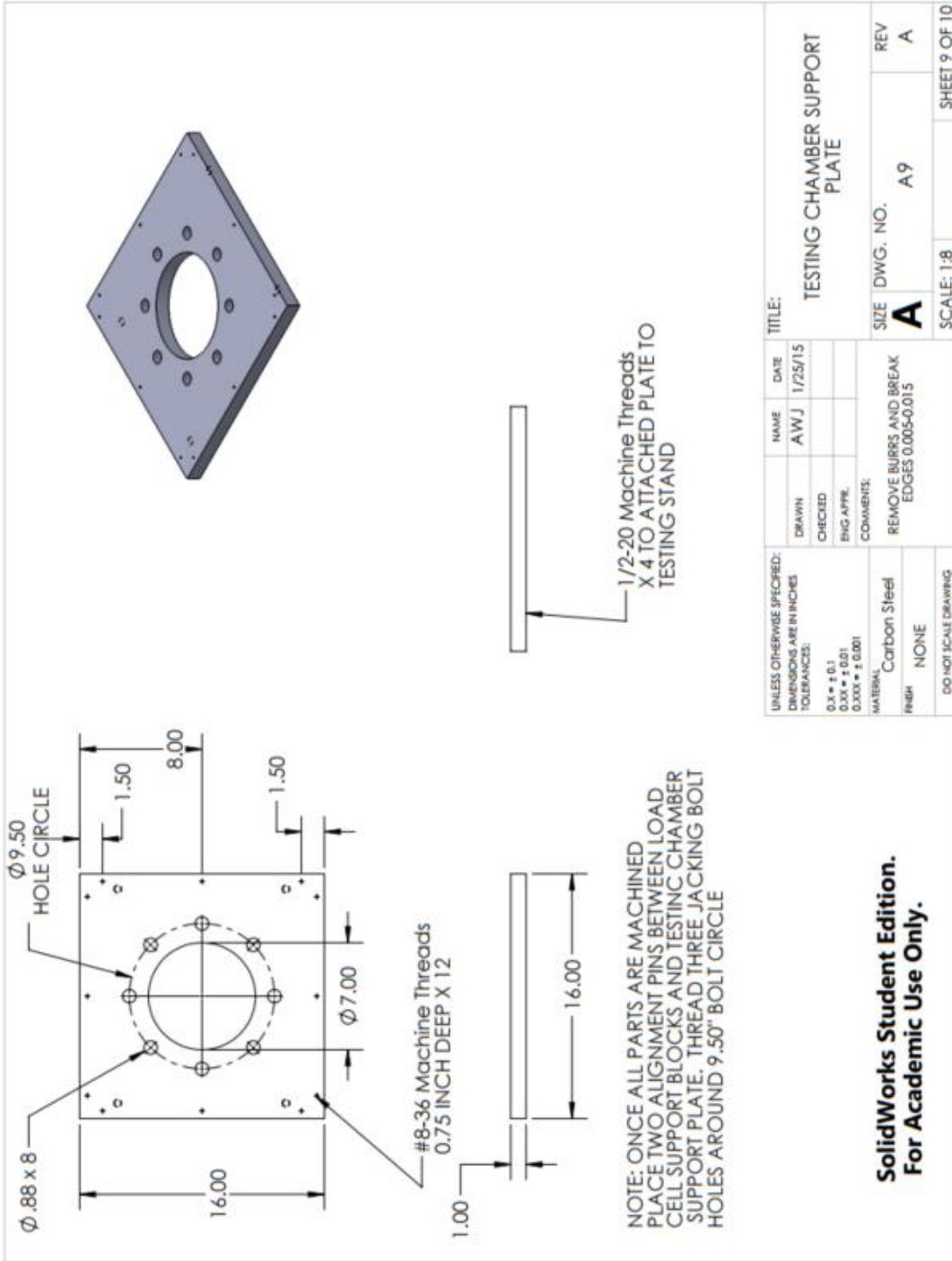
SolidWorks Student Edition.
For Academic Use Only.



**SolidWorks Student Edition.
For Academic Use Only.**

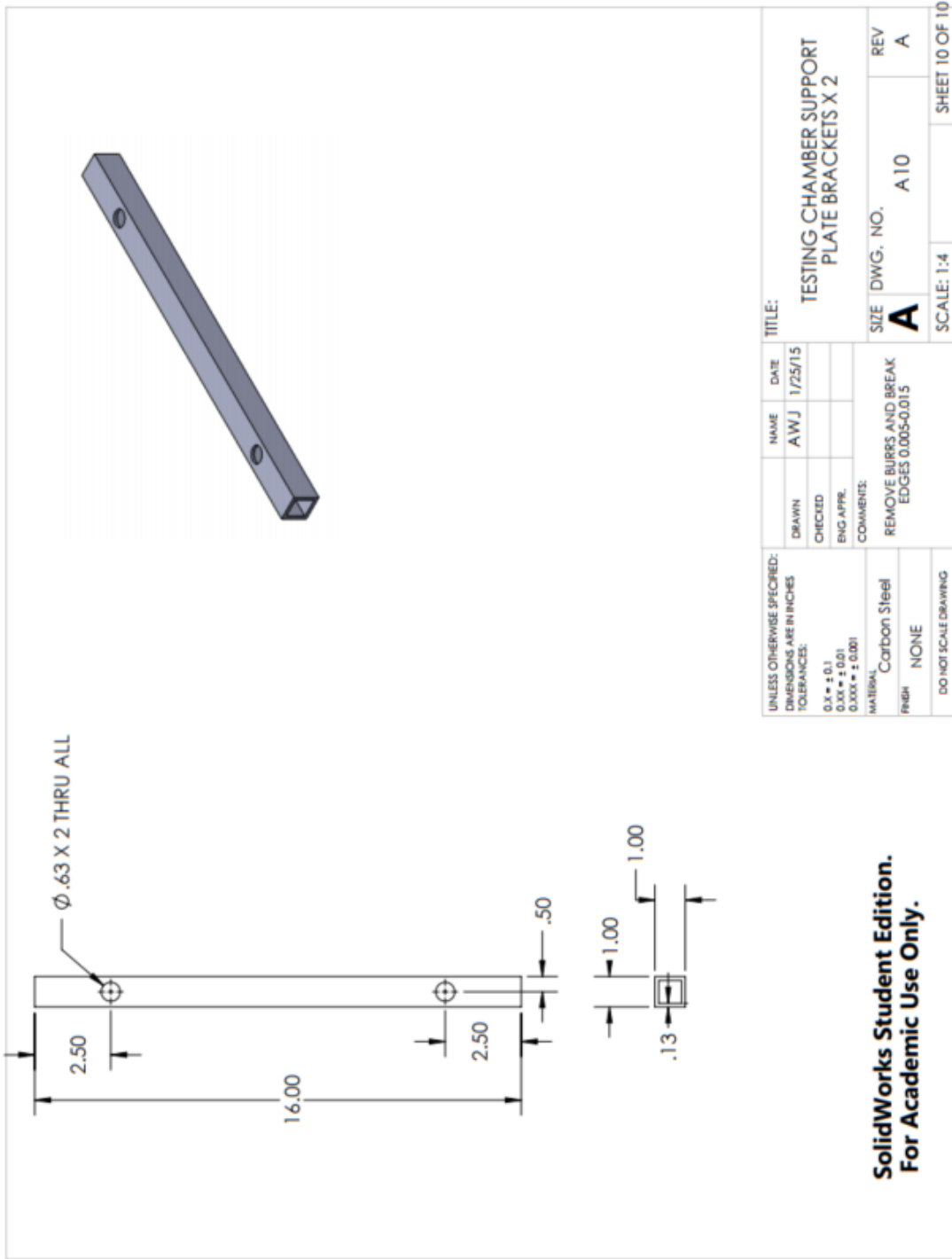
UNLESS OTHERWISE SPECIFIED: DIMENSIONS ARE IN INCHES TOLERANCES:		NAME	DATE	TITLE:	
DRAWN	AWJ	1/25/15	SPLASH BOX		
CHECKED					
ENG. APPR.					
COMMENTS:		REMOVE BURRS AND BREAK EDGES 0.005-0.015		SIZE	DWG. NO.
MATERIAL: Carbon Steel		A		A8	REV
FINISH: NONE		SCALE: 1:5		A	A
DO NOT SCALE DRAWING		SHEET 8 OF 10		1	

1 2 3 4 5

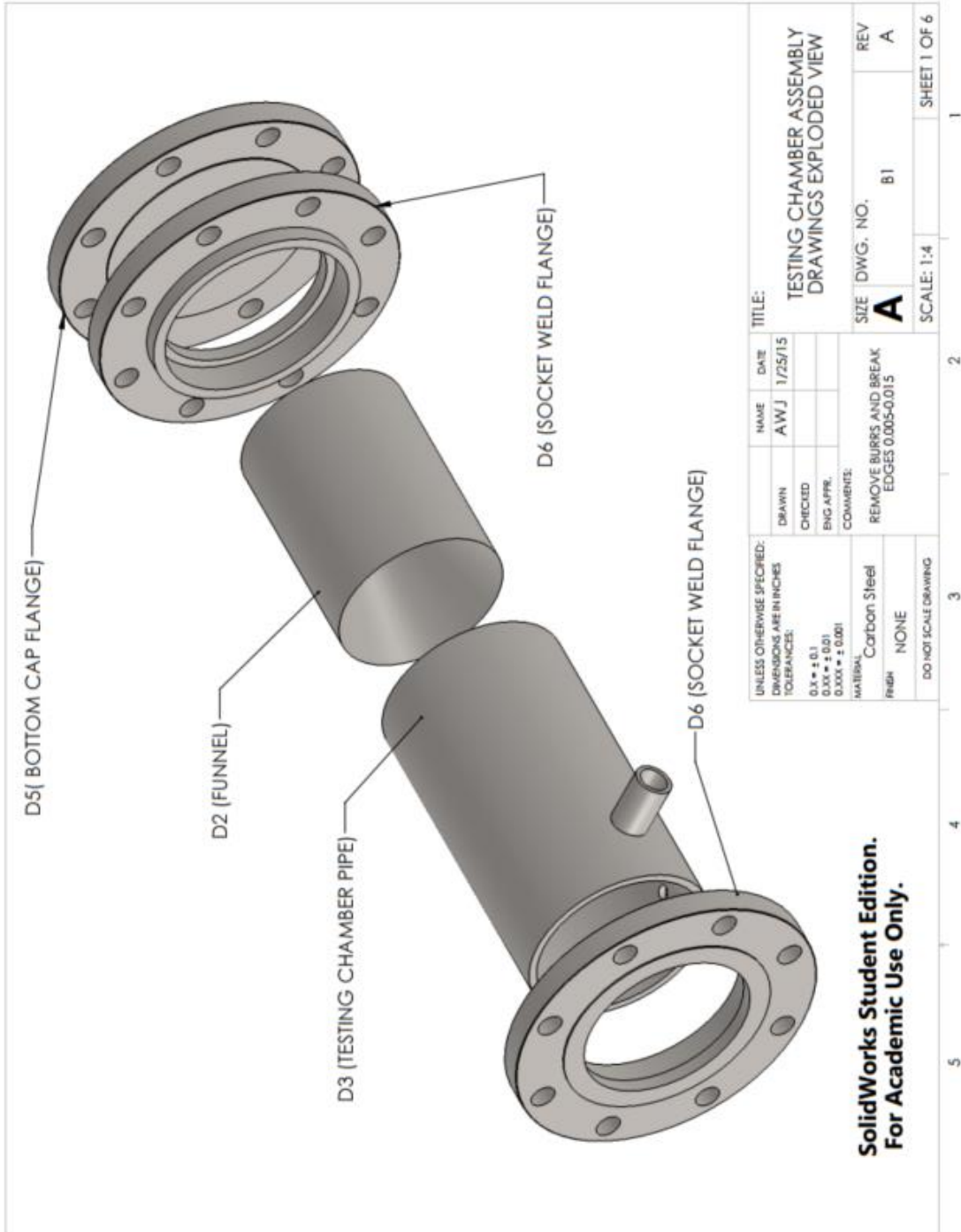


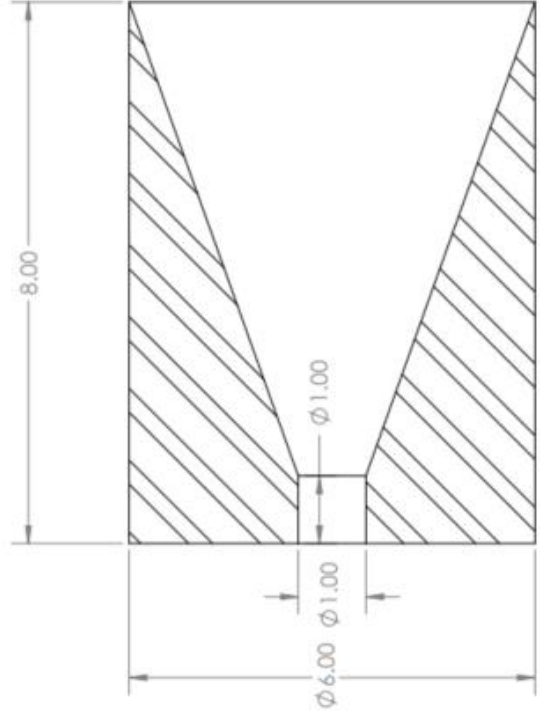
**SolidWorks Student Edition.
For Academic Use Only.**

UNLESS OTHERWISE SPECIFIED: DIMENSIONS ARE IN INCHES		NAME	DATE	TITLE:
DRAWN	CHECKED	AWJ	1/25/15	TESTING CHAMBER SUPPORT PLATE
TOLERANCES: 0.1" = ± 0.1 0.001" = ± 0.001 0.0005" = ± 0.0005		ENG APPR.		SIZE DWG. NO. A A9
MATERIAL Carbon Steel		COMMENTS: REMOVE BURRS AND BREAK EDGES 0.005-0.015		REV A
FINISH NONE		DO NOT SCALE DRAWING		SCALE: 1:8



Assembly B: Testing Chamber Drawings



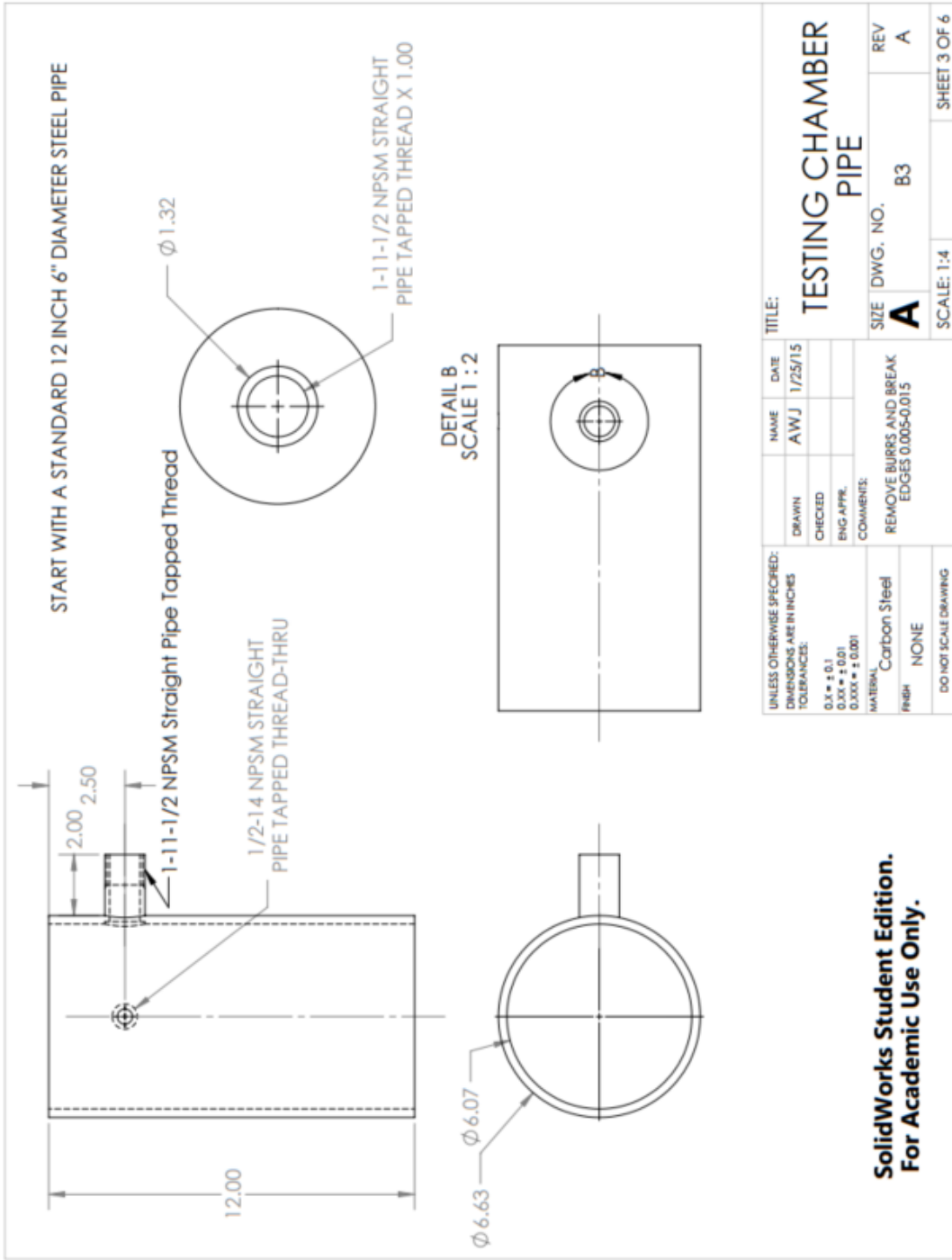


SECTION A-A
SCALE 1 : 2

UNLESS OTHERWISE SPECIFIED: DIMENSIONS ARE IN INCHES TOLERANCES:		NAME	DATE	TITLE:
0.125 ± 0.1		AWJ	1/25/15	FUNNEL
0.000 ± 0.01		DRAWN		
0.000 ± 0.001		CHECKED		
		ENG. APPL.		
		COMMENTS:		SIZE DWG. NO.
		REMOVE BURRS AND BREAK EDGES 0.005-0.015		A B2
MATERIAL: Carbon Steel				REV
FINISH: NONE				A
DO NOT SCALE DRAWING				SCALE: 1:2
				SHEET 2 OF 6

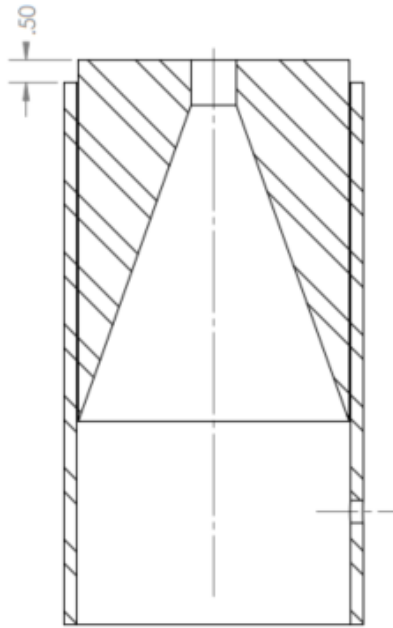
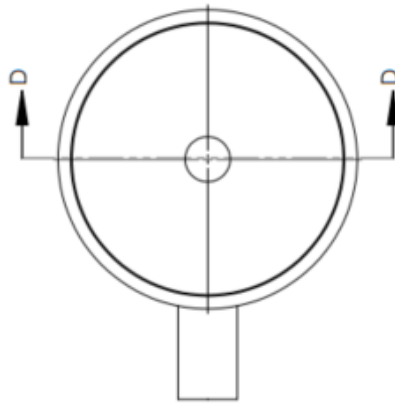
**SolidWorks Student Edition.
For Academic Use Only.**

1 2 3 4 5



**SolidWorks Student Edition.
For Academic Use Only.**

WELD D2 INSIDE D3 AS SHOWN



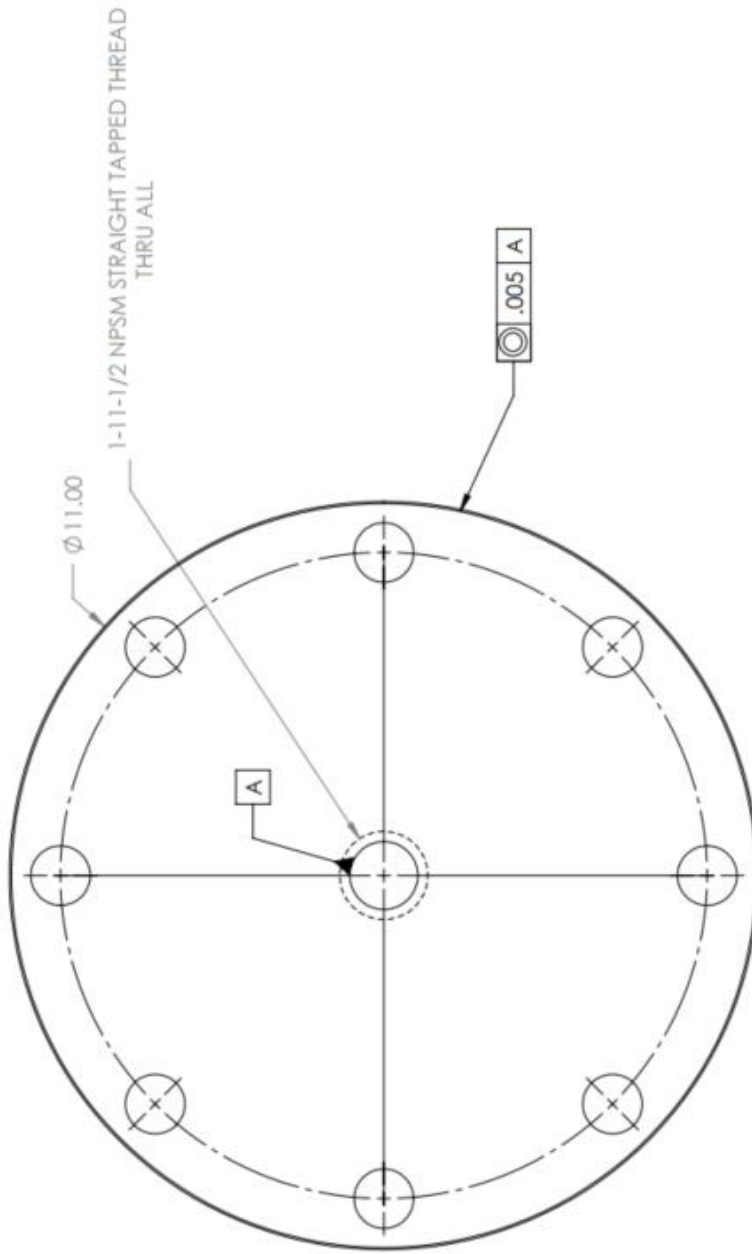
SECTION D-D
SCALE 1:3

**SolidWorks Student Edition.
For Academic Use Only.**

UNLESS OTHERWISE SPECIFIED: DIMENSIONS ARE IN INCHES TOLERANCES:		NAME	DATE	TITLE:	
D.X. ± 0.1	DRAWN	AWJ	1/25/15	WELD FUNNEL INSIDE PIPE	
D.X.X. ± 0.01	CHECKED			SIZE	DWG. NO.
D.X.X.X. ± 0.001	ENG. APPR.			A	B4
MATERIAL	COMMENTS:	REMOVE BURRS AND BREAK EDGES 0.005-0.015		REV	A
Carbon Steel				SCALE: 1:3	SHEET 4 OF 6
FINISH	DO NOT SCALE DRAWING				
NONE					

5 4 3 2 1

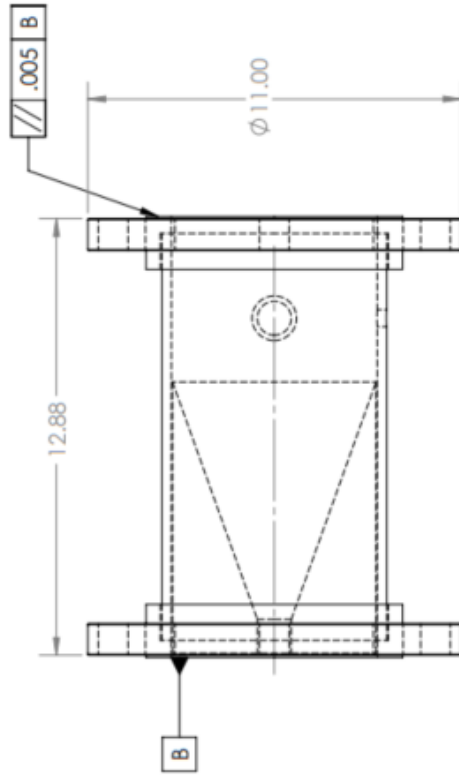
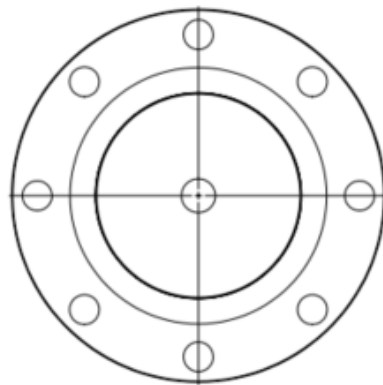
START WITH A STANDARD 6 INCH STEEL PIPE END FLANGE



UNLESS OTHERWISE SPECIFIED: DIMENSIONS ARE IN INCHES TOLERANCES:		NAME	DATE	TITLE:	
0.X * ± 0.1		AWJ	1/25/15	BOTTOM CAP FLANGE	
0.XX * ± 0.01		CHECKED		SIZE	DWG. NO.
0.XXX * ± 0.001		END APPR.		A	B5
		COMMENTS:		REV	A
MATERIAL	Carbon Steel	REMOVE BURRS AND BREAK EDGES 0.005-0.015		SCALE:	1:2
FINISH	NONE				
DO NOT SCALE DRAWING					

**SolidWorks Student Edition.
For Academic Use Only.**

WELD TWO SOCKET FLANGES ONTO BOTH ENDS OF THE 6 INCH PIPE.



UNLESS OTHERWISE SPECIFIED:
DIMENSIONS ARE IN INCHES
TOLERANCES:
0.1 ± 0.1
0.00 ± 0.01
0.000 ± 0.001
MATERIAL: Carbon Steel
FINISH: NONE
DO NOT SCALE DRAWING

DRAWN: A W J
CHECKED: []
ENG. APPR. []
COMMENTS:
REMOVE BURRS AND BREAK
EDGES 0.005-0.015

TITLE:

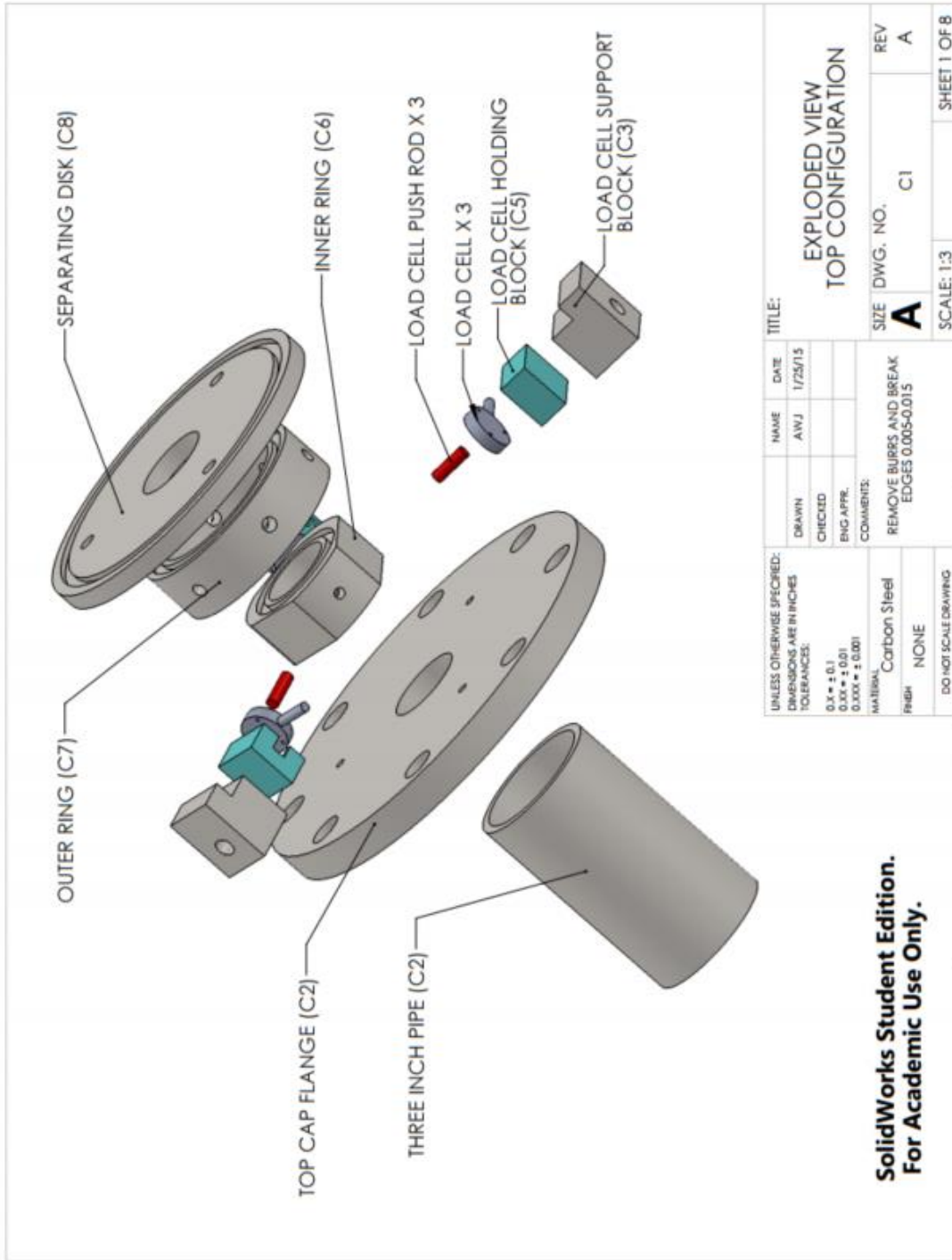
WELD 2 SOCKET
FLANGES ON PIPE

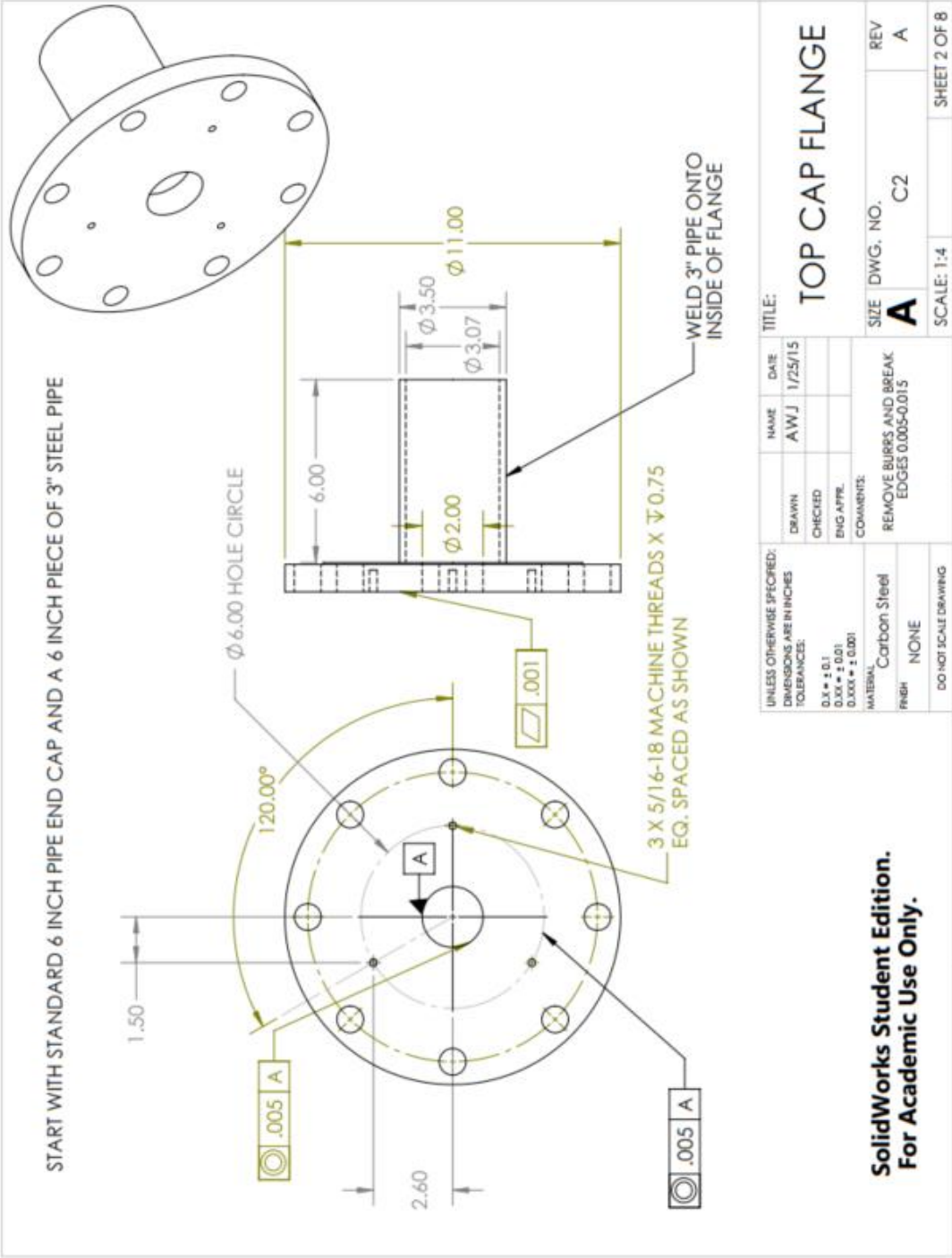
SIZE DWG. NO. B6
REV A

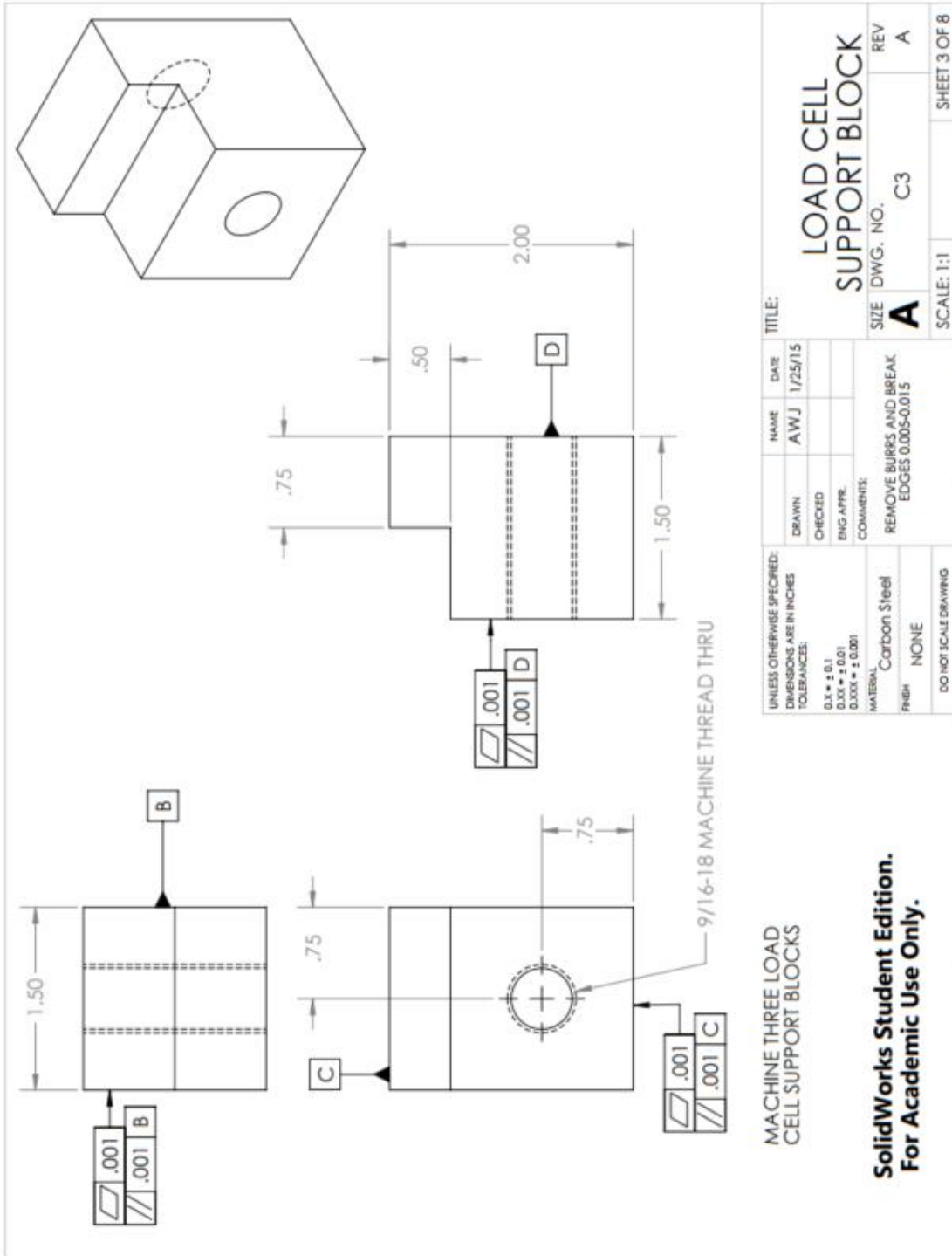
SCALE: 1:4 SHEET 6 OF 6

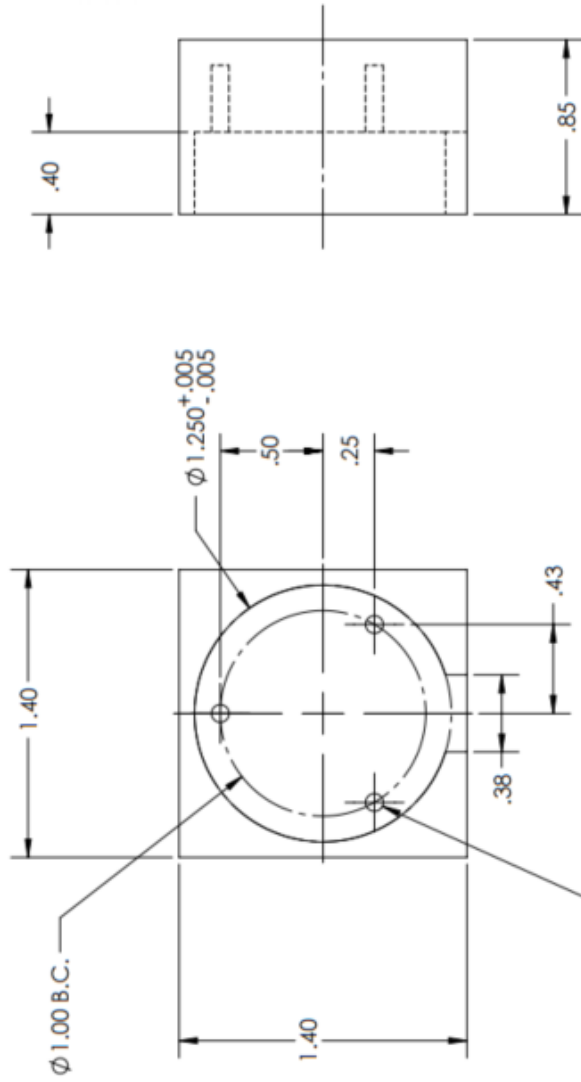
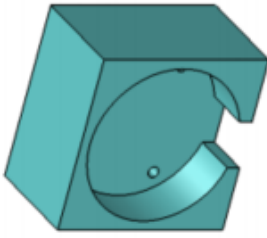
**SolidWorks Student Edition.
For Academic Use Only.**

Assembly C: Top Configuration







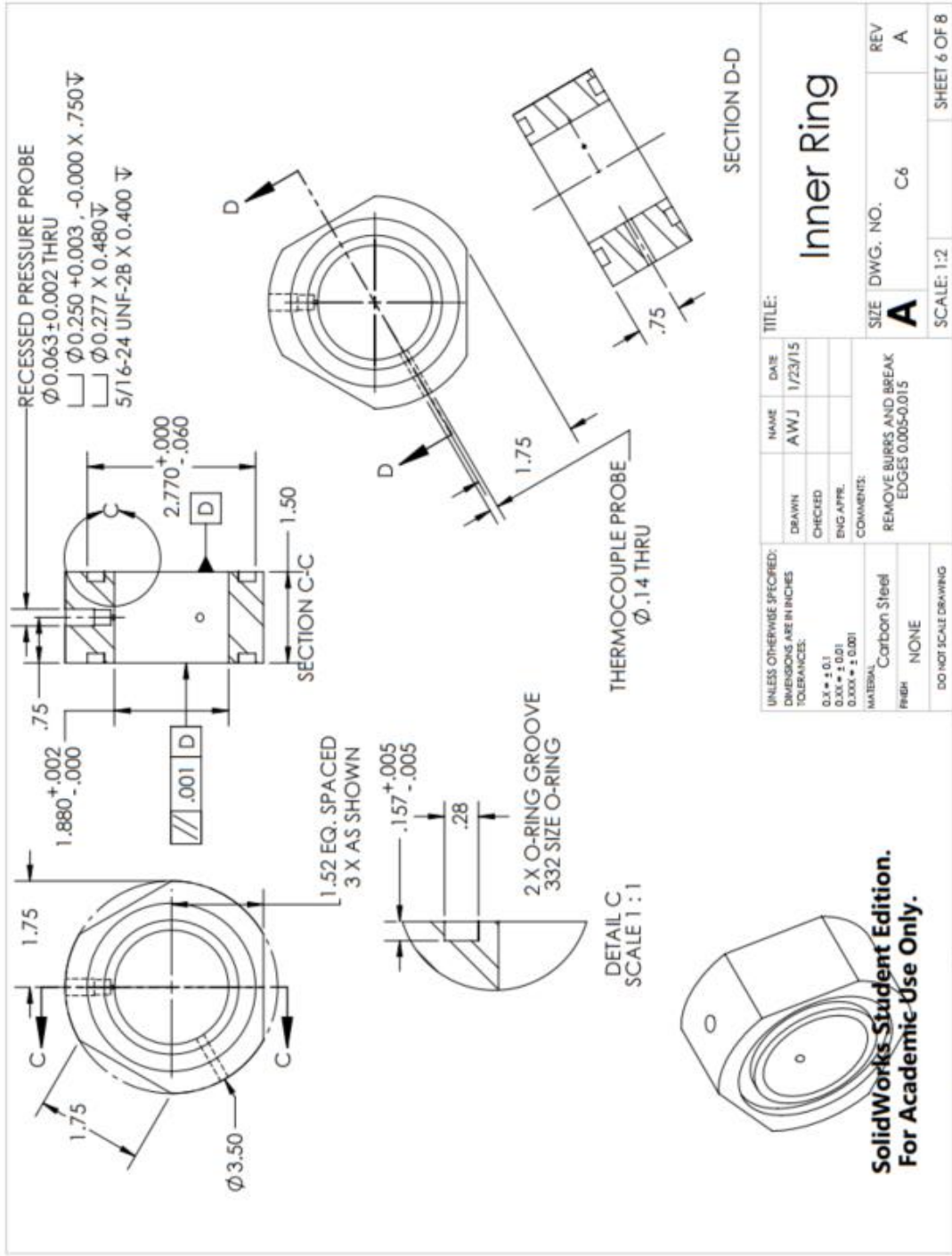


3 X $\phi .086$, $\nabla 0.33$
 TAP #2-56 MACHINE THREAD
 EQ. SPACES AS SHOWN

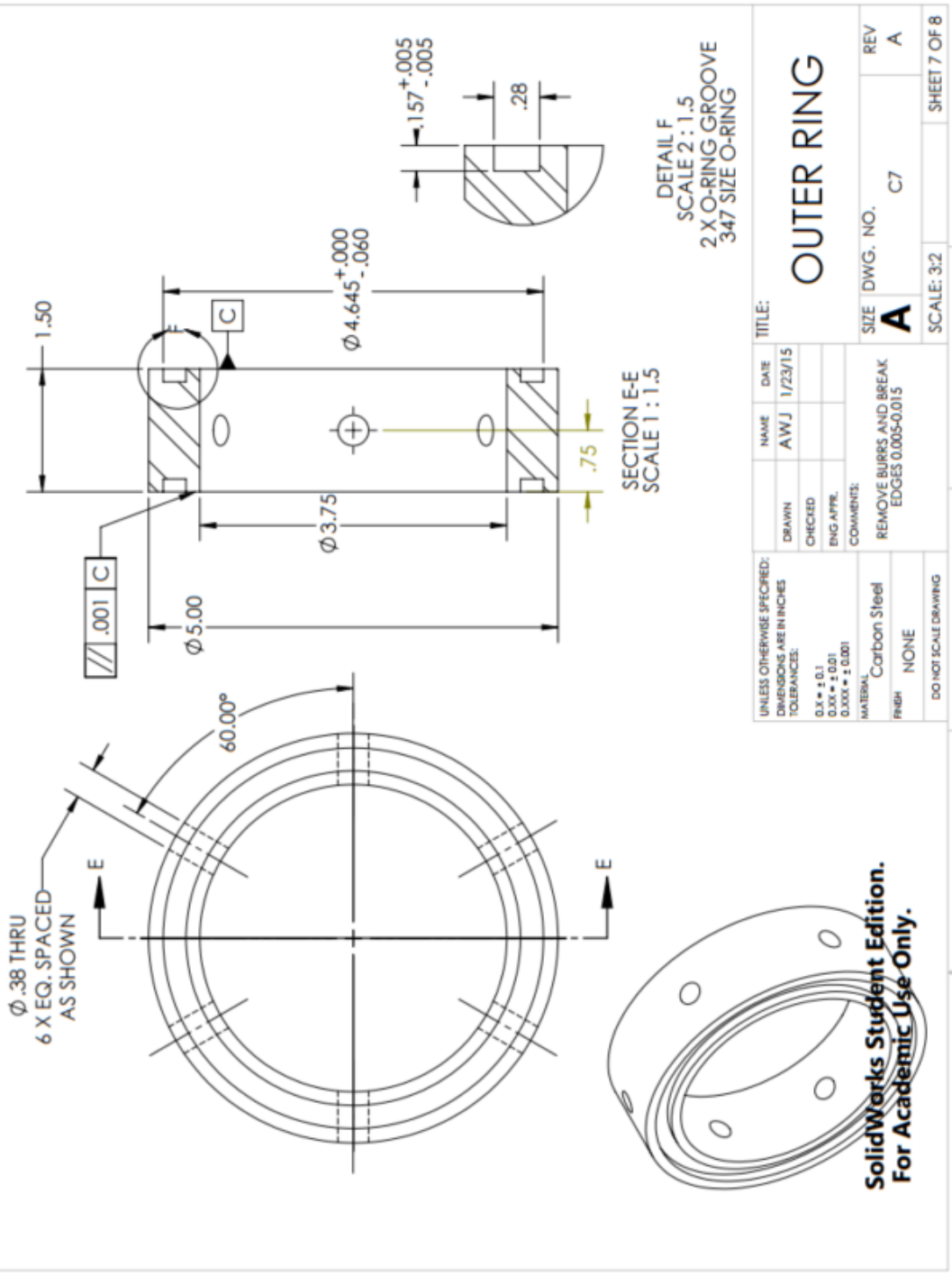
MACHINE THREE OF THIS PART

UNLESS OTHERWISE SPECIFIED: DIMENSIONS ARE IN INCHES		NAME	DATE	TITLE:
DRAWN	AWJ	AWJ	1/23/15	Load Cell Block
CHECKED				
ENG. APPR.				
TOLERANCES:		COMMENTS:		
0.X * ± 0.1		REMOVE BURRS AND BREAK		
0.XX * ± 0.01		EDGES 0.005-0.015		
0.XXX * ± 0.001				
MATERIAL	Carbon Steel	SIZE	DWG. NO.	REV
FINISH	NONE	A	C5	A
DO NOT SCALE DRAWING		SCALE: 3:2		SHEET 5 OF 8

**SolidWorks Student Edition.
 For Academic Use Only.**



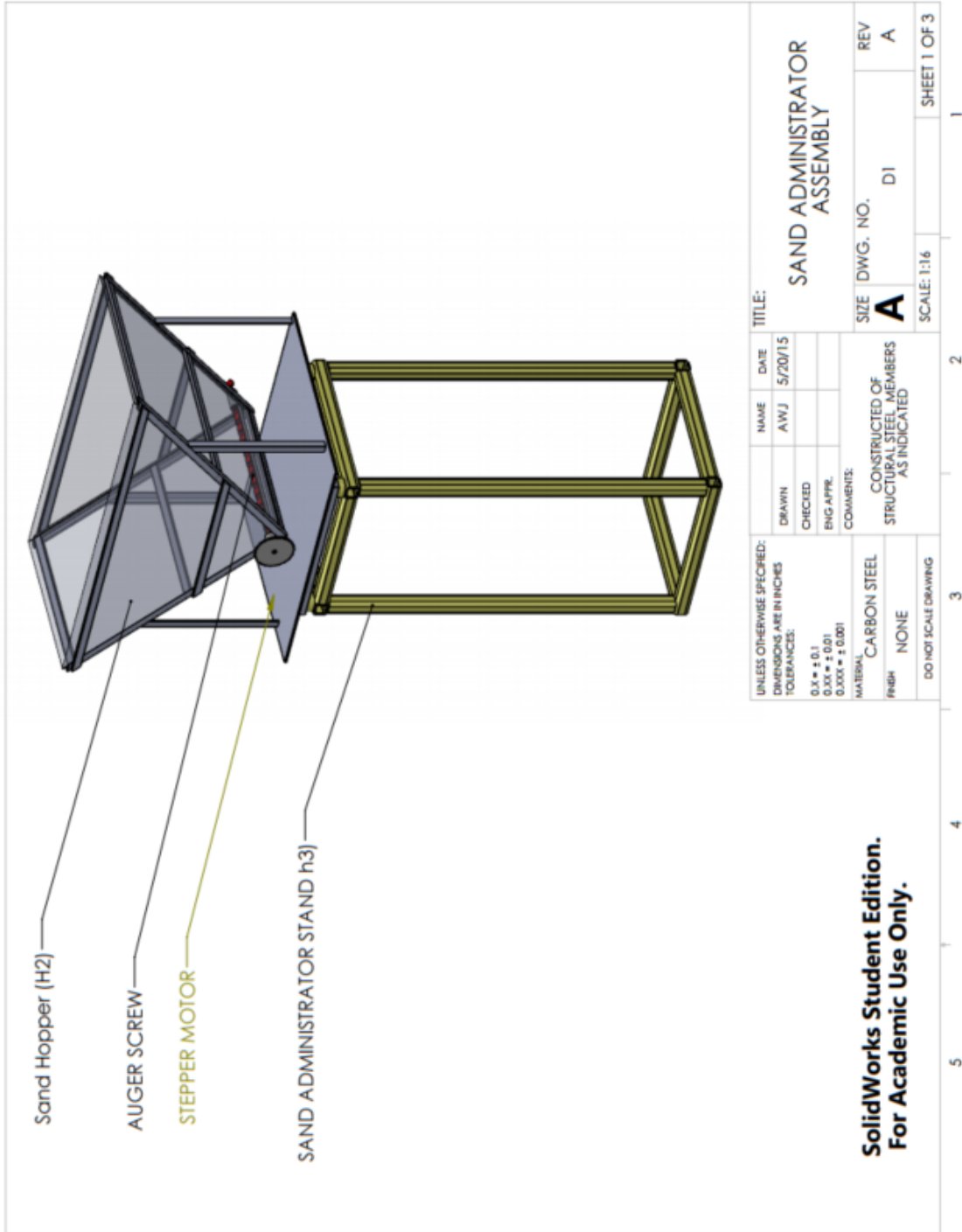
SolidWorks Student Edition.
For Academic Use Only.



UNLESS OTHERWISE SPECIFIED: DIMENSIONS ARE IN INCHES		NAME	DATE
TOLERANCES:		AWJ	1/23/15
0.X ± 0.1			
0.XX ± 0.01			
0.XXX ± 0.001			
MATERIAL: Carbon Steel		TITLE: OUTER RING	
FINISH: NONE		SIZE DWG. NO. C7	
DO NOT SCALE DRAWING		REV A	
		SCALE: 3:2	
		SHEET 7 OF 8	

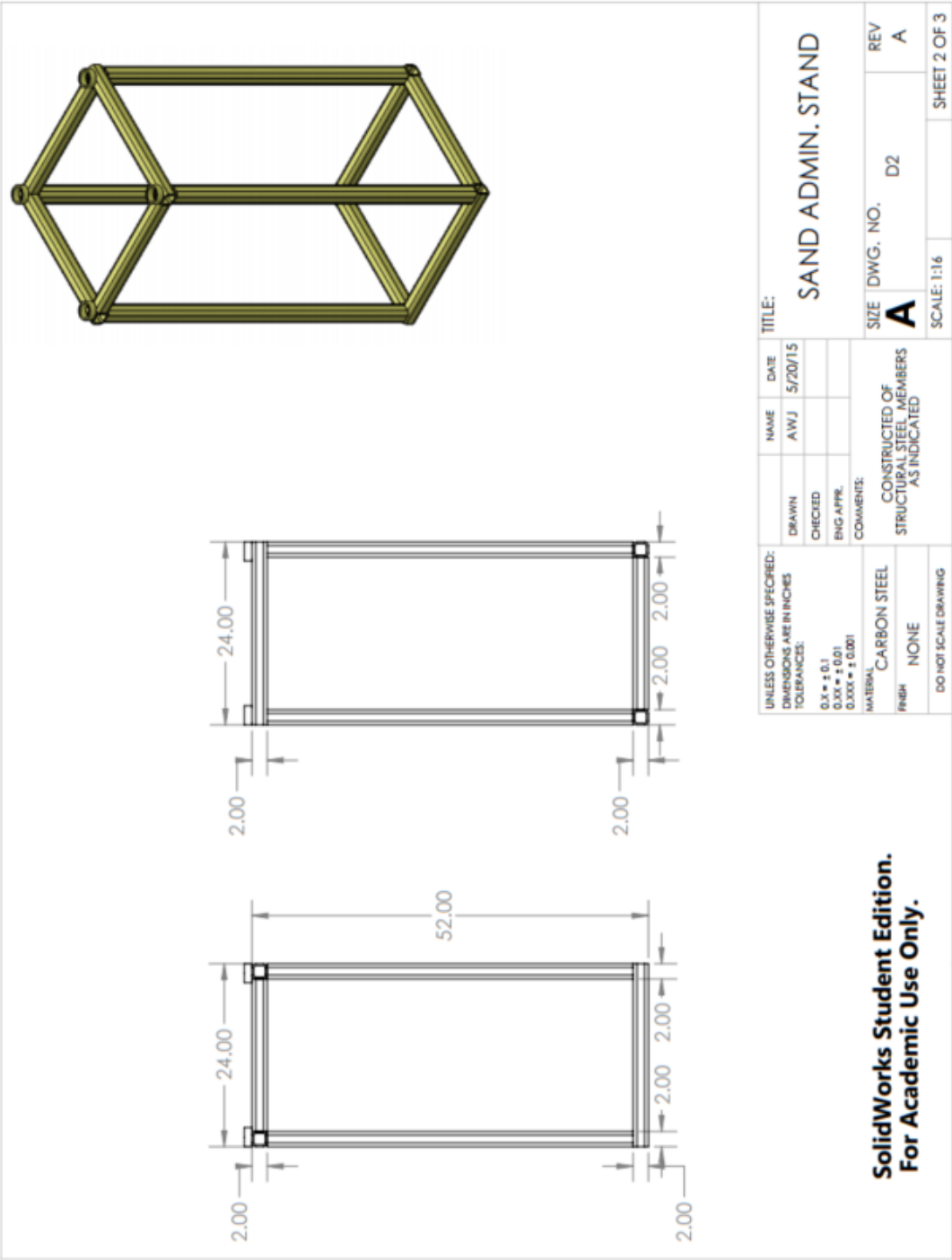
SolidWorks Student Edition.
For Academic Use Only.

Assembly D: Sand Administrator

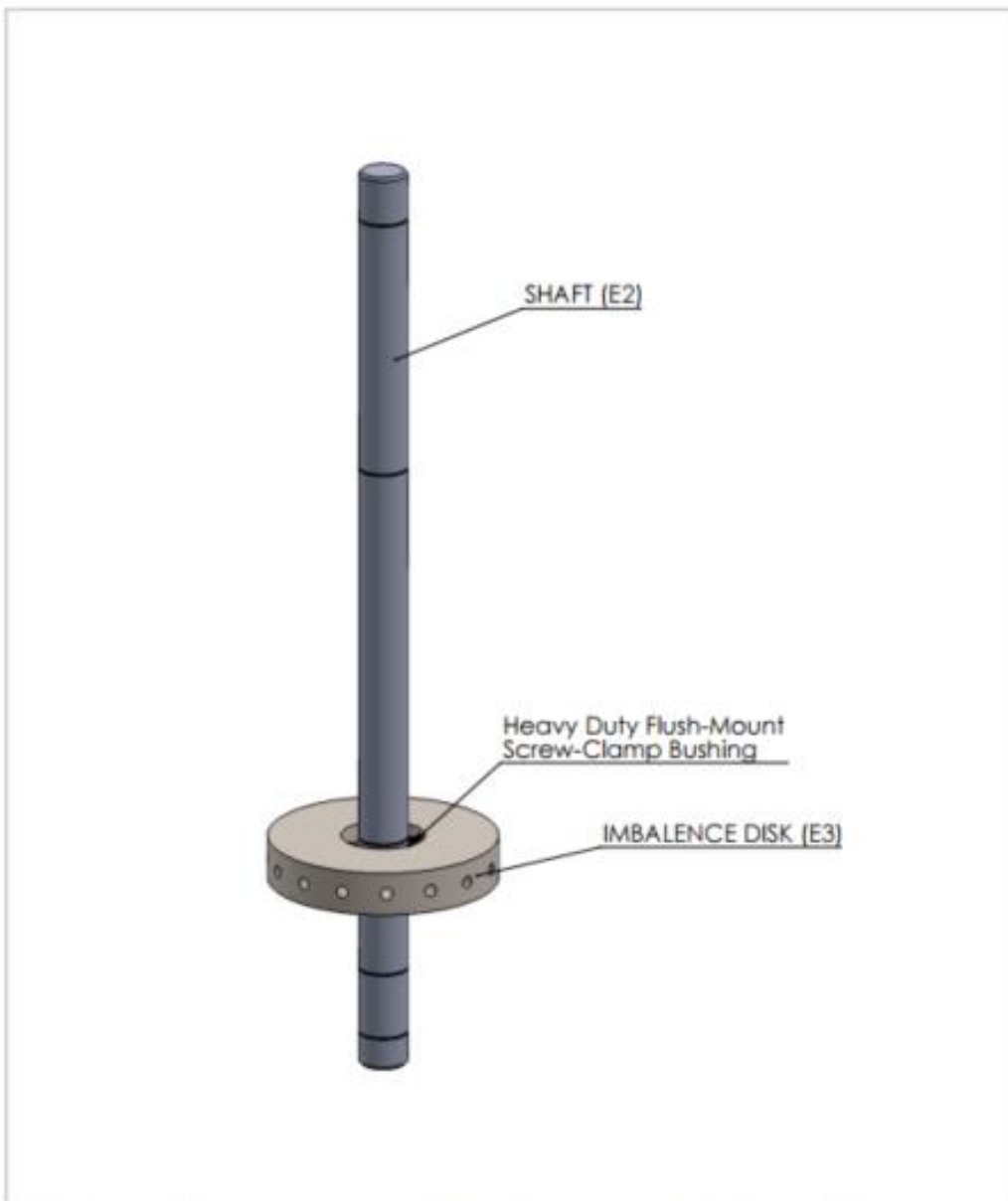


**SolidWorks Student Edition.
For Academic Use Only.**

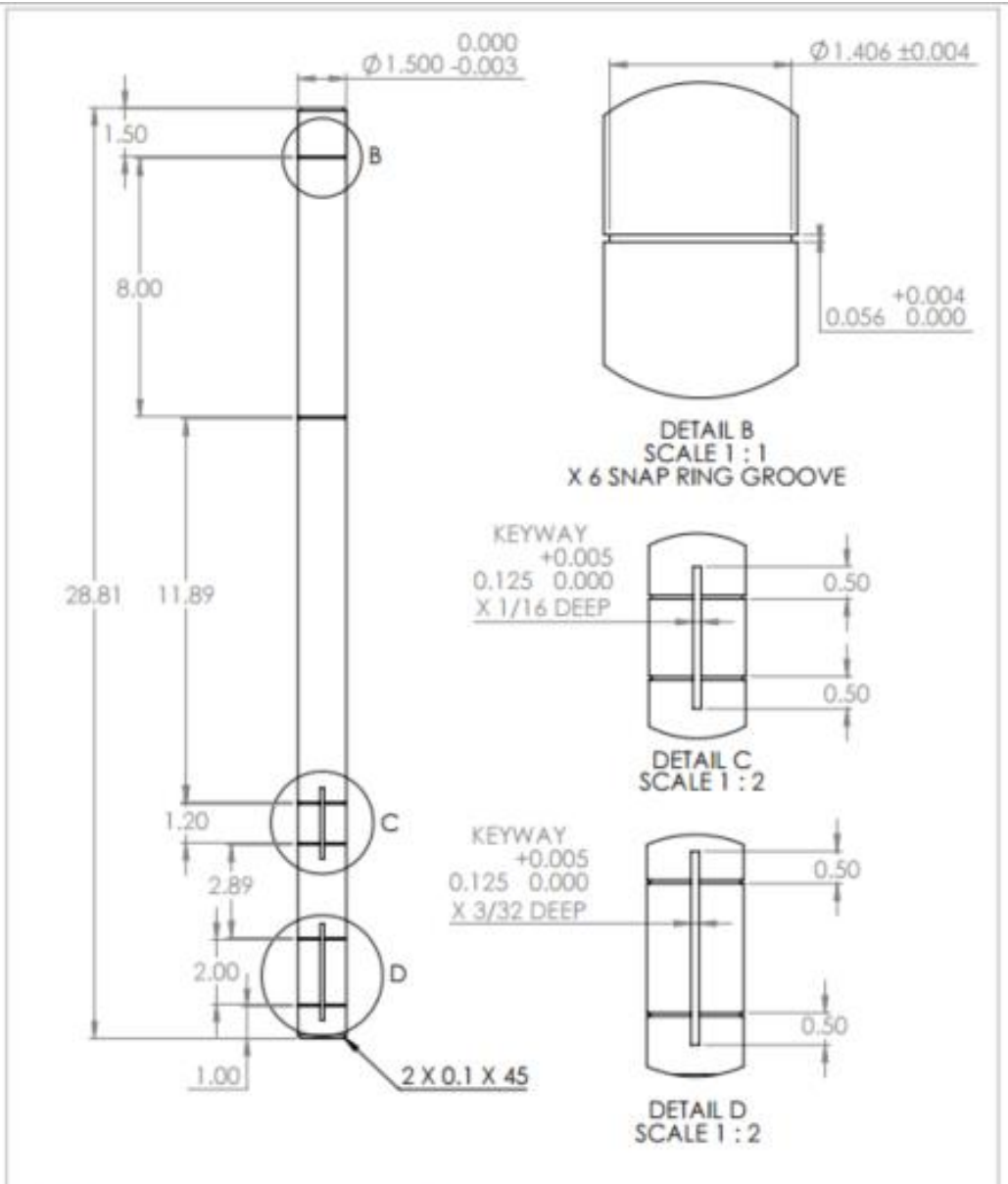
UNLESS OTHERWISE SPECIFIED: DIMENSIONS ARE IN INCHES TOLERANCES:		DRAWN	NAME	DATE	TITLE:	
0.XX ± 0.1		CHECKED	AWJ	5/20/15	SAND ADMINISTRATOR ASSEMBLY	
0.XX ± 0.01		ENG APPR.			SIZE	DWG. NO.
0.XXX ± 0.001		COMMENTS:			A	D1
MATERIAL:	CARBON STEEL	CONSTRUCTED OF STRUCTURAL STEEL MEMBERS AS INDICATED			REV	A
FINISH:	NONE				SCALE: 1:16	SHEET 1 OF 3
DO NOT SCALE DRAWING						



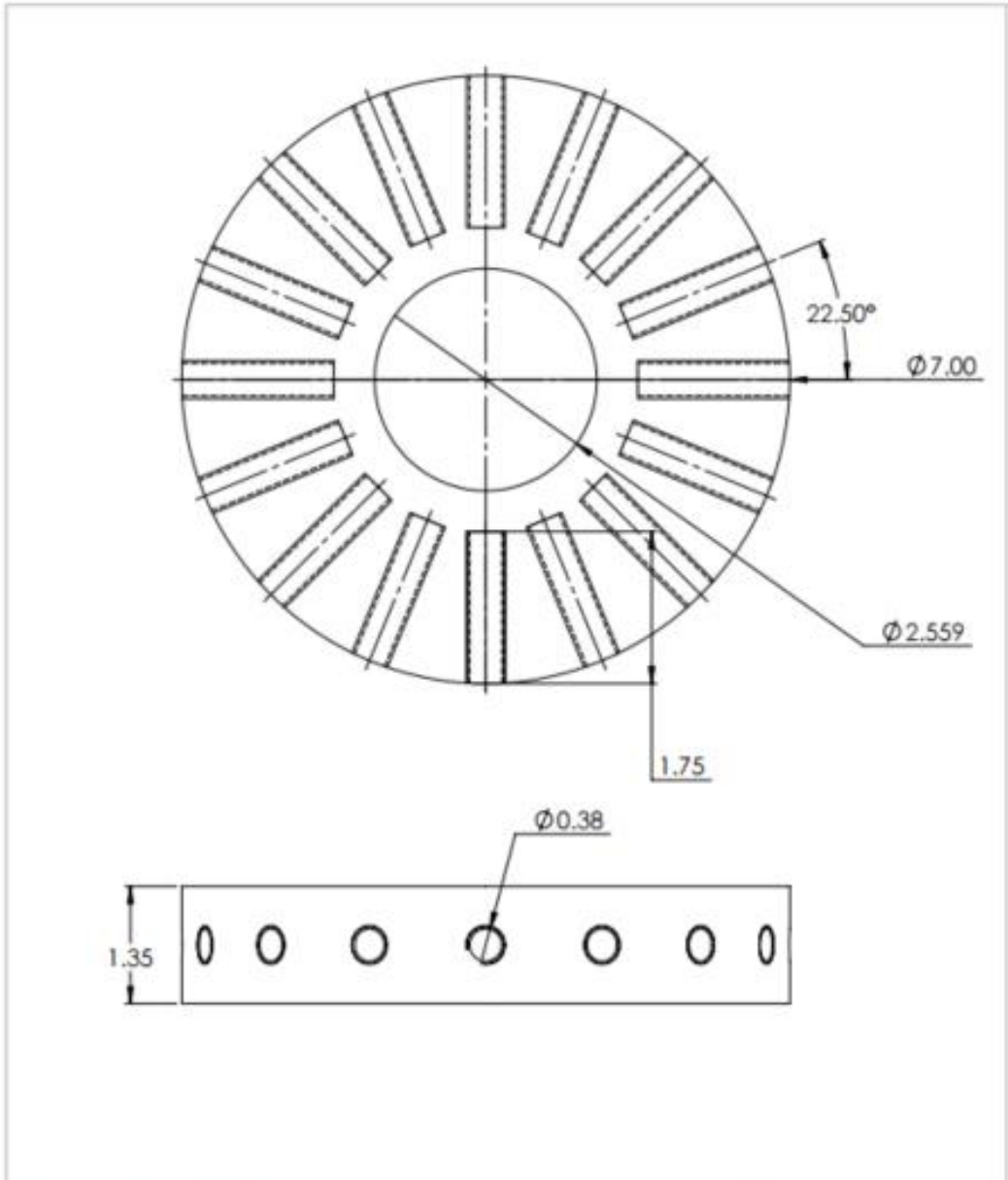
Assembly E: Shaft and Imbalance Disk



DIMENSIONS ARE IN INCHES		TOLERANCES:		ORDER AND BREAK SHARP EDGES	DO NOT SCALE DRAWING	REVISION
D.X = ± 0.1		D.XX = ± 0.01				
D.XXX = ± 0.001				TITLE SHAFT AND IMBALANCE DISK ASSEMBLY		
DRAWN	NAME	SIGNATURE	DATE			
DWD	AKJ		4/12/2015			
APP'D						
MFG						
GA			MATERIAL	DRG NO.	E1	
				SCALE: 1:1	SHEET 1 OF 3	

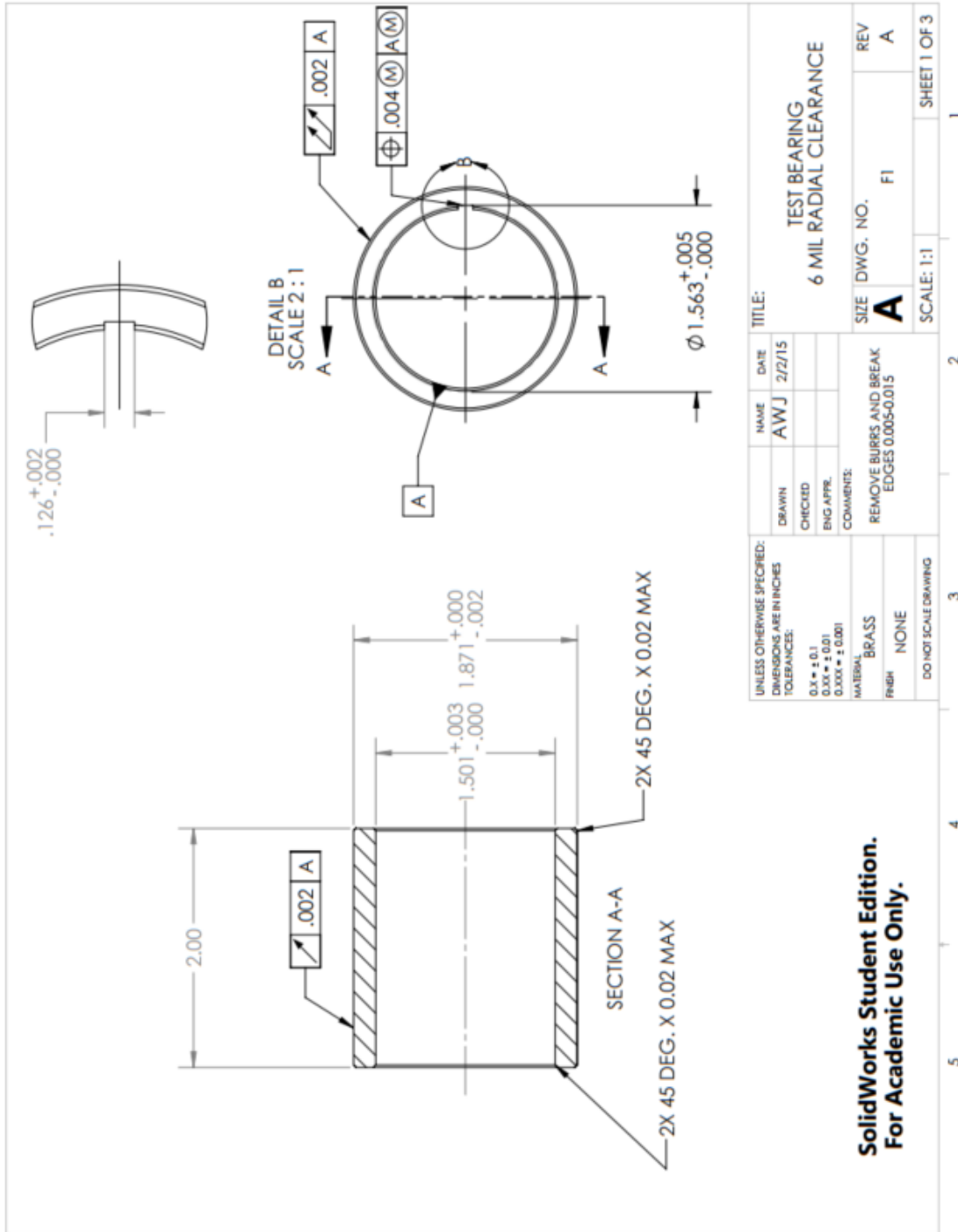


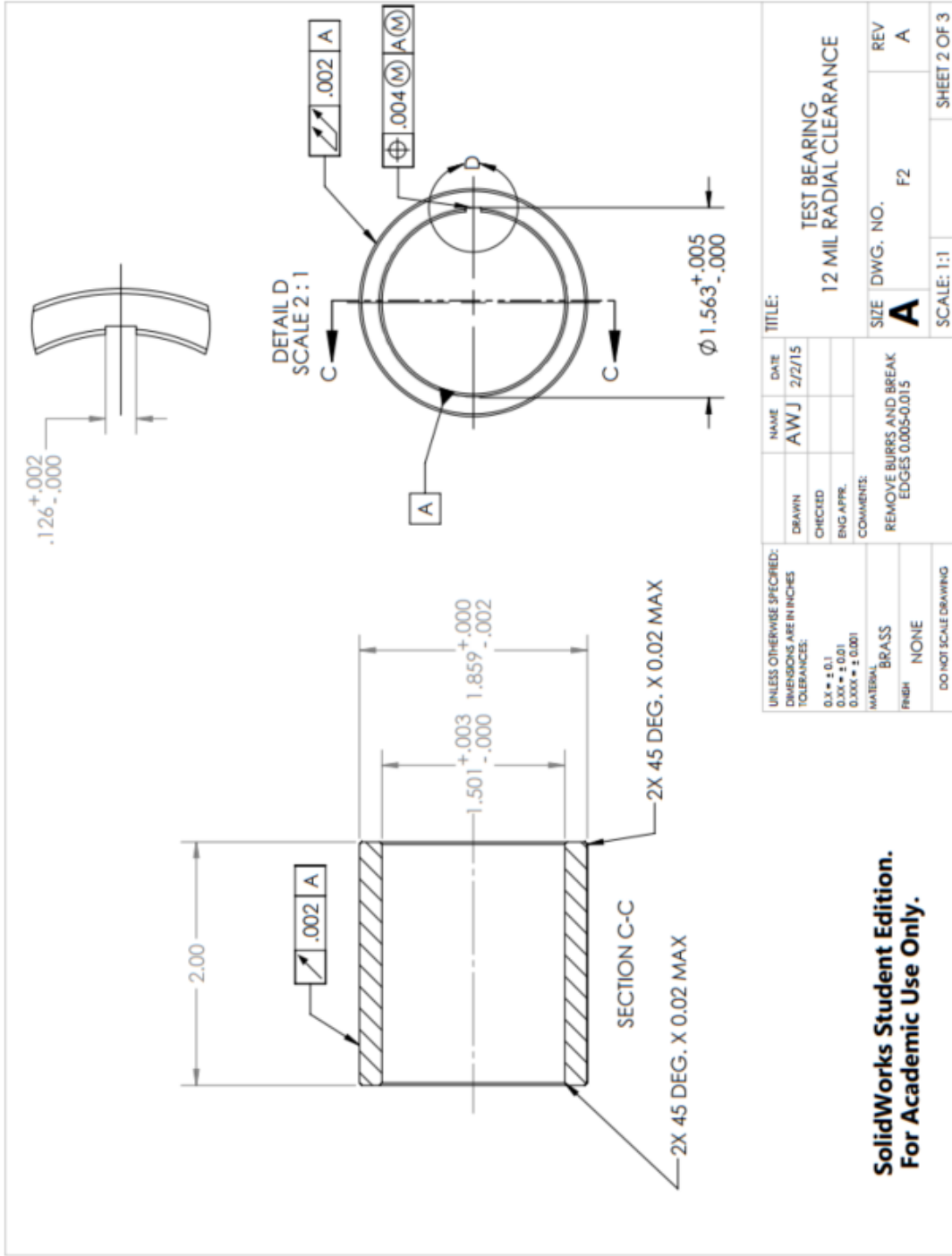
DIMENSIONS ARE IN INCHES TOLERANCES: 0.X = ± 0.1 0.XX = ± 0.01 0.XXX = ± 0.001		FINISH MACH RA 125		DEBUR AND BREAK SHARP EDGES	DO NOT SCALE DRAWING	REVISION
NAME	SIGNATURE	DATE			INCONEL SHAFT	
DRAWN AWJ		4/15/2012				
CHFD						
APPRD						
MFC						
CLA					DWG NO.	E2
			MATERIAL: Inconel 718		SCALE: 1:1	SHEET 1 OF 1



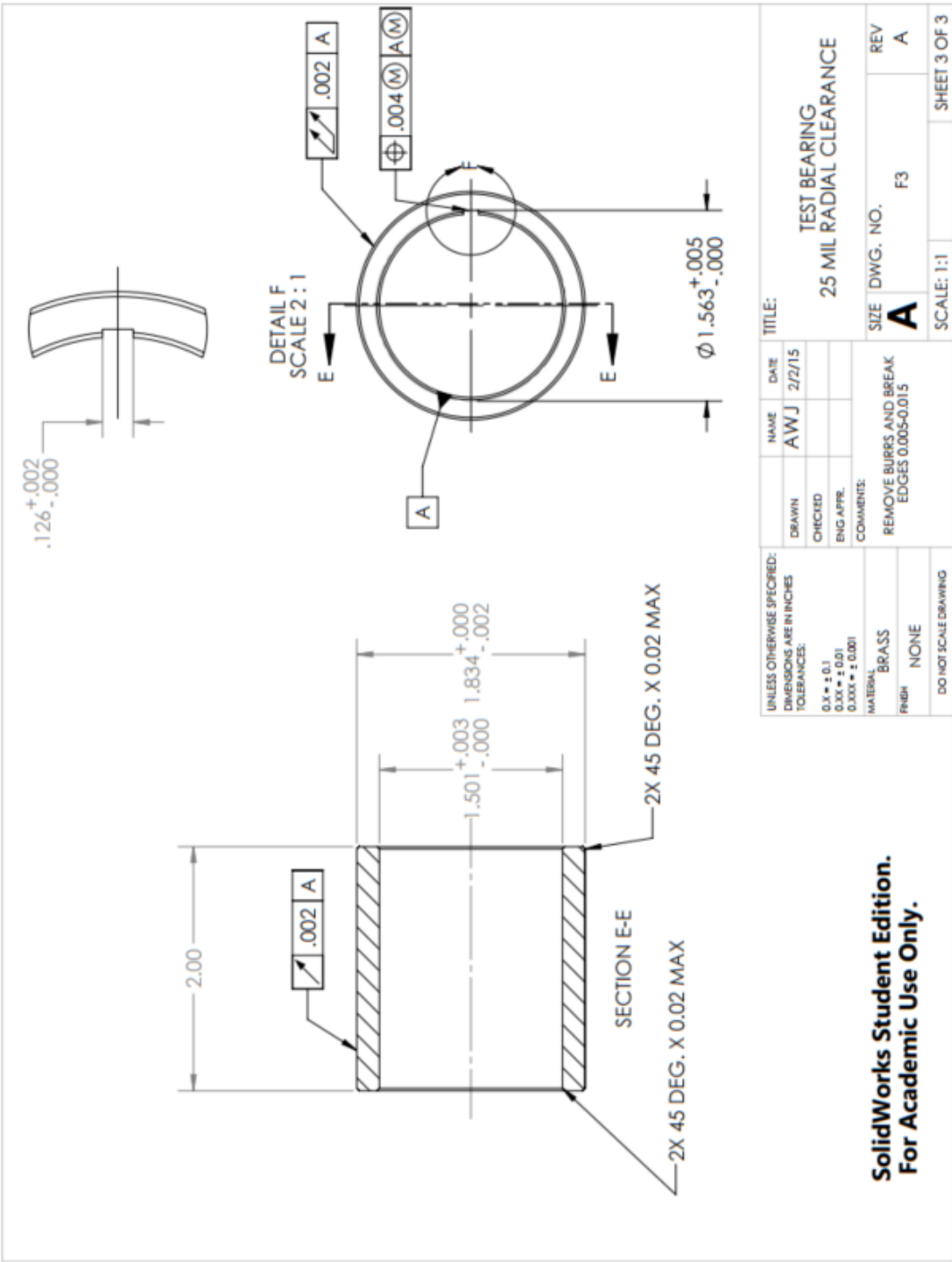
DIMENSIONS ARE IN INCHES TOLERANCES: 0.1 = ± 0.1 0.01 = ± 0.01 0.001 = ± 0.001			FINISH		CORNER AND BREAK SHARP EDGES		DO NOT SCALE DRAWING		REVISION	
DRAWN AWJ			SIGNATURE		DATE 4/12/2013		JOB		IMBALANCE DISK	
CHK'D										
APP'VD										
MFG										
QA					MATERIAL: STAINLESS STEEL		DWG NO.		E3	
					WEIGHT:		SCALE: 2:1		SHEET 1 OF 3	

Assembly F: Imitation Brass Bearings

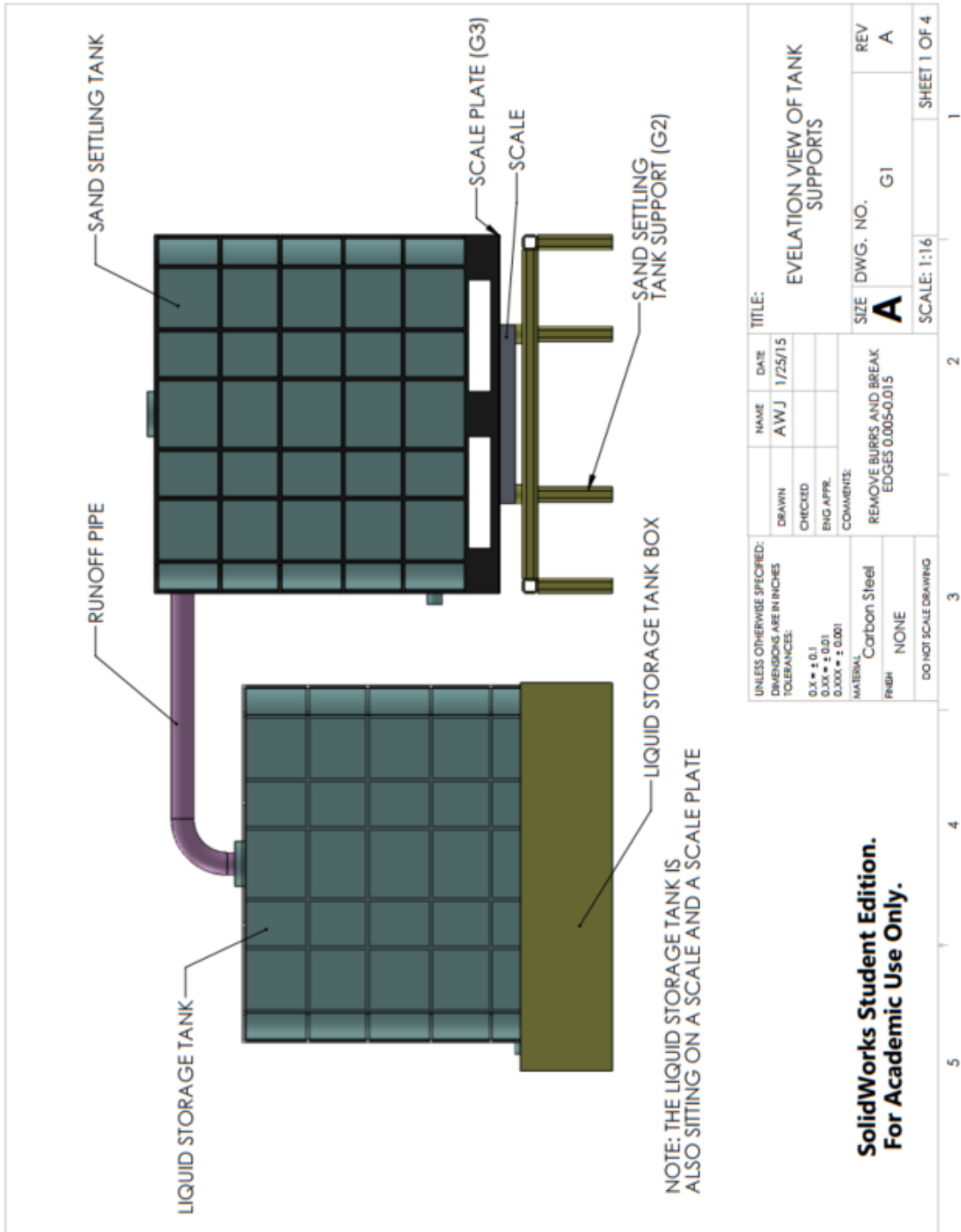


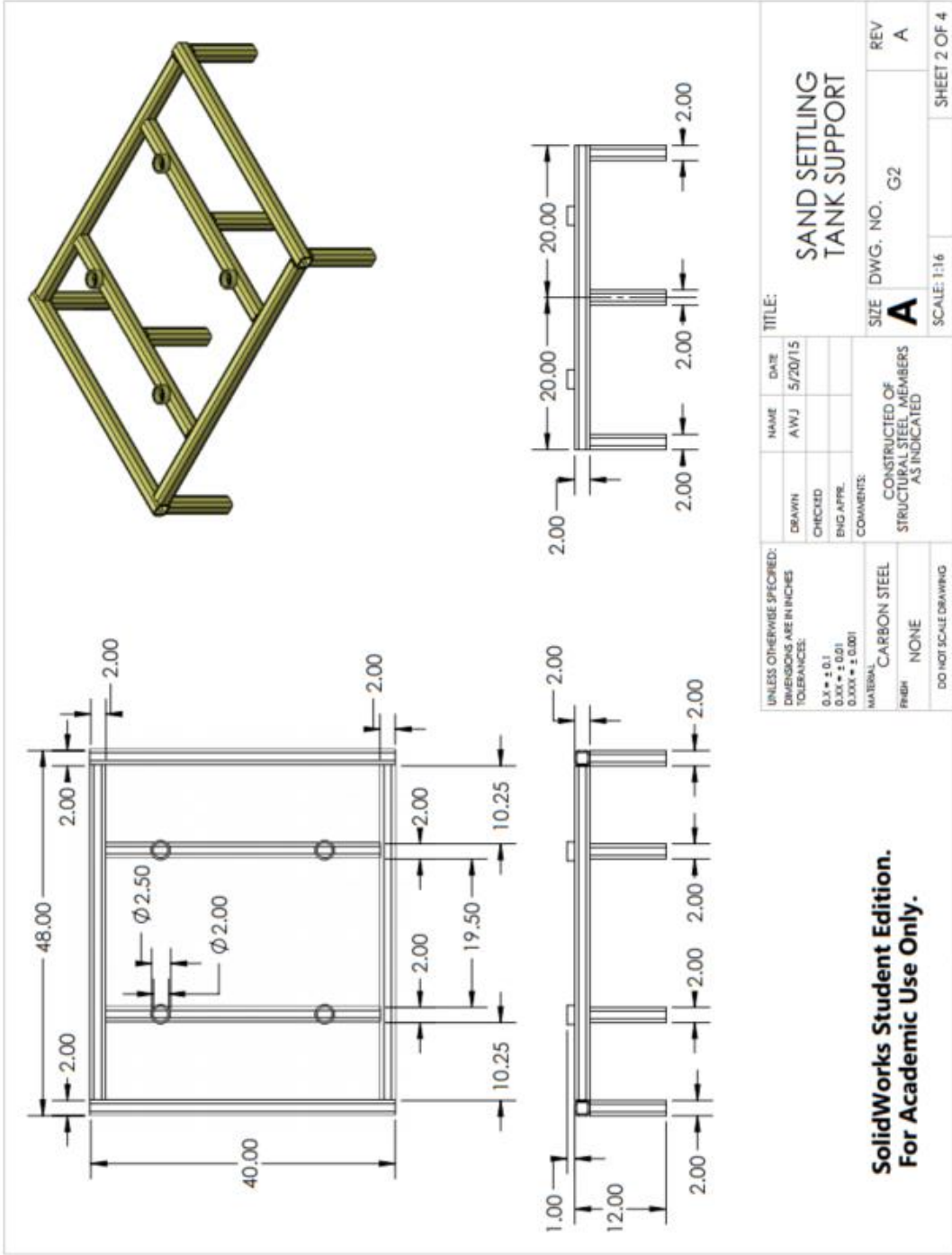


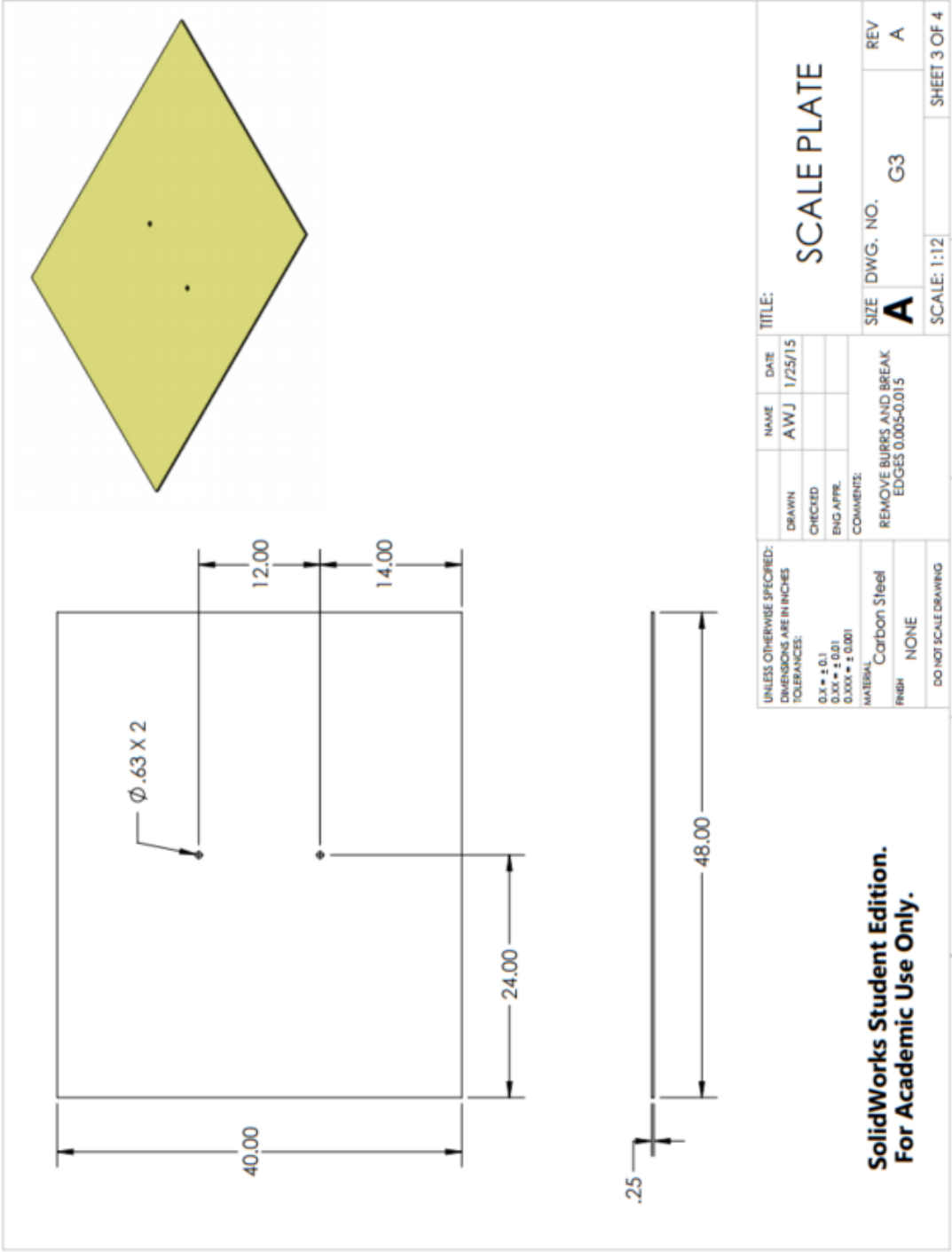
**SolidWorks Student Edition.
For Academic Use Only.**



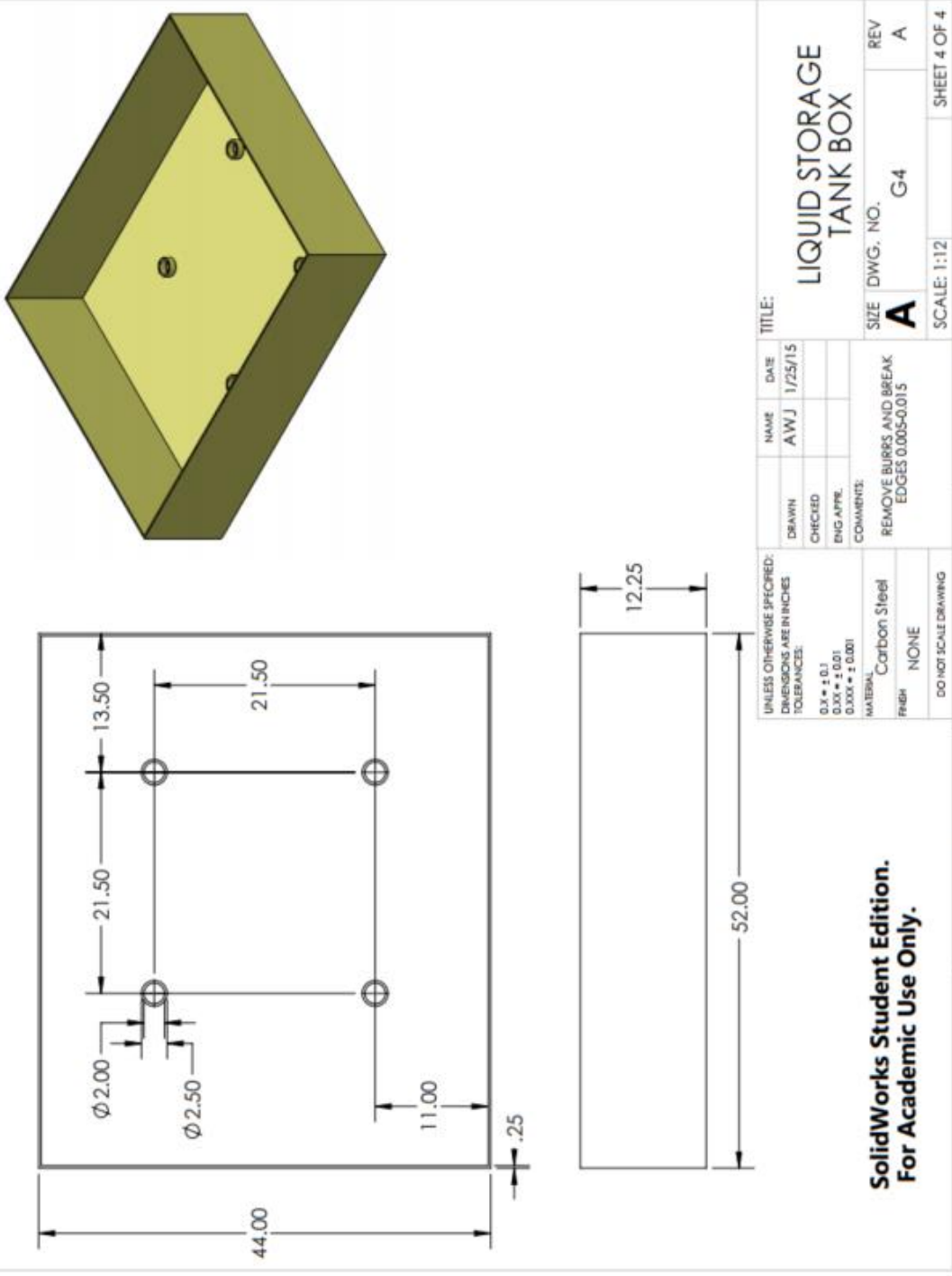
Assembly G: Tank Supports







**SolidWorks Student Edition.
For Academic Use Only.**



APPENDIX B

ALL 6 MIL RADIAL CLEARANCE DATA

Imbalance Disk Orbit, 600 RPM, 6 mil Bearing Clearance

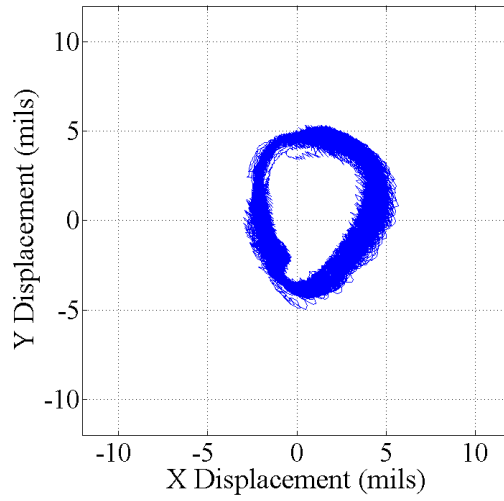


Figure 58: 6 mil radial clearance orbit at 600 RPM

Imbalance Disk Orbit, 1200 RPM, 6 mil Bearing Clearance

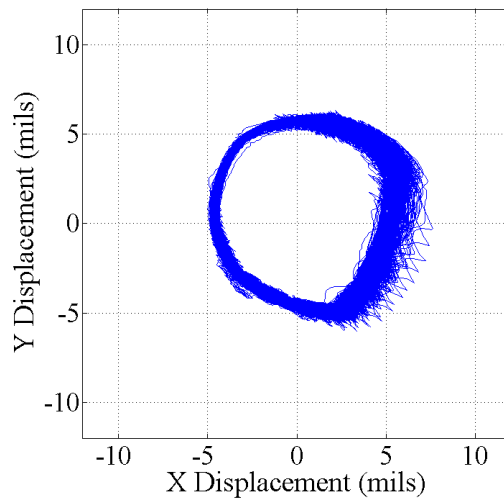


Figure 59: 6 mil radial clearance orbit at 1200 RPM

Imbalance Disk Orbit, 1800 RPM, 6 mil Bearing Clearance

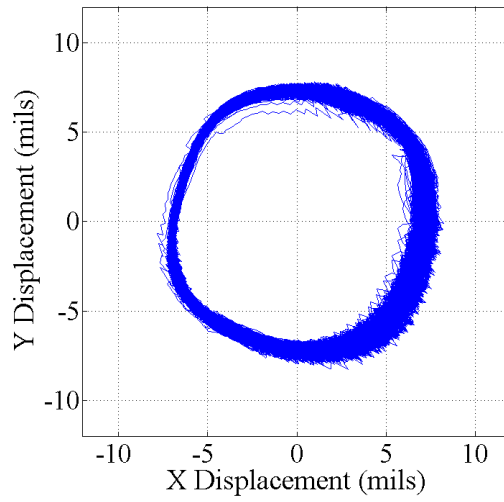


Figure 60: 6 mil radial clearance orbit at 1800 RPM

Imbalance Disk Orbit, 2400 RPM, 6 mil Bearing Clearance

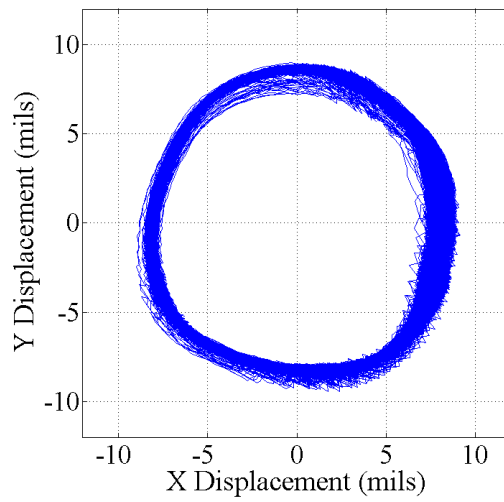


Figure 61: 6 mil radial clearance orbit at 2400 RPM

Imbalance Disk Orbit, 3000 RPM, 6 mil Bearing Clearance

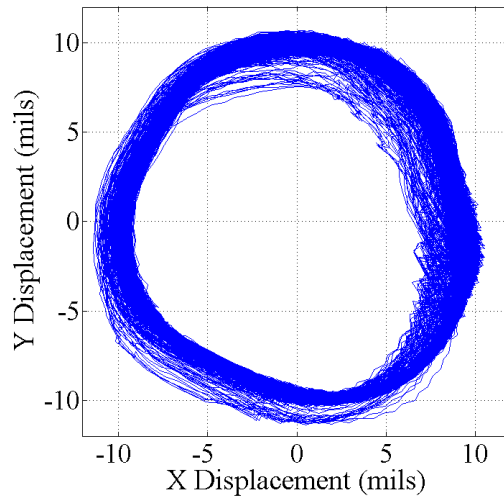


Figure 62: 6 mil radial clearance orbit at 3000 RPM

Imbalance Disk Orbit, 3600 RPM, 6 mil Bearing Clearance

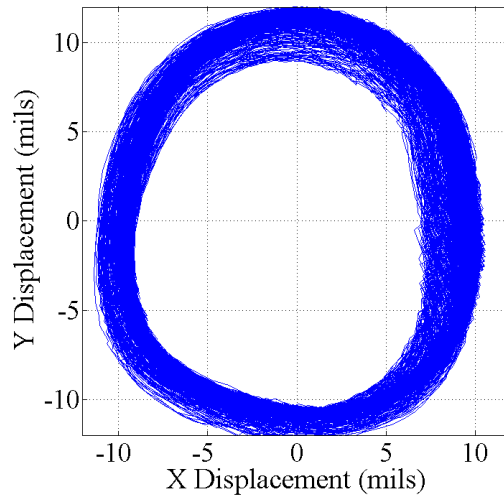


Figure 63: 6 mil radial clearance orbit at 3600 RPM

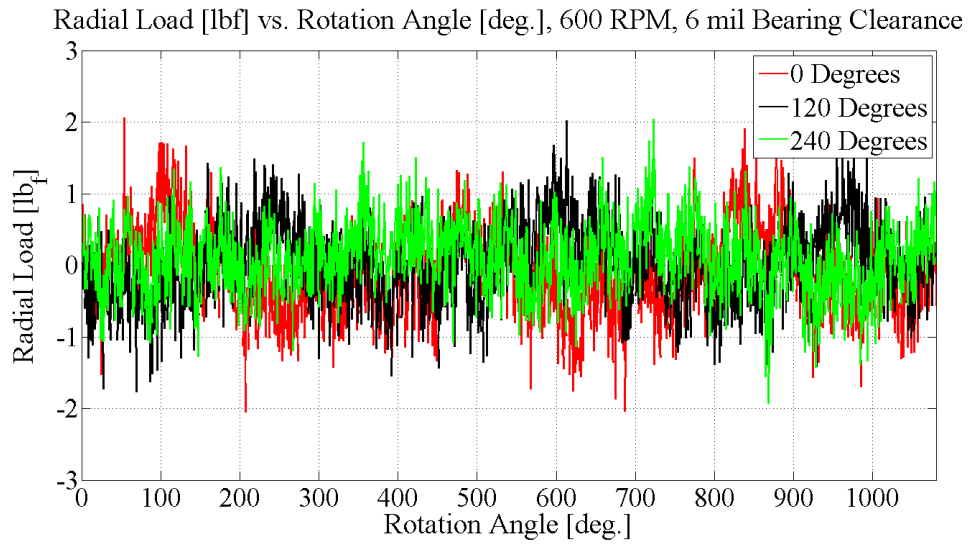


Figure 64: 6 mil radial clearance radial loads at 600 RPM

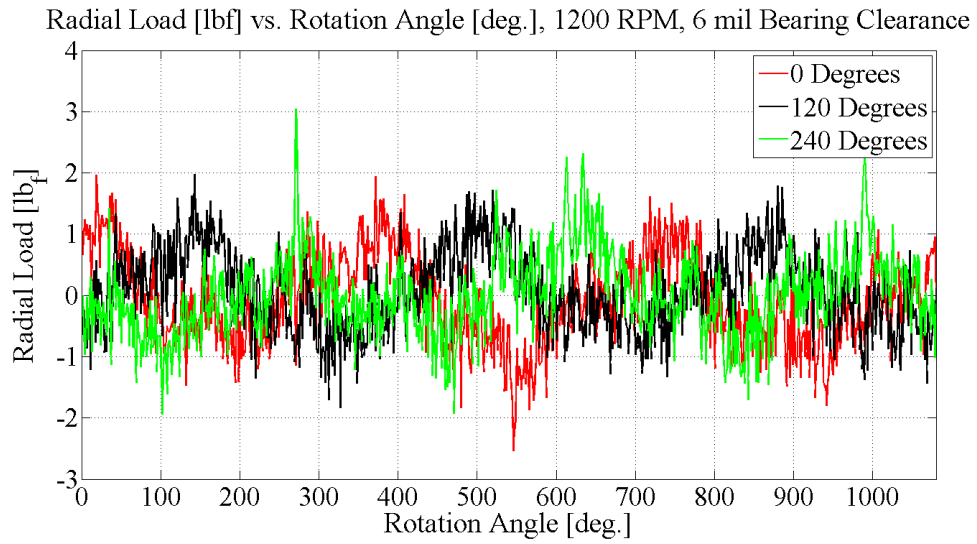


Figure 65: 6 mil radial clearance radial loads at 1200 RPM

Radial Load [lbf] vs. Rotation Angle [deg.], 1800 RPM, 6 mil Bearing Clearance

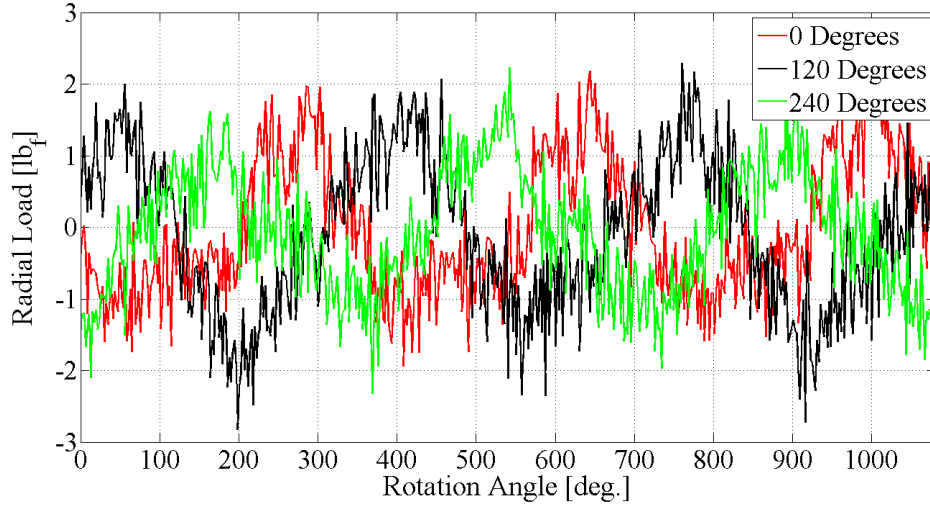


Figure 66: 6 mil radial clearance radial loads at 1800 RPM

Radial Load [lbf] vs. Rotation Angle [deg.], 2400 RPM, 6 mil Bearing Clearance

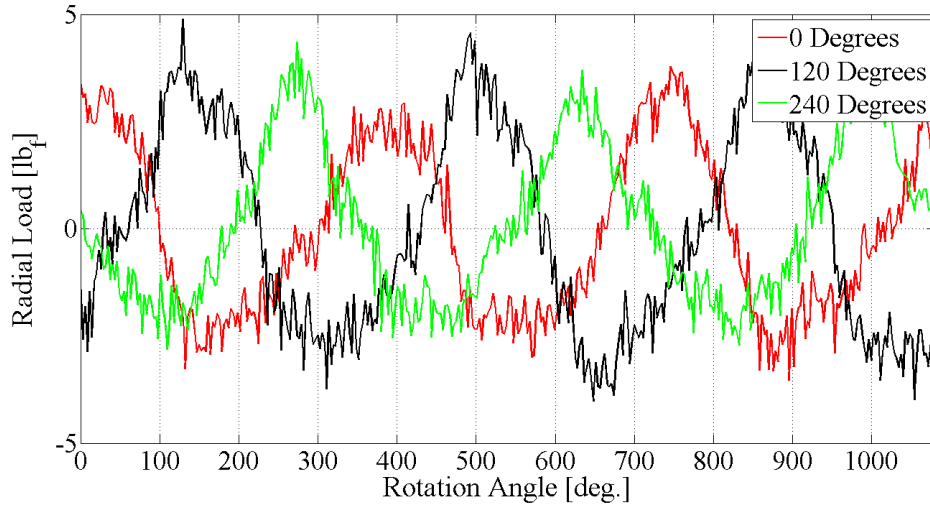


Figure 67: 6 mil radial clearance radial loads at 2400 RPM

Radial Load [lbf] vs. Rotation Angle [deg.], 3000 RPM, 6 mil Bearing Clearance

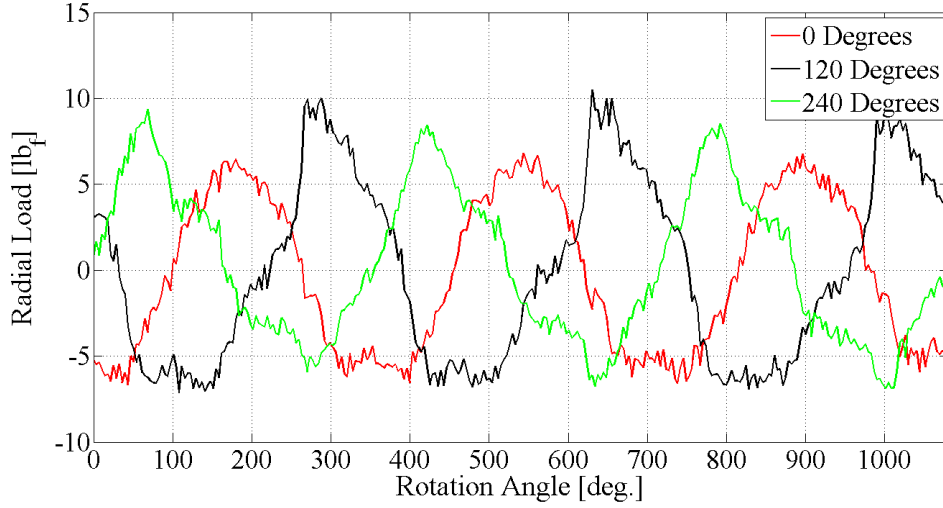


Figure 68: 6 mil radial clearance radial loads at 3000 RPM

Radial Load [lbf] vs. Rotation Angle [deg.], 3600 RPM, 6 mil Bearing Clearance

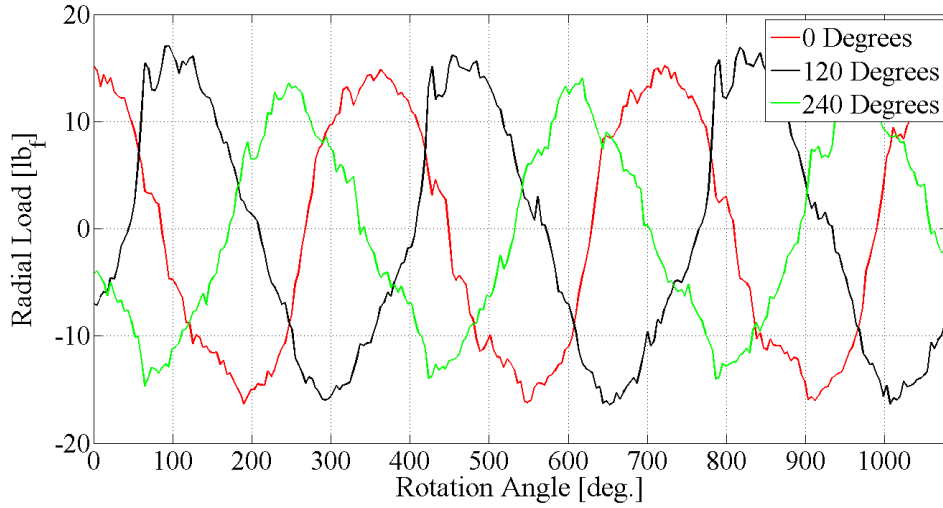


Figure 69: 6 mil radial clearance radial loads at 3600 RPM

Dynamic Pressure [psi] vs. Rotation Angle [deg.], 600 RPM, 6 mil Bearing Clearance

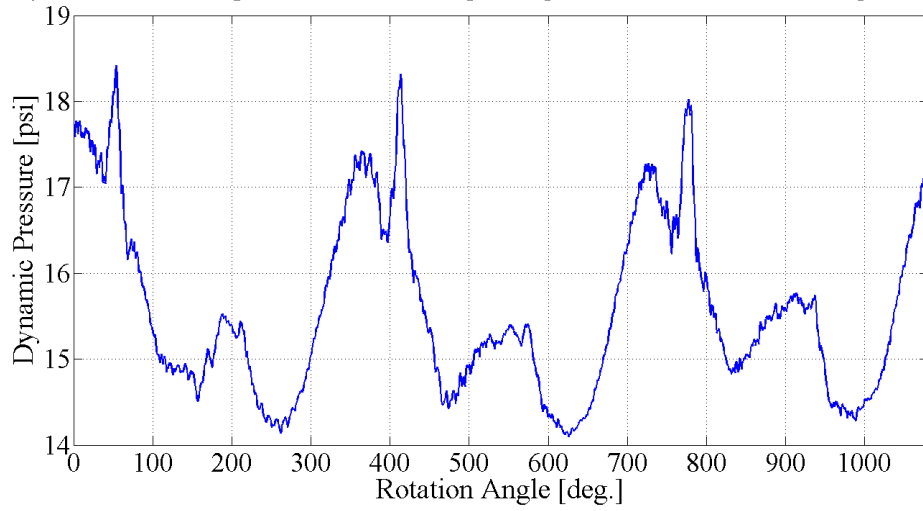


Figure 70: 6 mil radial clearance annulus pressure at 600 RPM

Dynamic Pressure [psi] vs. Rotation Angle [deg.], 1200 RPM, 6 mil Bearing Clearance

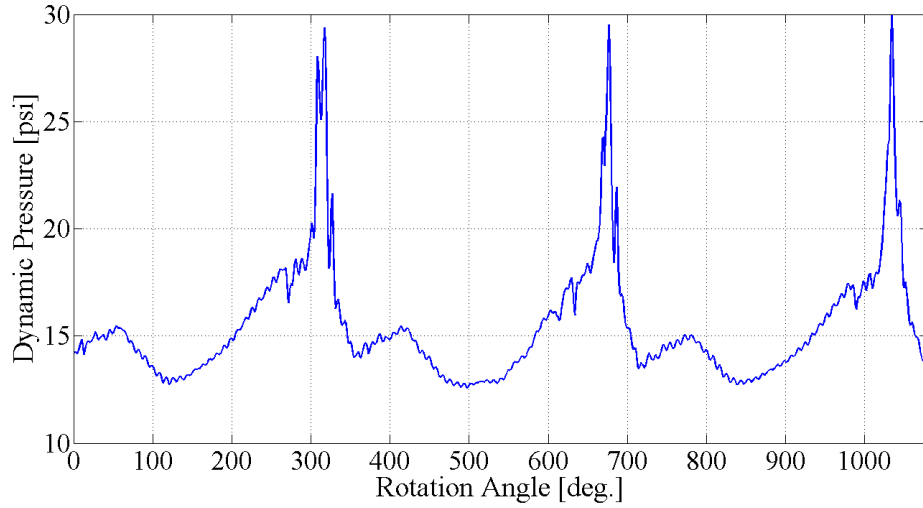


Figure 71: 6 mil radial clearance annulus pressure at 1200 RPM

Dynamic Pressure [psi] vs. Rotation Angle [deg.], 1800 RPM, 6 mil Bearing Clearance

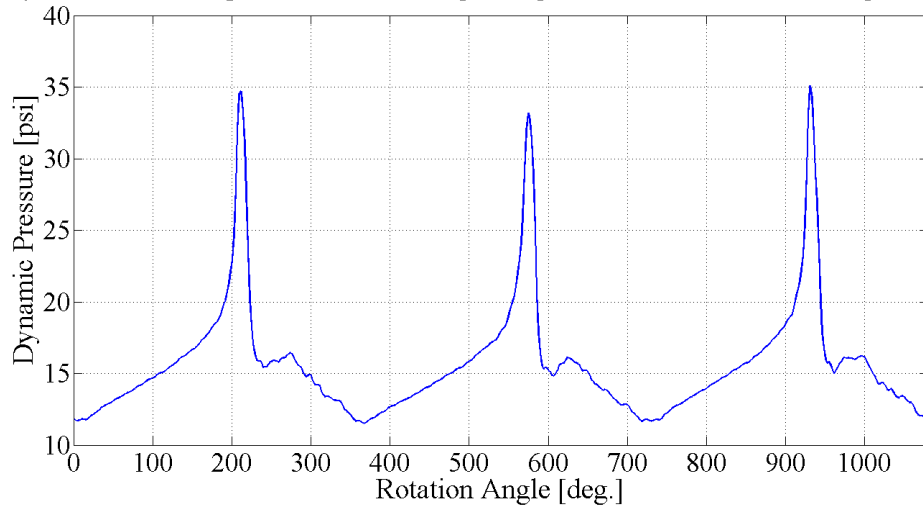


Figure 72: 6 mil radial clearance annulus pressure at 1800 RPM

Dynamic Pressure [psi] vs. Rotation Angle [deg.], 2400 RPM, 6 mil Bearing Clearance

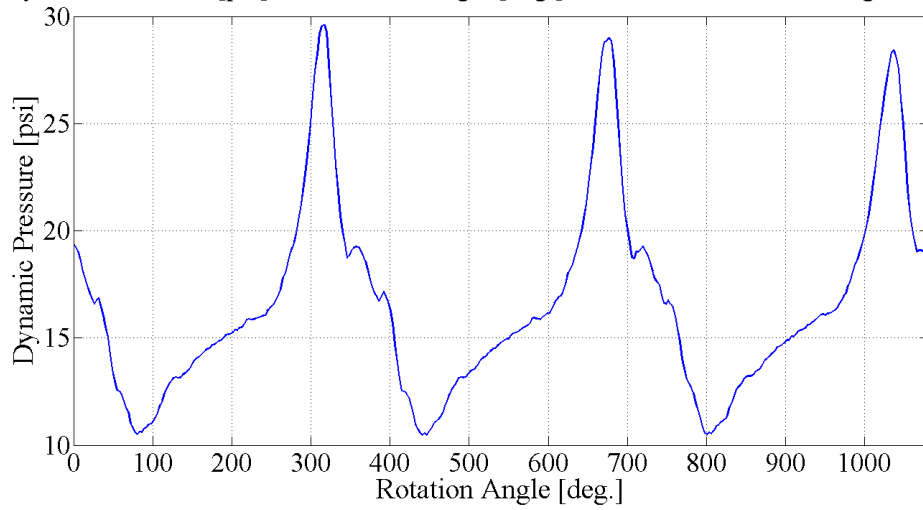


Figure 73: 6 mil radial clearance annulus pressure at 2400 RPM

Dynamic Pressure [psi] vs. Rotation Angle [deg.], 3000 RPM, 6 mil Bearing Clearance

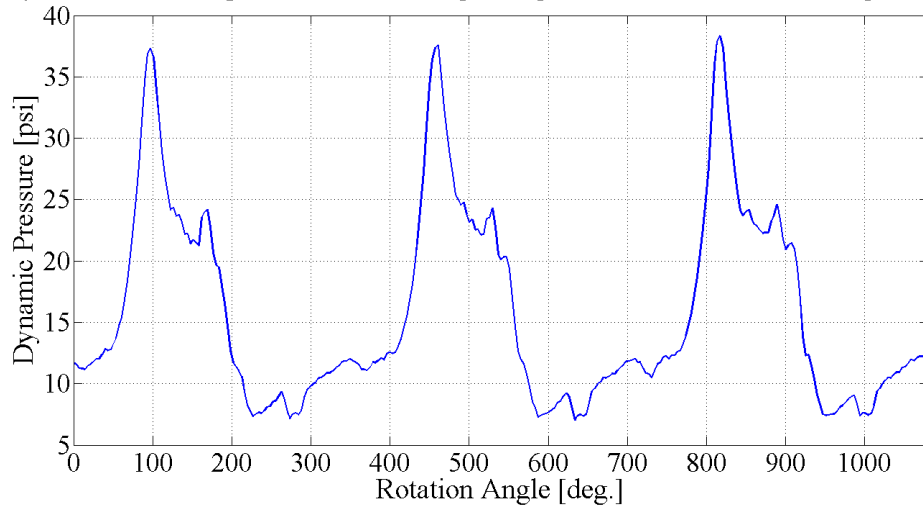


Figure 74: 6 mil radial clearance annulus pressure at 3000 RPM

Dynamic Pressure [psi] vs. Rotation Angle [deg.], 3600 RPM, 6 mil Bearing Clearance

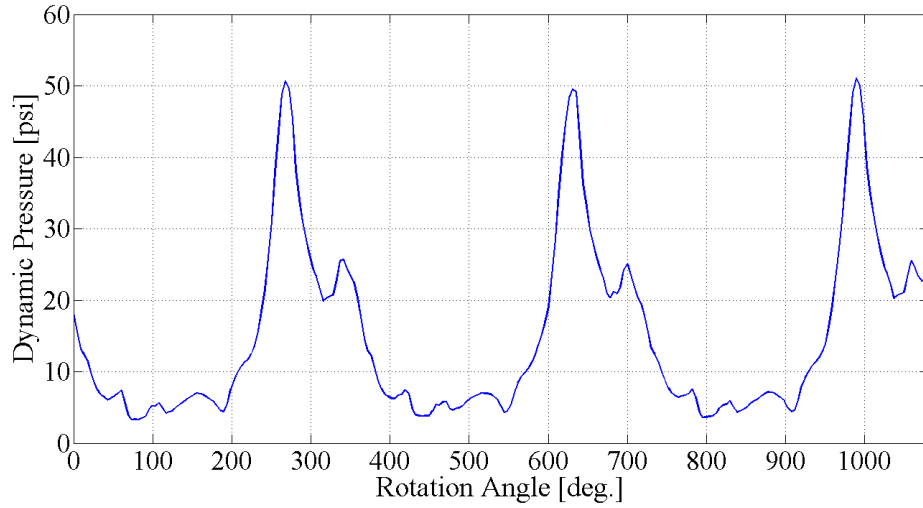


Figure 75: 6 mil radial clearance annulus pressure at 3600 RPM

Imbalance Disk Orbit, 6 mil Bearing Clearance

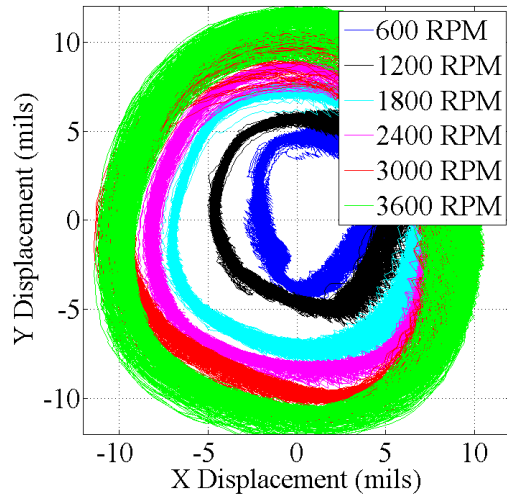


Figure 76: 6 mil orbit comparison as a function of speed

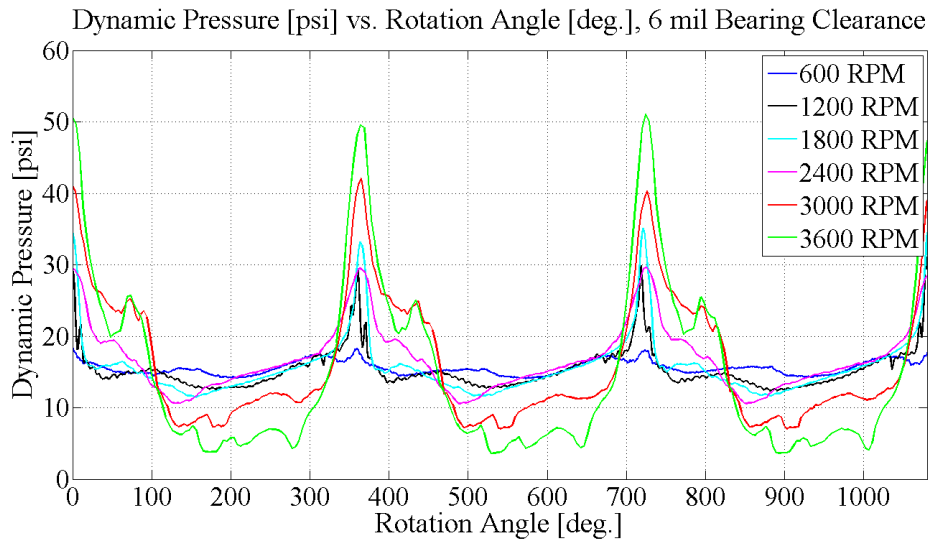


Figure 77: 6 mil radial clearance pressure comparison as a function of angle

600 RPM, 6 mil Bearing Clearance Annulus Pressure Compared to Sommerfeld Prediction

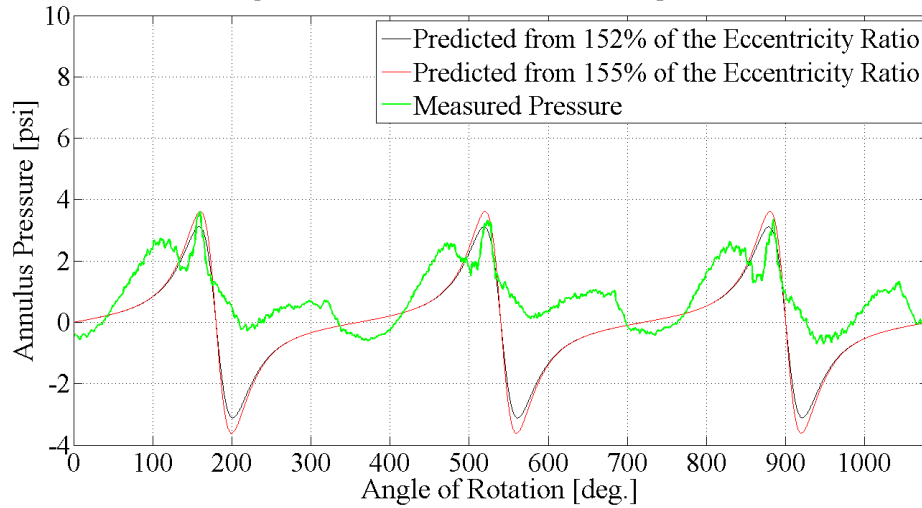


Figure 78: 6 mil predicted compared to measured pressure at 600 RPM

1200 RPM, 6 mil Bearing Clearance Annulus Pressure Compared to Sommerfeld Prediction

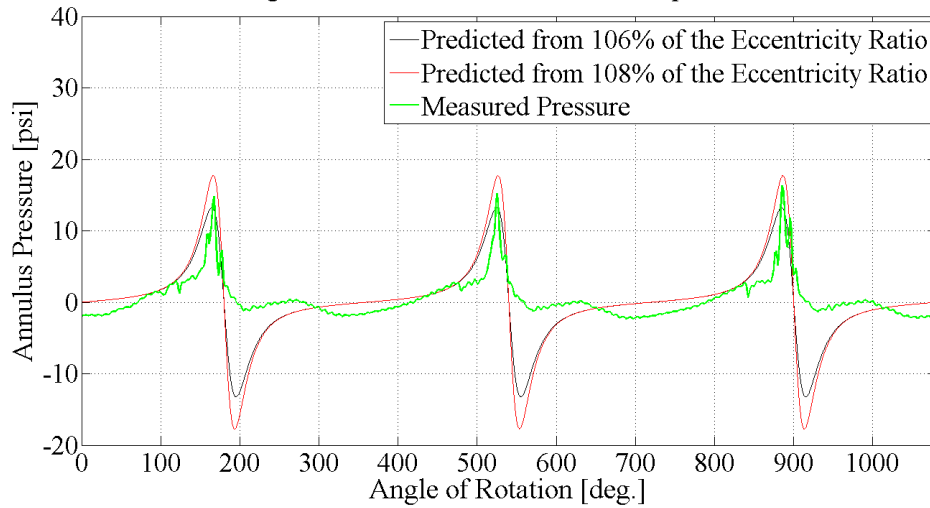


Figure 79: 6 mil predicted compared to measured pressure at 1200 RPM

1800 RPM, 6 mil Bearing Clearance Annulus Pressure Compared to Sommerfeld Prediction

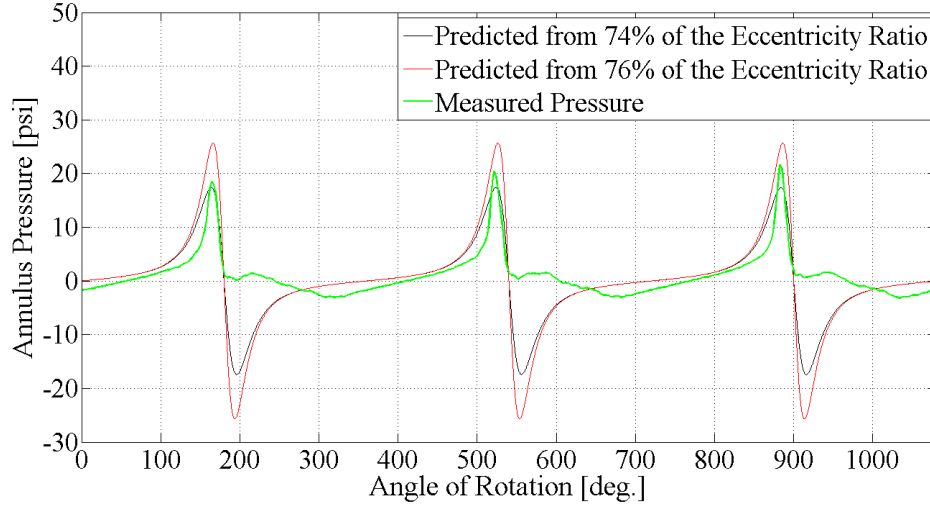


Figure 80: 6 mil predicted compared to measured pressure at 1800 RPM

2400 RPM, 6 mil Bearing Clearance Annulus Pressure Compared to Sommerfeld Prediction

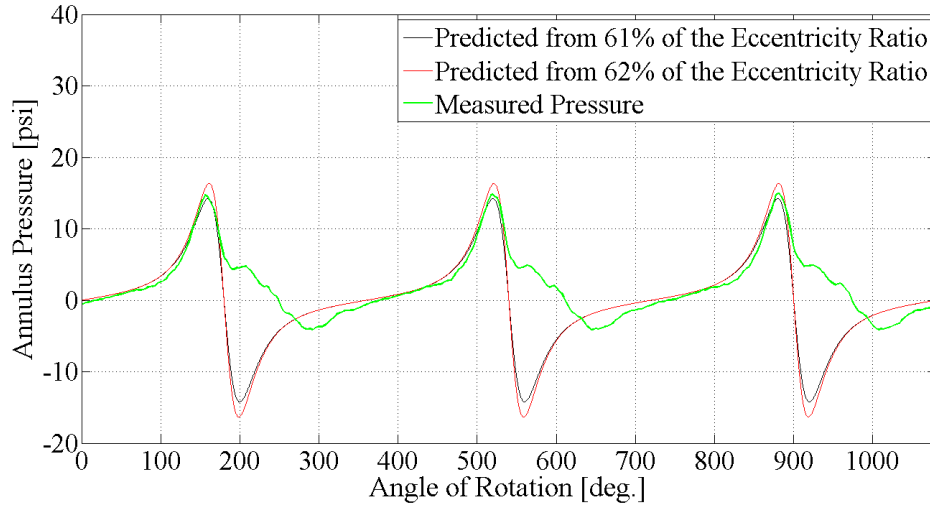


Figure 81: 6 mil predicted compared to measured pressure at 2400 RPM

3000 RPM, 6 mil Bearing Clearance Annulus Pressure Compared to Sommerfeld Prediction

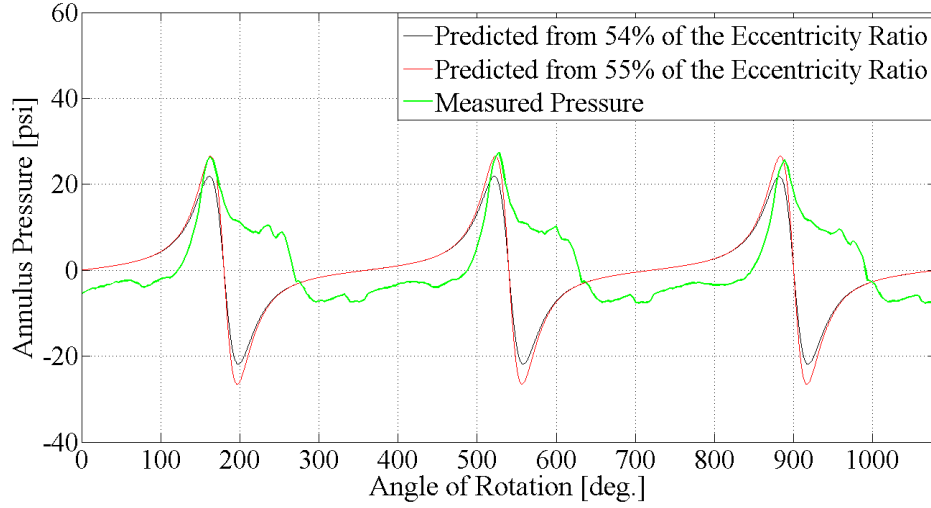


Figure 82: 6 mil predicted compared to measured pressure at 3000 RPM

3600 RPM, 6 mil Bearing Clearance Annulus Pressure Compared to Sommerfeld Prediction

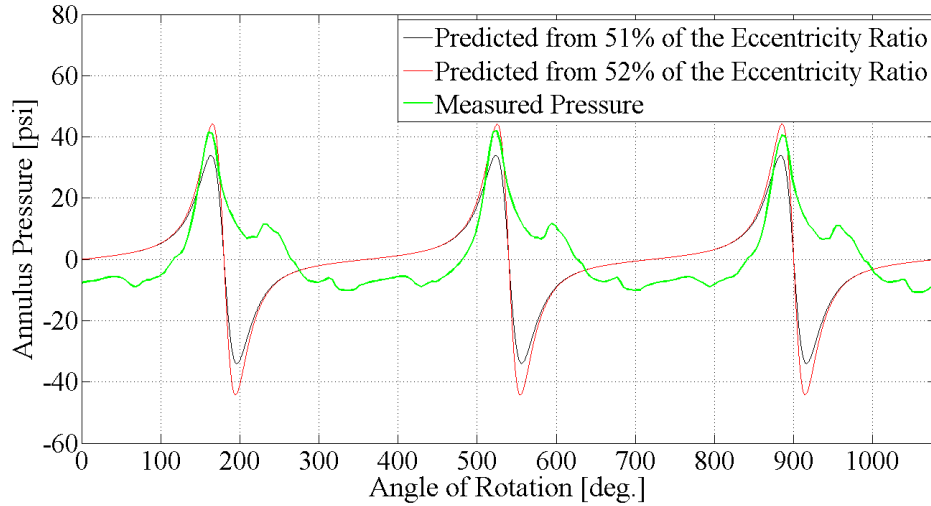


Figure 83: 6 mil predicted compared to measured pressure at 3600 RPM

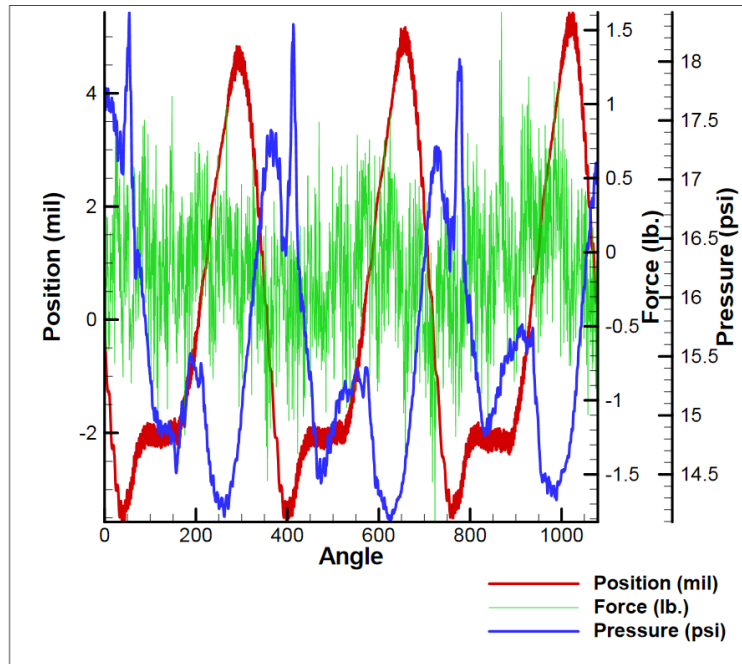


Figure 84: 6 mil position, force, and pressure comparison at 600 RPM

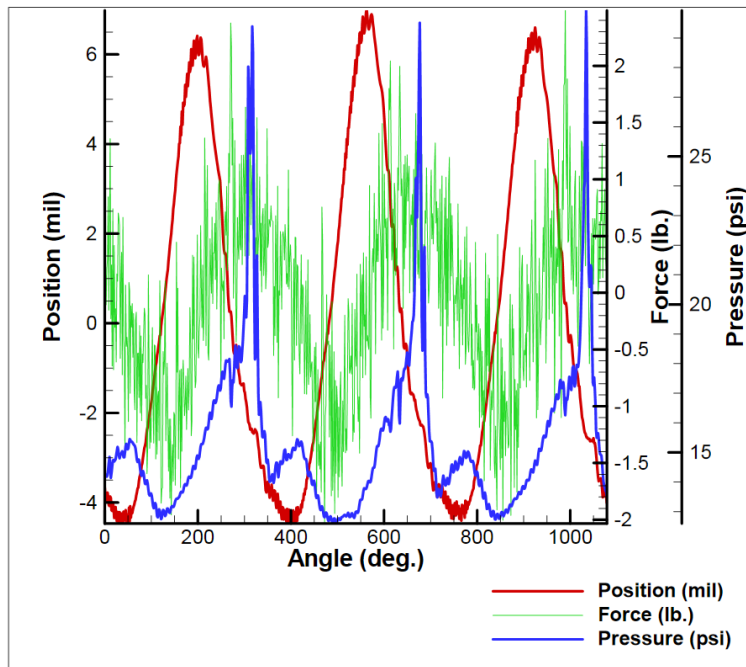


Figure 85: 6 mil position, force, and pressure comparison at 1200 RPM

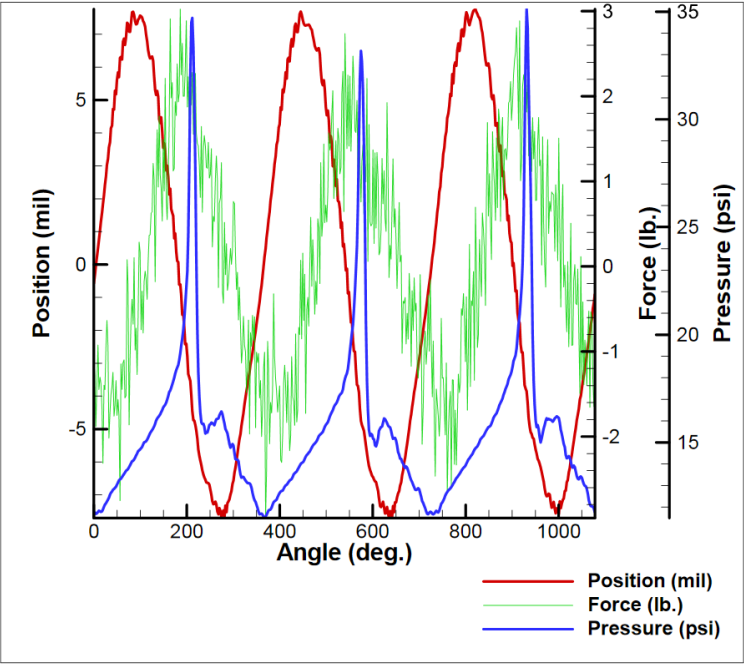


Figure 86: 6 mil position, force, and pressure comparison at 1800 RPM

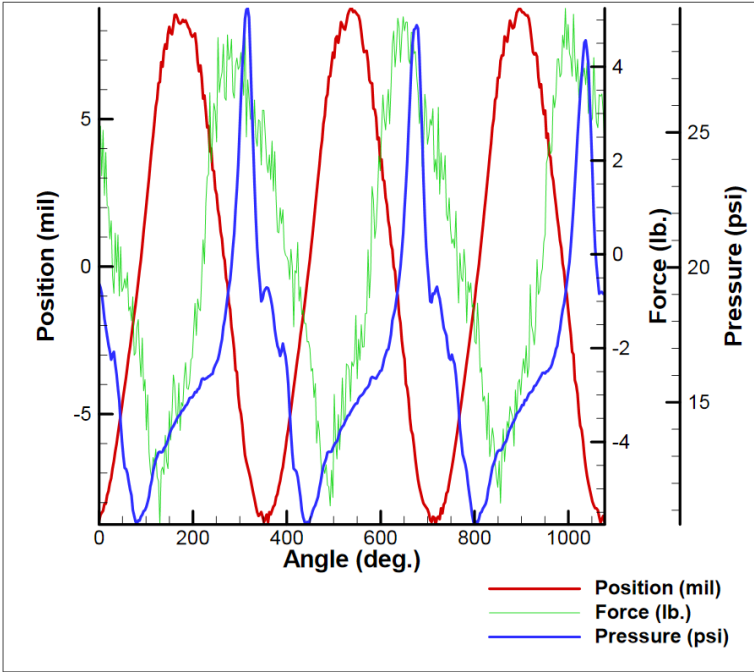


Figure 87: 6 mil position, force, and pressure comparison at 2400 RPM

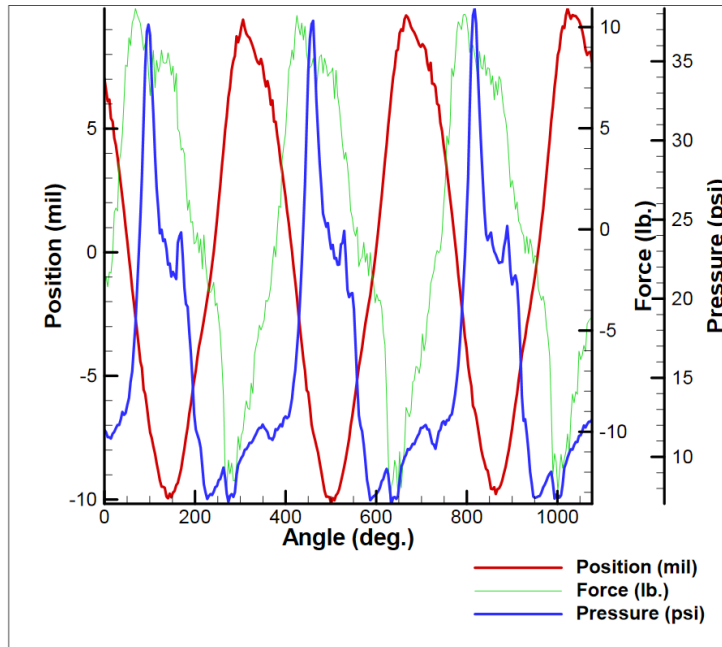


Figure 88: 6 mil position, force, and pressure comparison at 3000 RPM

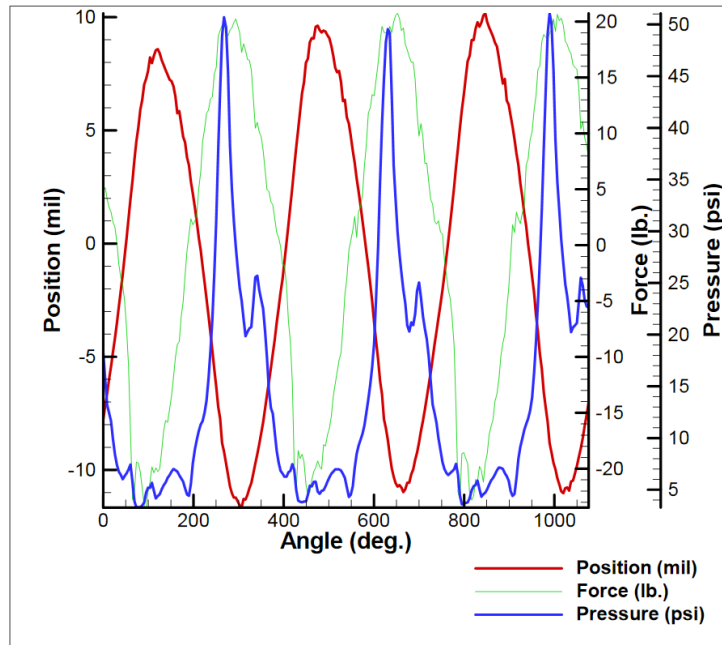


Figure 89: 6 mil position, force, and pressure comparison at 3600 RPM

APPENDIX C

ALL 12.5 MIL RADIAL CLEARANCE DATA

Imbalance Disk Orbit, 600 RPM, 12.5 mil Bearing Clearance

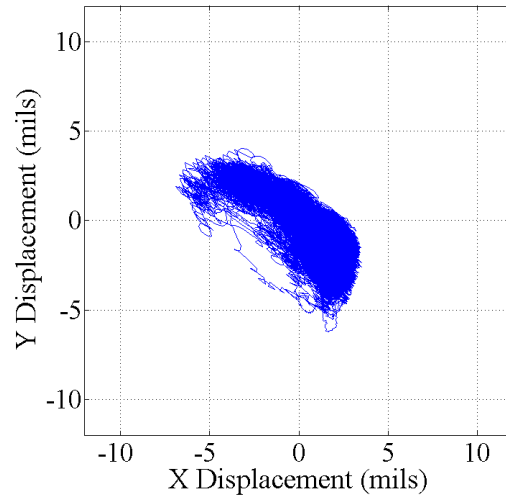


Figure 90: 12.5 mil radial clearance orbit at 600 RPM

Imbalance Disk Orbit, 1200 RPM, 12.5 mil Bearing Clearance

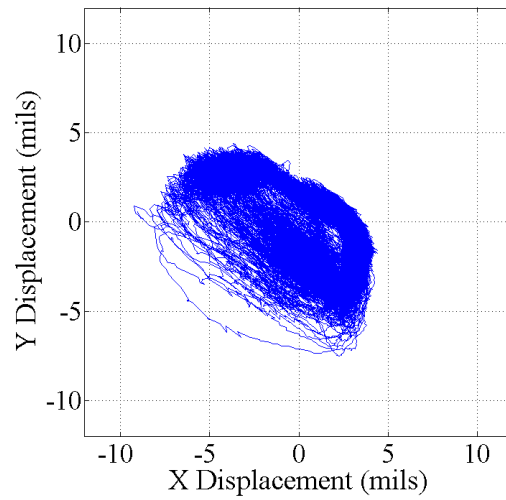


Figure 91: 12.5 mil radial clearance orbit at 1200 RPM

Imbalance Disk Orbit, 1800 RPM, 12.5 mil Bearing Clearance

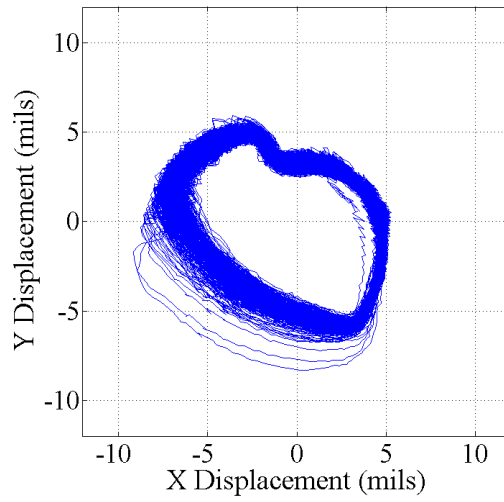


Figure 92: 12.5 mil radial clearance orbit at 1800 RPM

Imbalance Disk Orbit, 2400 RPM, 12.5 mil Bearing Clearance

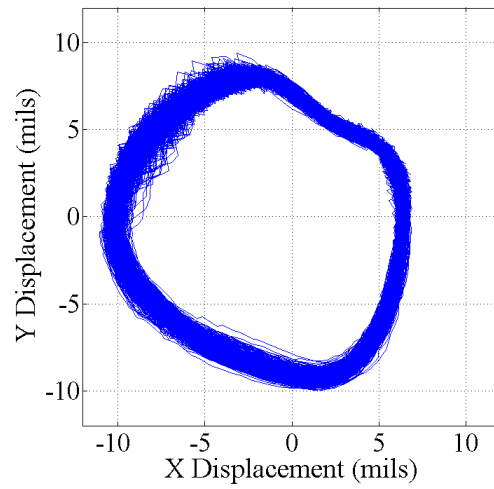


Figure 93: 12.5 mil radial clearance orbit at 2400 RPM

Imbalance Disk Orbit, 3000 RPM, 12.5 mil Bearing Clearance

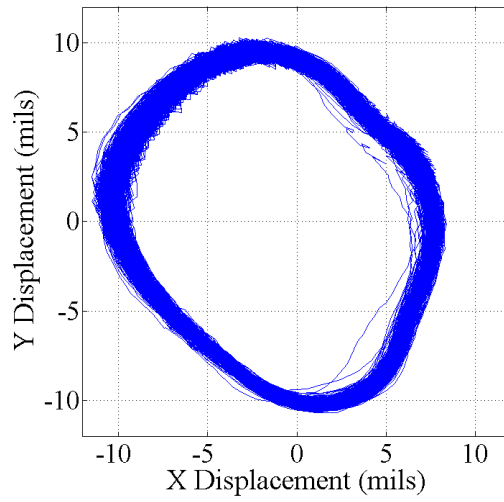


Figure 94: 12.5 mil radial clearance orbit at 3000 RPM

Imbalance Disk Orbit, 3600 RPM, 12.5 mil Bearing Clearance

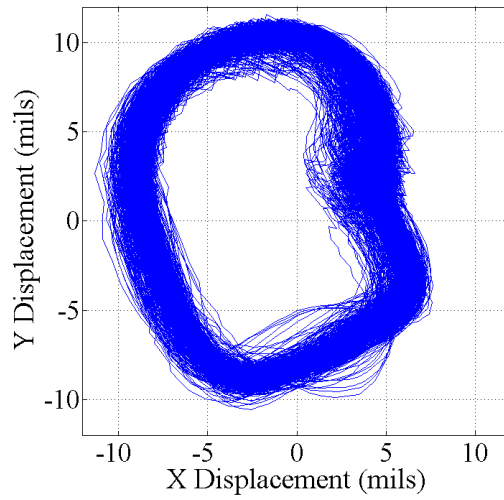


Figure 95: 12.5 mil radial clearance orbit at 3600 RPM

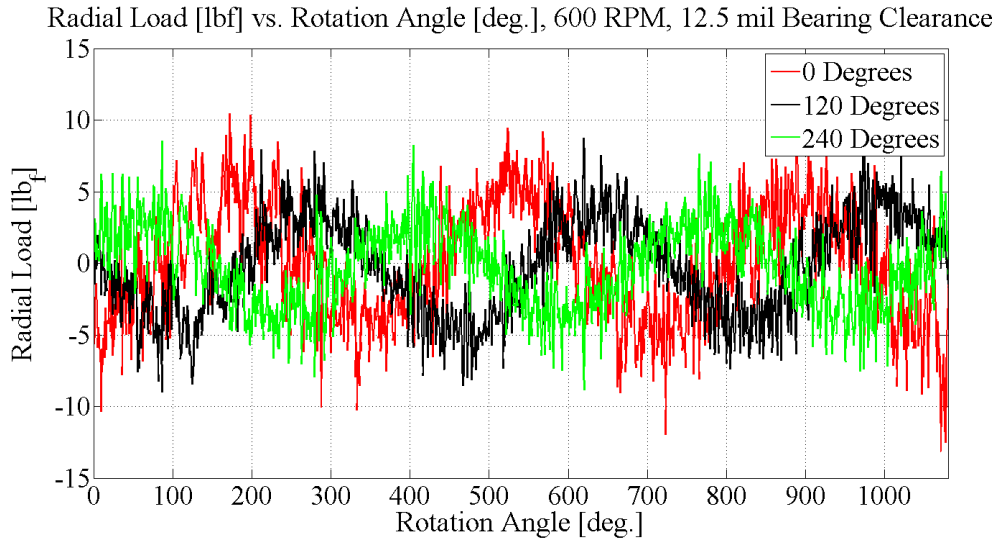


Figure 96: 12.5 mil radial clearance radial loads at 600 RPM

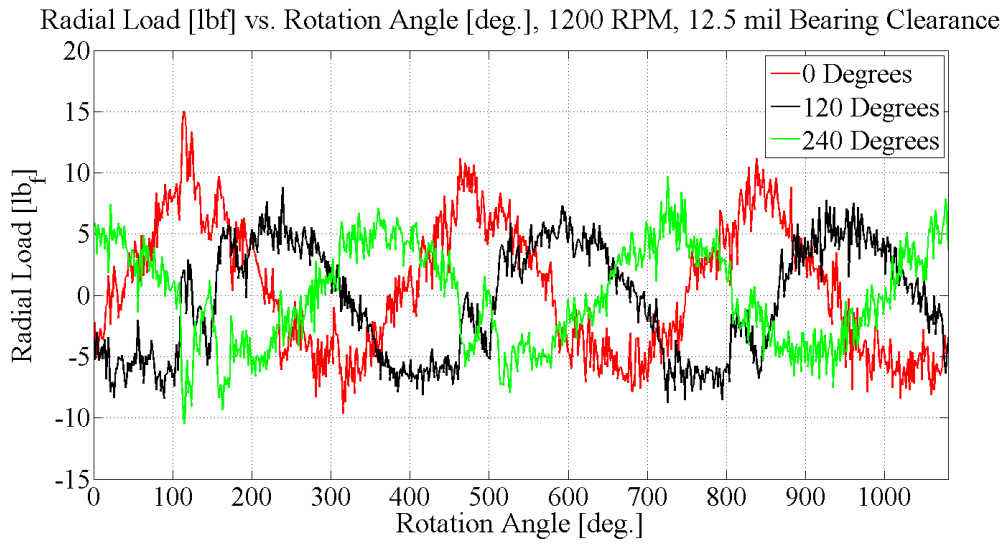


Figure 97: 12.5 mil radial clearance radial loads at 1200 RPM

Radial Load [lbf] vs. Rotation Angle [deg.], 1800 RPM, 12.5 mil Bearing Clearance

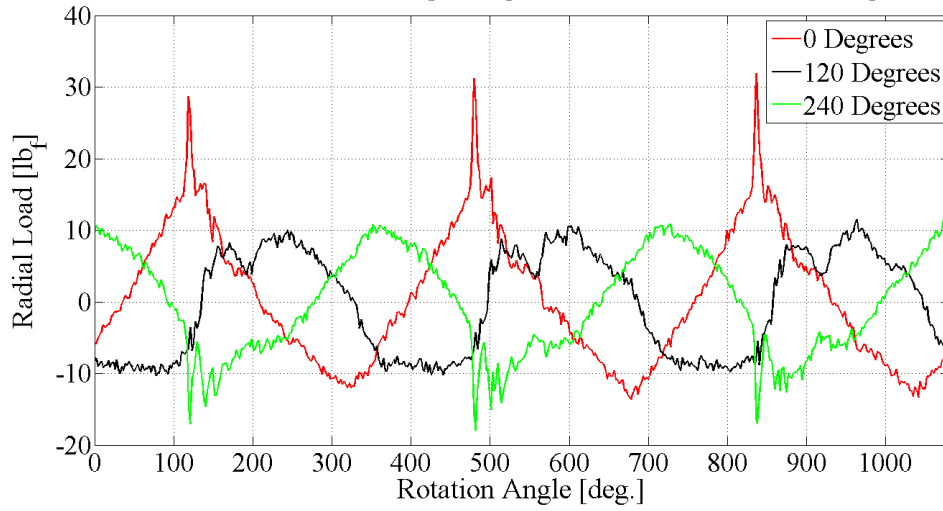


Figure 98: 12.5 mil radial clearance radial loads at 1800 RPM

Radial Load [lbf] vs. Rotation Angle [deg.], 2400 RPM, 12.5 mil Bearing Clearance

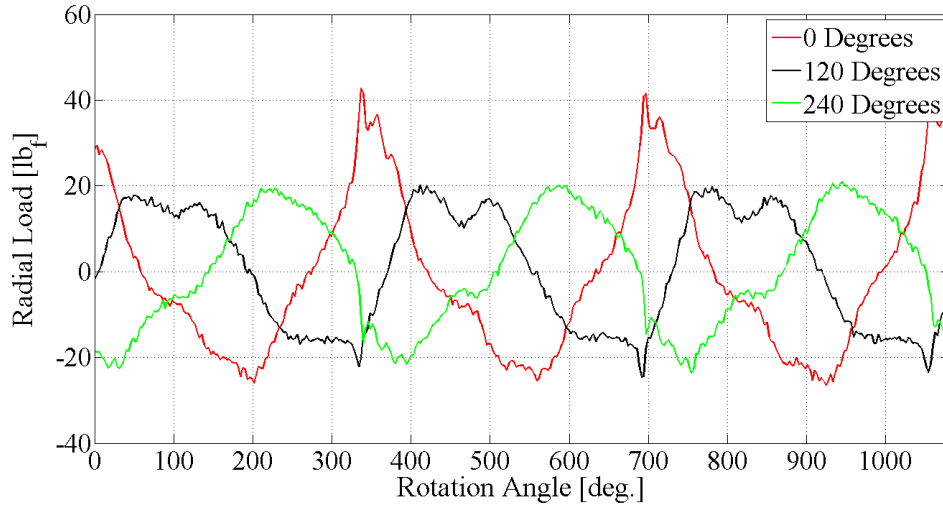


Figure 99: 12.5 mil radial clearance radial loads at 2400 RPM

Radial Load [lbf] vs. Rotation Angle [deg.], 3000 RPM, 12.5 mil Bearing Clearance

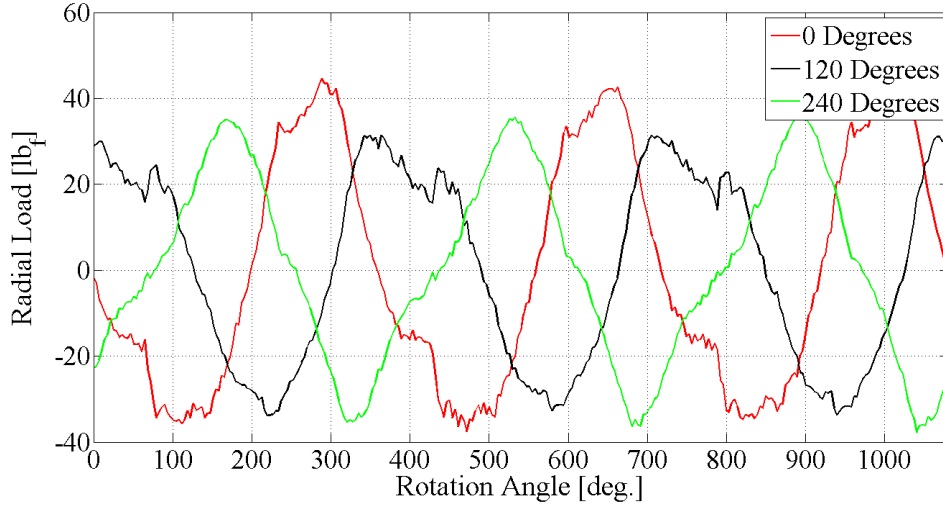


Figure 100: 12.5 mil radial clearance radial loads at 3000 RPM

Radial Load [lbf] vs. Rotation Angle [deg.], 3600 RPM, 12.5 mil Bearing Clearance

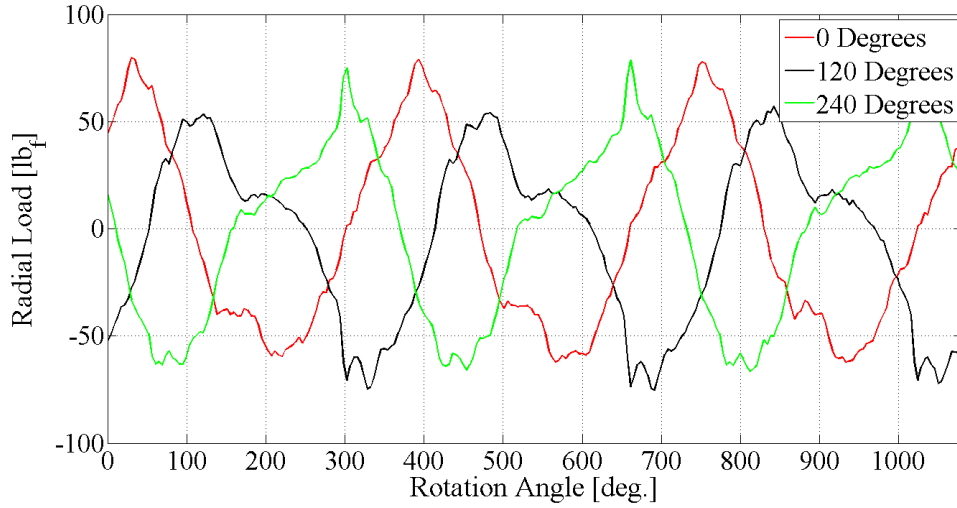


Figure 101: 12.5 mil radial clearance radial loads at 3600 RPM

Dynamic Pressure [psi] vs. Rotation Angle [deg.], 600 RPM, 12.5 mil Bearing Clearance

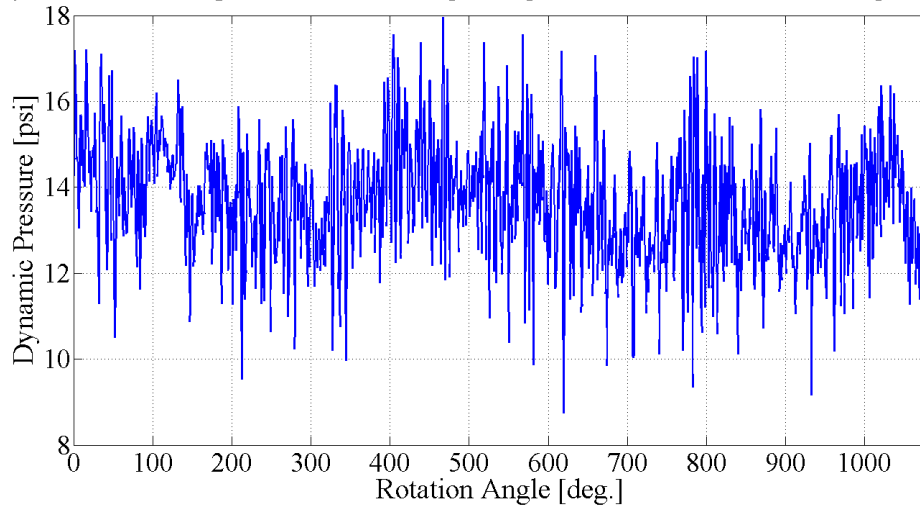


Figure 102: 12.5 mil radial clearance annulus pressure at 600 RPM

Dynamic Pressure [psi] vs. Rotation Angle [deg.], 1200 RPM, 12.5 mil Bearing Clearance

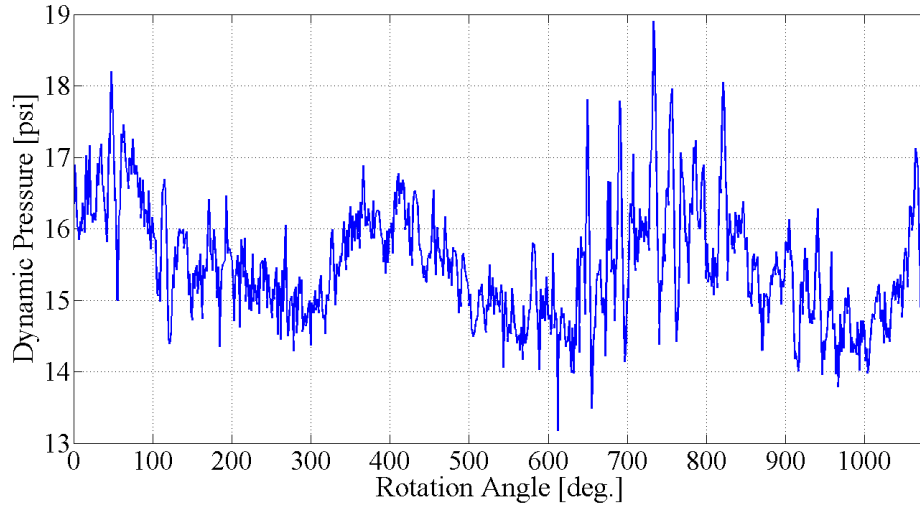


Figure 103: 12.5 mil radial clearance annulus pressure at 1200 RPM

Dynamic Pressure [psi] vs. Rotation Angle [deg.], 1800 RPM, 12.5 mil Bearing Clearance

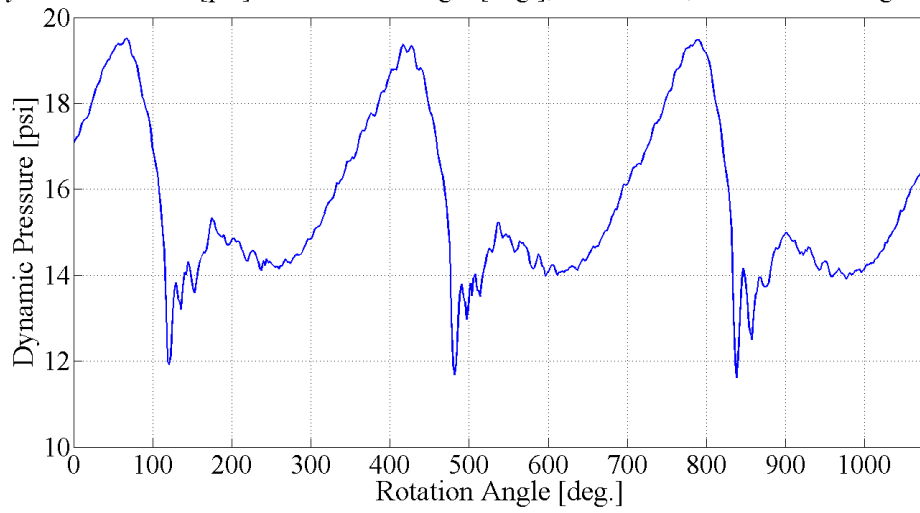


Figure 104: 12.5 mil radial clearance annulus pressure at 1800 RPM

Dynamic Pressure [psi] vs. Rotation Angle [deg.], 2400 RPM, 12.5 mil Bearing Clearance

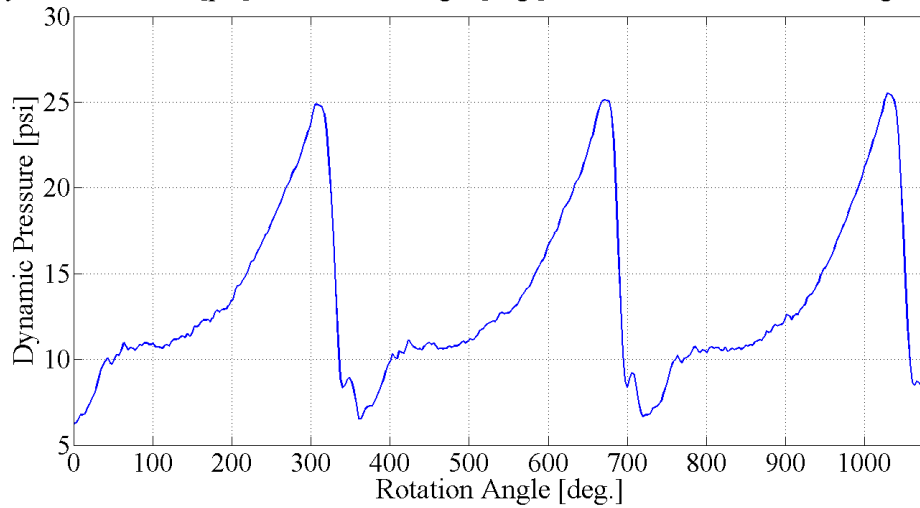


Figure 105: 12.5 mil radial clearance annulus pressure at 2400 RPM

Dynamic Pressure [psi] vs. Rotation Angle [deg.], 3000 RPM, 12.5 mil Bearing Clearance

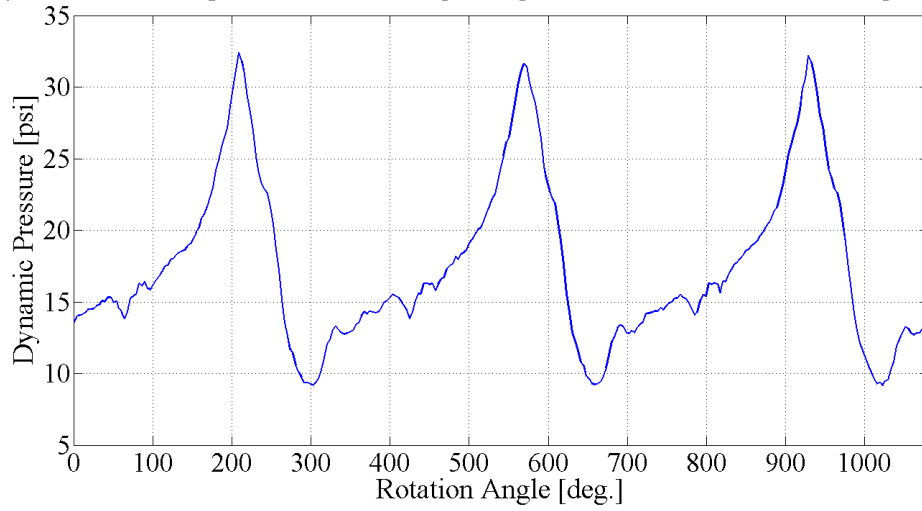


Figure 106: 12.5 mil radial clearance annulus pressure at 3000 RPM

Dynamic Pressure [psi] vs. Rotation Angle [deg.], 3600 RPM, 12.5 mil Bearing Clearance

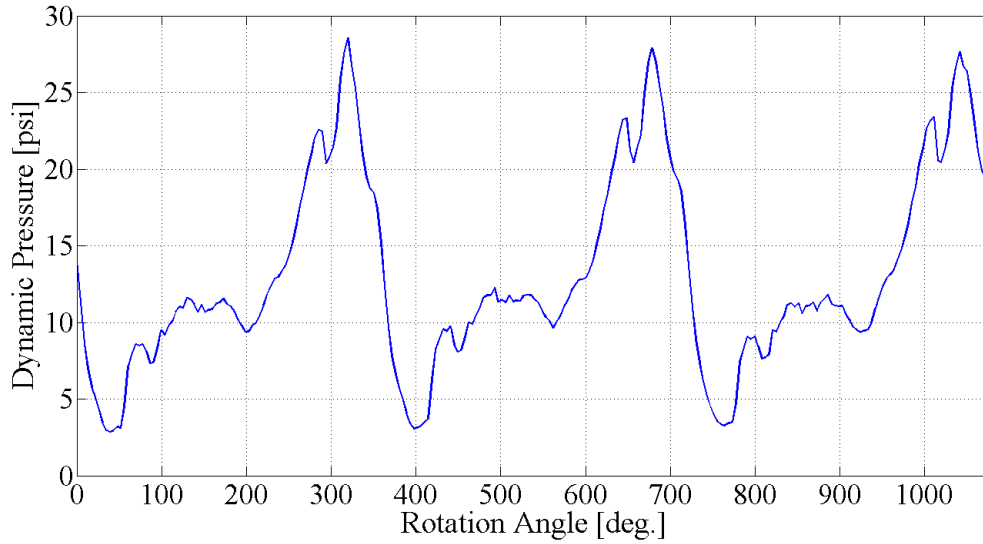


Figure 107: 12.5 mil radial clearance annulus pressure at 3600 RPM

Imbalance Disk Orbit, 12.5 mil Bearing Clearance

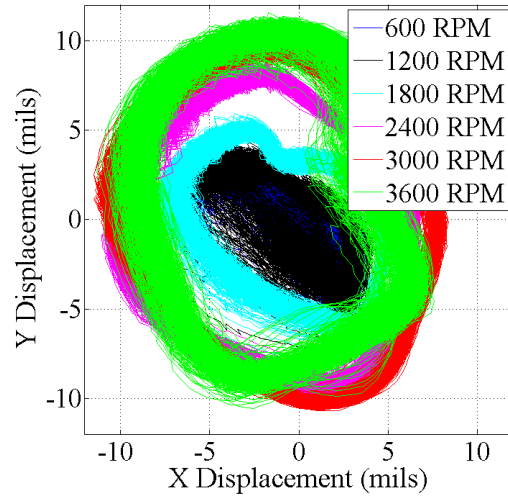


Figure 108: 12.5 mil orbit comparison as a function of speed

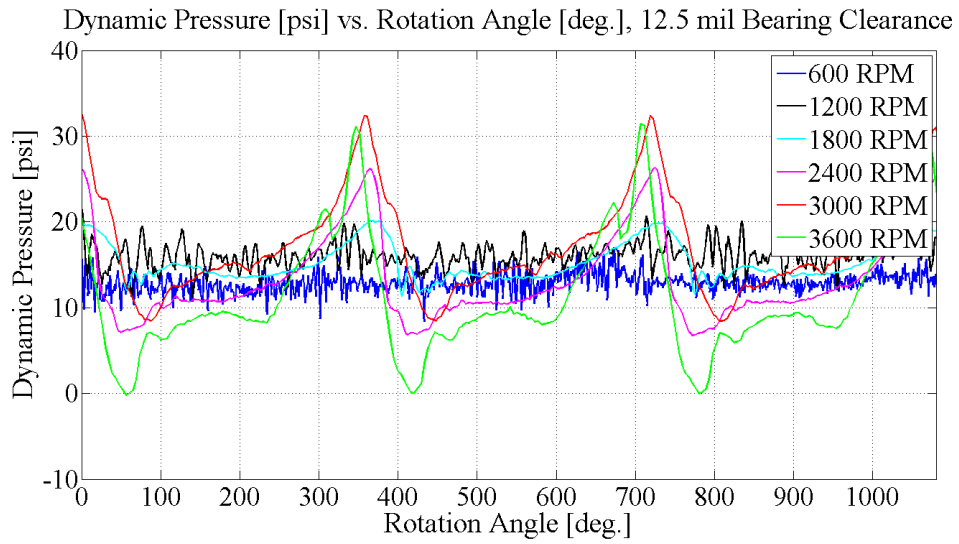


Figure 109: 12.5 mil pressure comparison as a function of angle

600 RPM, 12.5 mil Bearing Clearance Annulus Pressure Compared to Sommerfeld Prediction

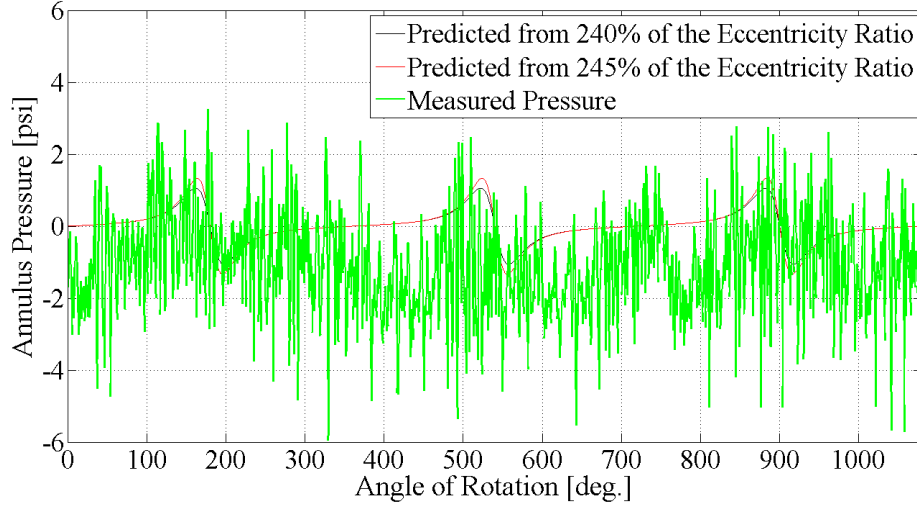


Figure 110: 12.5 mil predicted and measured pressure at 600 RPM

1200 RPM, 12.5 mil Bearing Clearance Annulus Pressure Compared to Sommerfeld Prediction

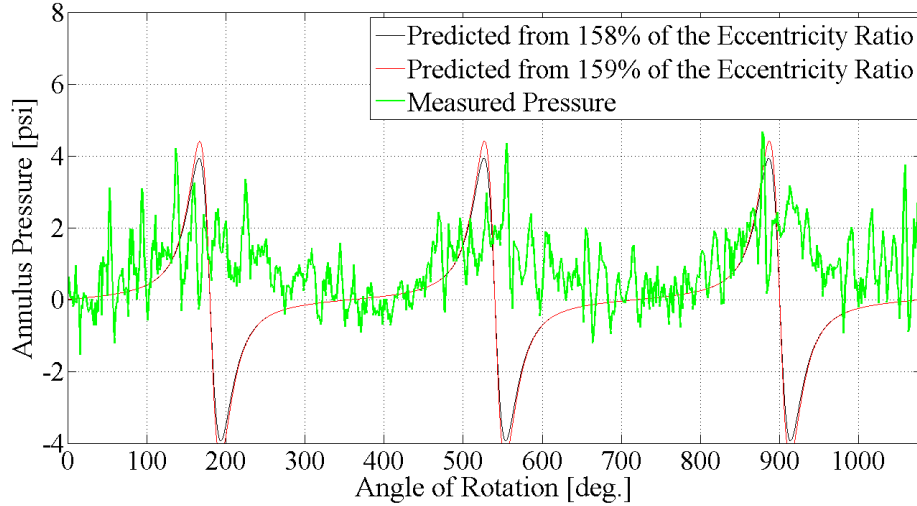


Figure 111: 12.5 mil predicted and measured pressure at 1200 RPM

1800 RPM, 12.5 mil Bearing Clearance Annulus Pressure Compared to Sommerfeld Prediction

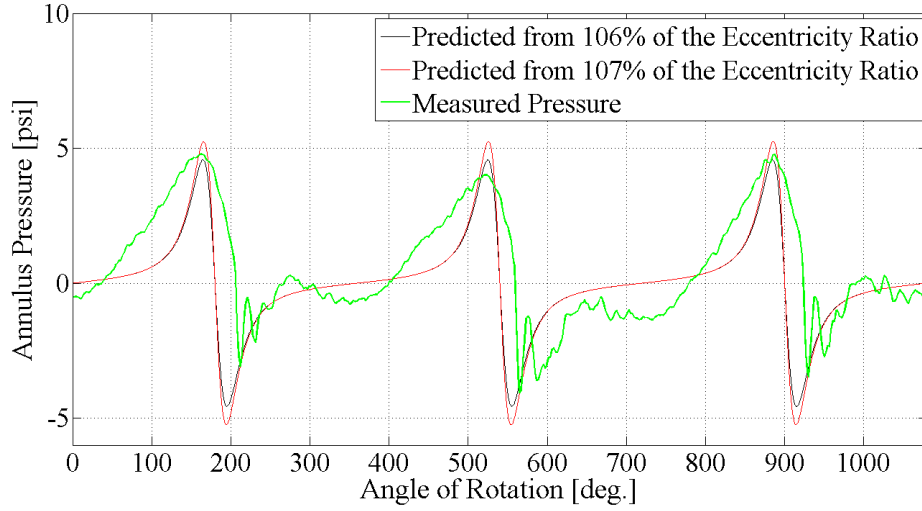


Figure 112: 12.5 mil predicted and measured pressure at 1800 RPM

2400 RPM, 12.5 mil Bearing Clearance Annulus Pressure Compared to Sommerfeld Prediction

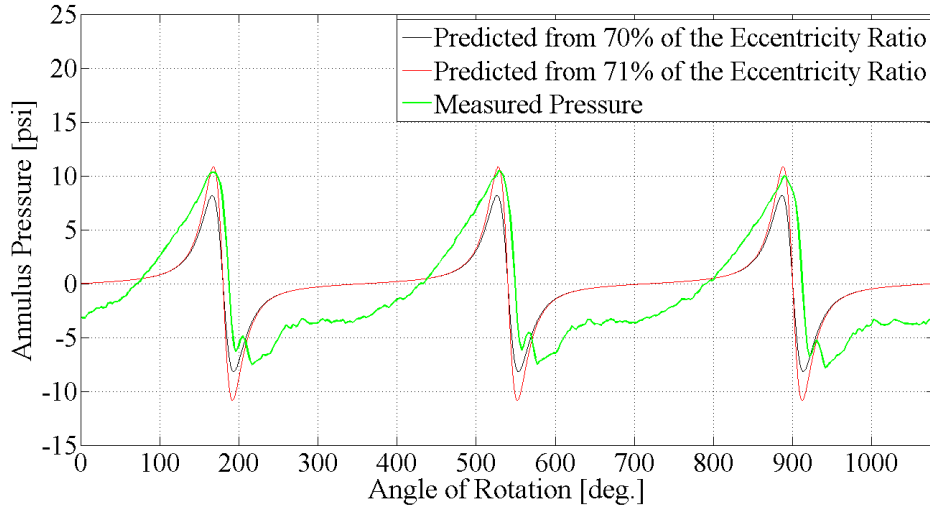


Figure 113: 12.5 mil predicted and measured pressure at 2400 RPM

3000 RPM, 12.5 mil Bearing Clearance Annulus Pressure Compared to Sommerfeld Prediction

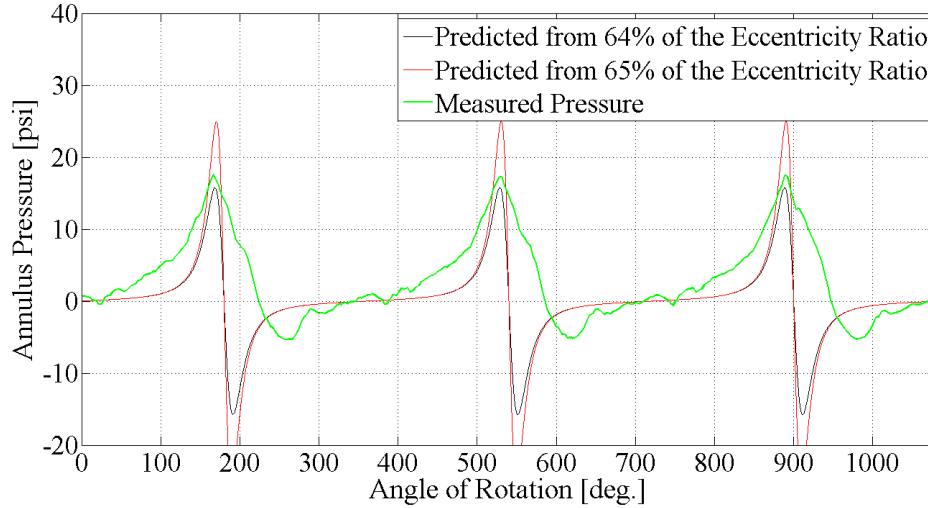


Figure 114: 12.5 mil predicted and measured pressure at 3000 RPM

3600 RPM, 12.5 mil Bearing Clearance Annulus Pressure Compared to Sommerfeld Prediction

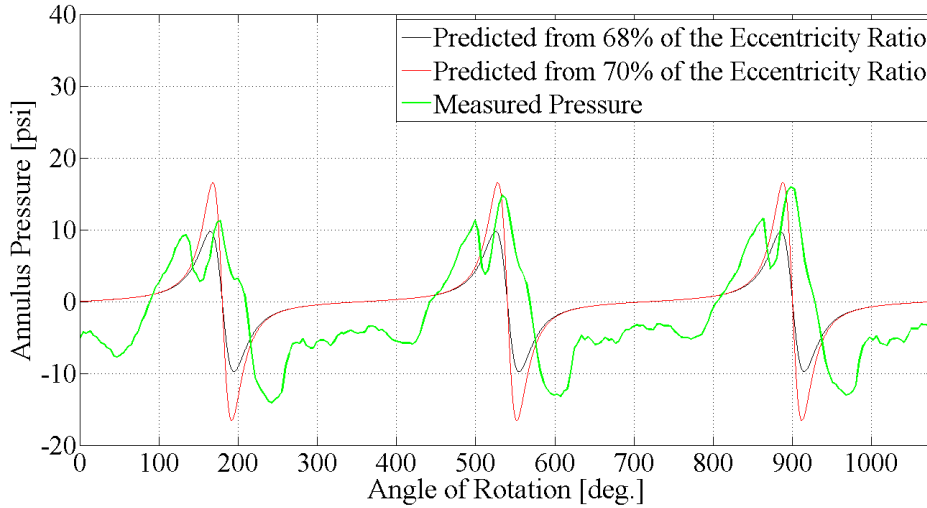


Figure 115: 12.5 mil predicted and measured pressure at 3600 RPM

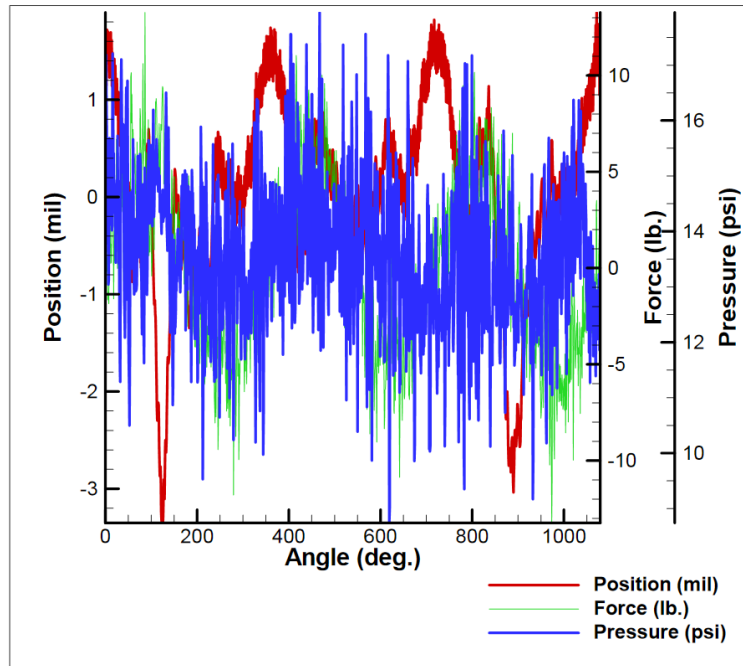


Figure 116: 12.5 mil position, force, and pressure comparison at 600 RPM

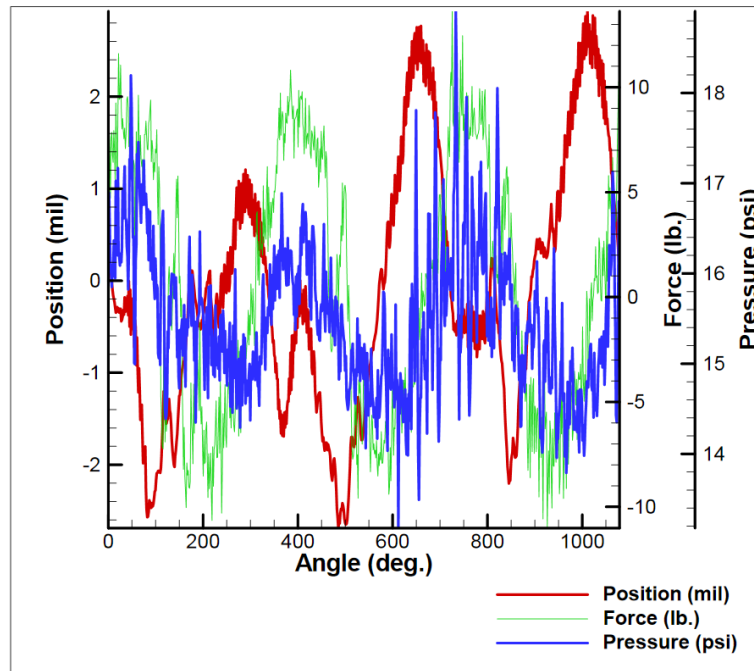


Figure 117: 12.5 mil position, force, and pressure comparison at 1200 RPM

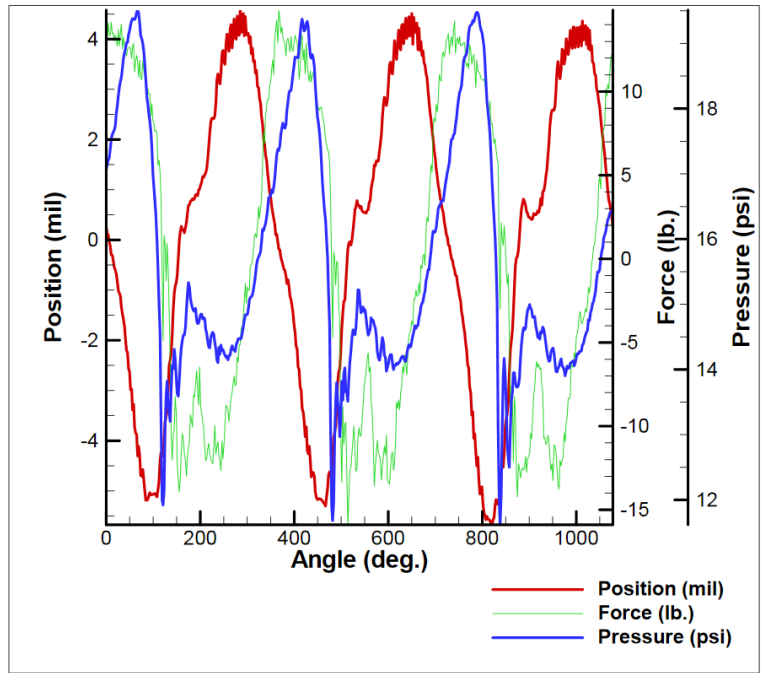


Figure 118: 12.5 mil position, force, and pressure comparison at 1800 RPM

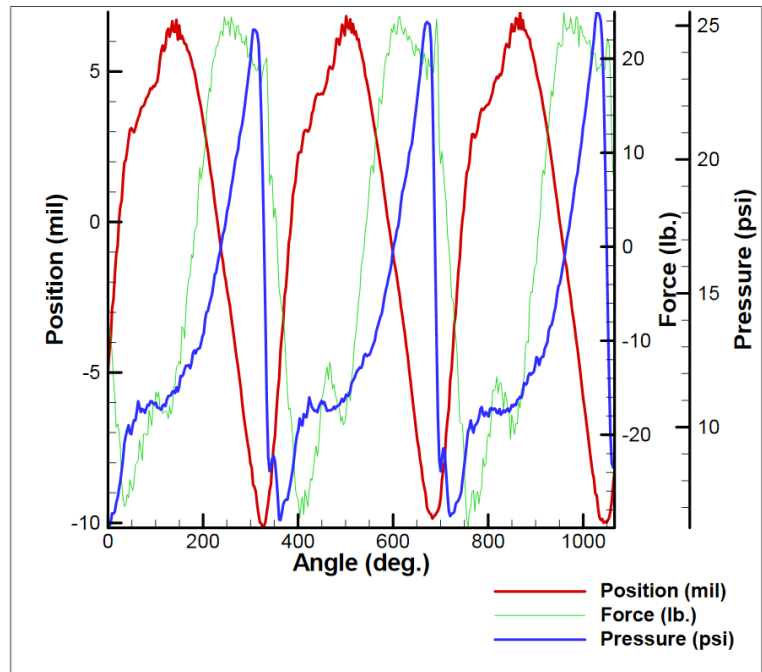


Figure 119: 12.5 mil position, force, and pressure comparison at 2400 RPM

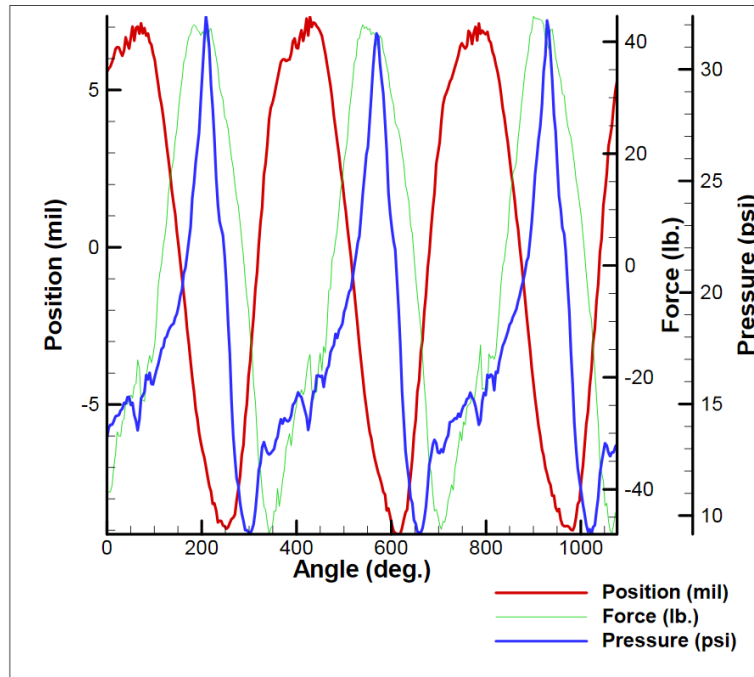


Figure 120: 12.5 mil position, force, and pressure comparison at 3000 RPM

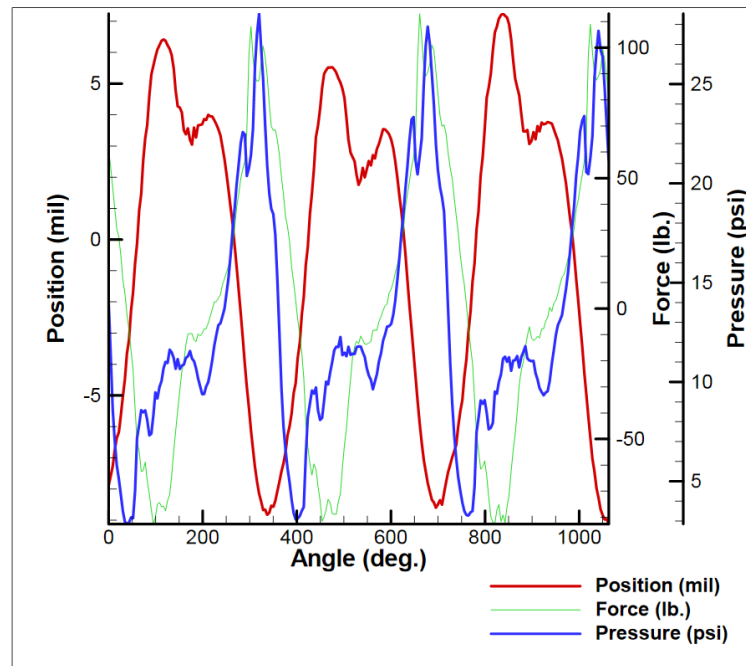


Figure 121: 12.5 mil position, force, and pressure comparison at 3600 RPM